# EXTRACTION OF THE $^1S_0$ NEUTRON-NEUTRON SCATTERING LENGTH FROM A KINEMATICALLY-COMPLETE N-D BREAKUP EXPERIMENT

by

Dinko E. González Trotter

Department of Physics
Duke University

Date: _____
Approved:

_____
W. Tornow, Supervisor

_____
Calvin Howell

_____
Roxanne Springer

_____
Richard Walter

_____
Henry Weller

Dissertation submitted in partial fulfillment of
the requirements for the degree of
Doctor of Philosophy in the Department of Physics
in the Graduate School of Duke University

1998

ABSTRACT

(Physics – Nuclear)

# EXTRACTION OF THE $^1S_0$ NEUTRON-NEUTRON SCATTERING LENGTH FROM A KINEMATICALLY-COMPLETE N-D BREAKUP EXPERIMENT

by

Dinko E. González Trotter

Department of Physics
Duke University

Date: _____
Approved:

_____
W. Tornow, Supervisor

_____
Calvin Howell

_____
Roxanne Springer

_____
Richard Walter

_____
Henry Weller

An abstract submitted in partial fulfillment of
the requirements for the degree of
Doctor of Philosophy in the Department of Physics
in the Graduate School of Duke University

1998

ABSTRACT

by

Dinko E. González Trotter

The world-average for the neutron-neutron scattering length ($a_{nn}$) determined from kinematically-complete $nd$ breakup experiments is $-16.7 \pm 0.5$ fm [Mil90]. This quantity is in disagreement with the average $a_{nn}$ of $-18.6 \pm 0.3$ fm [Mil90] extracted from two $\pi^-$d capture experiments [Gab84, Sch87]. The proton-proton scattering length (corrected for electromagnetic interactions) is $a_{pp}^N = -17.3 \pm 0.4$ fm [Mil90]. The $\pi^-$d $a_{nn}$ value is consistent with theoretical calculations of the effect of charge-symmetry breaking (CSB) on the $^1S_0$ part of the nucleon-nucleon interaction ($\Delta a_{nn}{}_{CSB}^{calc} = |a_{nn}| - |a_{pp}| = 1.5 \pm 0.4$ fm [Mil90]). Due to the paramount importance that charge symmetry has in nucleon-nucleon and sub-nucleon models, the present discrepancy must be resolved.

One reason for this discrepancy could be the methods used in the analysis of the $nd$ breakup experimental data. Another possibility is that the presence of a third strongly-interacting particle in the exit channel of the $nd$ breakup reaction induces a three-nucleon force (3NF) [Šla89]. A 3NF is predicted to manifest itself as a systematic dependence of $a_{nn}$ on the neutron-neutron ($nn$) production angle ($\theta_{nn}$) in the $nd$ breakup exit channel [Hüb93].

A kinematically-complete $nd$ breakup $^2$H(n,nnp) experiment (with bombarding neutron beam energy of $E_0 = 13.0$ MeV) has been performed at the Triangle Universities Nuclear Laboratory (TUNL) with the aim of extracting the $nn$ scattering length $a_{nn}$ from the comparison of experimental absolute $nd$ breakup cross sections with rigorous three-nucleon calculations [Wit96]. The absolute cross sections for neutron-neutron final-state interaction ($nn$ FSI) configurations (where the neutrons in the exit channel leave with zero relative momentum) were measured at production angles $\theta_{nn} = 20.5°$, $28.0°$, $35.5°$ and $43.0°$ with respect to the incident neutron beam axis.

Theoretical calculations of $nn$ FSI cross sections were done using a modified version

of the Bonn-B one-boson exchange potential for several values of $a_{nn}$. These calculations allowed us to construct three-nucleon cross-section libraries which were incorporated in detailed Monte-Carlo simulations of the TUNL $nd$ breakup experiment. The events generated by the Monte-Carlo simulations were treated in the same way as the experimental events, allowing for direct comparison between theoretical and experimental $nn$ FSI cross sections.

Our results show no strong angular dependence of $a_{nn}$, i.e., no evidence for a 3NF was found within the experimental uncertainties. We obtained $a_{nn} = -18.7 \pm 0.6$ fm, in agreement with the $\pi^-$d results for $a_{nn}$.

# Acknowledgements

The TUNL $a_{nn}$ experiment, like most nuclear physics experiments, was the product of a coordinated and continuous group effort. Werner Tornow's insight, dedication and patience at all stages of the experiment and during the data analysis ensured the success of this endeavor. I am thankful to my friend and colleague, Frank Salinas, for his work sorting the great volume of experimental data acquired. We benefited from Calvin Howell's helpful and persistent work, especially during the setting-up and debugging phase of the experiment. I am also indebted to the members of the neutron time-of-flight group for their help: Qiankun Chen, Alex Crowell, Chris Roper and Richard Walter. In addition, the following visiting scientists also contributed: Yingtang Chen [1], Zemin Chen [1], Hongqing Tang [2], Zuying Zhou [2] and Scott Carman [3]. Henryk Witała [4] from the Bochum-Cracow group provided the program to rigorously calculate the *nd* breakup cross sections, which allowed us to create libraries for the Monte-Carlo simulation of our experiment. I also wish to thank the following people at the Physikalisch-Technische Bundesanstalt, Braunschweig, Germany, for their help in the characterization and efficiency measurement of our neutron detectors: Horst Klein, Dankwart Schmidt, Wolf Mannhart and Sigmund Guldbakke.

The help and influence of my family have had a great impact on my life and work. I am deeply grateful to my parents, María Eugenia Trotter Gannat and Bión González León,

[1] Tsinghua University, Beijing, China
[2] CIAE, Beijing, China
[3] Lawrence Livermore National Laboratory
[4] Jagellonian University, Cracow, Poland

for stimulating my intellectual curiosity from an early age and always providing me with their unconditional support. My thanks also go to my grandfather, Ursus Trotter Schifko, for his example of hard work and perseverance. Finally, I especially thank my fiancée (and soon to be wife) Susanne Hauger for her love, patience and help in all things (including proofreading this thesis).

Dinko E. González Trotter

*Duke University*

*September 1998*

To My Family

# Contents

**Abstract** iv

**Acknowledgements** vi

**List of Figures** xiii

**List of Tables** xvi

**Chapter 1 Introduction** 1

1.0.1 Charge-Symmetry Breaking and the Nuclear Force . . . . . 1

1.0.2 Three-Particle Kinematics . . . . . 2

1.0.3 Scattering Length . . . . . 3

**Chapter 2 Experimental Setup** 9

2.1 Introduction . . . . . 9

2.2 Neutron Production and Collimation . . . . . 10

2.3 Detector Types . . . . . 12

2.3.1 Center Detector . . . . . 12

2.3.2 Neutron Detectors . . . . . 12

2.3.3 Layout of Detectors . . . . . 15

2.4 Detector Electronics . . . . . 16

2.4.1 Neutron Detectors . . . . . 16

2.4.2 Center Detector . . . . . 18
2.4.3 Computer Trigger . . . . . 21
2.4.4 CAMAC Electronics . . . . . 23

**Chapter 3 Theory** **28**

3.1 Introduction . . . . . 28
3.2 Meson-Exchange Theory and the Bonn-B Potential . . . . . 29
3.3 3N Breakup Formalism . . . . . 31
3.3.1 NN Forces . . . . . 31
3.3.2 Three-Body Forces . . . . . 35
3.3.3 Breakup Cross Sections . . . . . 37

**Chapter 4 Monte-Carlo Simulations** **40**

4.1 Introduction . . . . . 40
4.2 Cross-Section Libraries . . . . . 41
4.3 Monte-Carlo Codes . . . . . 44
4.3.1 *nd* Elastic Scattering . . . . . 44
4.3.2 *nd* Breakup . . . . . 45

**Chapter 5 Data Analysis** **53**

5.1 Luminosity Determination . . . . . 54
5.1.1 Accidental *nd* Elastic Scattering Events . . . . . 55
5.1.2 Sample-Correlated Background . . . . . 56
5.2 Dead-Time and ADC-Loss Corrections . . . . . 60
5.3 Center Detector Light-Output Functions . . . . . 61
5.4 Breakup Event Sorting . . . . . 63
5.5 Breakup Cross-Section Determination . . . . . 64
5.5.1 Event Projection onto the Ideal-Locus S-Curve . . . . . 64
5.5.2 Cross-Talk Background Subtraction . . . . . 65

5.5.3 Breakup Cross-Section Uncertainties . . . . . 66
5.6 Extraction of $a_{nn}$ . . . . . 68
5.6.1 Extraction from the Absolute $nn$ FSI Cross Section . . . . . 68
5.6.2 Extraction from the Shape of the $nn$ FSI Cross Section . . . . . 68

**Chapter 6 Neutron Detector Efficiencies** **73**
6.1 Introduction . . . . . 73
6.2 Measurements at PTB . . . . . 74
6.2.1 Experimental Setup . . . . . 74
6.2.2 Proton Light-Output Function Determination . . . . . 75
6.2.3 Phototube Nonlinearity Problem . . . . . 79
6.2.4 Comparison of Experimental and Simulated Pulse Heights and Fluences 83
6.3 Measurements at TUNL . . . . . 90
6.3.1 Introduction . . . . . 90
6.3.2 Experimental Setup . . . . . 90
6.3.3 Data Analysis . . . . . 92
6.4 Results . . . . . 93

**Chapter 7 Results and Conclusions** **98**
7.1 Resulting $a_{nn}$ from the TUNL Experiment . . . . . 99
7.1.1 Extraction of $a_{nn}$ from the Absolute Cross Sections . . . . . 99
7.1.2 Extraction of $a_{nn}$ from Cross-Section Shapes . . . . . 100
7.2 Conclusions . . . . . 101
7.2.1 Charge-Symmetry Breaking in the Nuclear Force . . . . . 101
7.2.2 Discrepancies With Erlangen's $a_{nn}$ Results . . . . . 104
7.2.3 Absence of a Strong Three-Body Force . . . . . 105

**Appendix A $nd$ breakup Cross-Section Tables** **108**

**Appendix B Kinematic Plots** **110**

**Bibliography** **115**

**Biography** **120**

# List of Figures

1.1 Kinematic S-curve for *nd* breakup, where $\phi_{12} = 0°$ . . . . . 4
1.2 In the *nn* FSI both outgoing neutrons have the same momentum . . . . . 6
1.3 Monte-Carlo calculation of the absolute *nn* FSI cross sections . . . . . 7

2.1 Lateral cross-section view of the gas cell . . . . . 11
2.2 Front view of ring (bottom of figure) and transmission detectors . . . . . 14
2.3 Sketch of complete ring and transmission detectors. . . . . 15
2.4 Layout of detectors in the TUNL Shielded Neutron Source . . . . . 17
2.5 Simplified electronics diagram for neutron detector . . . . . 19
2.6 Electronics diagram for the center detector. . . . . 21
2.7 Simplified computer trigger electronics diagram. . . . . 23
2.8 Fast-clear circuit for TDCs and crate inhibit . . . . . 24
2.9 Computer trigger electronics diagram . . . . . 25
2.10 LED pulser electronic diagram. . . . . 27

3.1 Infinite multiple-scattering series for *nd* breakup . . . . . 32
3.2 Jacobi momenta and coupling scheme for particles . . . . . 35
3.3 3NF diagram due to 2-$\pi$ exchange . . . . . 36
3.4 The Tucson-Melbourne 3NF (cutoff parameter $\Lambda = 5.8\mu$) . . . . . 38

4.1 Point-geometry S-curves for several *nn* FSI . . . . . 41

4.2 Time-of-Flight spectrum associated with detector 9 . . . . . 46
4.3 MC Center Detector pulse-height spectrum . . . . . 47
4.4 $\bar{\Sigma}(E_1', E_2', E_3')$ matrix . . . . . 50
4.5 Comparison of finite and point-geometry $nd$ breakup differential cross sections 52

5.1 Doubles TOF spectrum for detector 8 . . . . . 56
5.2 Elastic scattering events CDPH spectrum for detector 8 . . . . . 58
5.3 Elastic scattering events CDPH spectrum for detector 17. . . . . 59
5.4 Low-gain $L_d(E)$ for the Feb95 run (top) . . . . . 62
5.5 Typical triples TOF spectra . . . . . 70
5.6 Experimental diagonal projection for $nn$ FSI . . . . . 71
5.7 $\chi^2$ determination of $a_{nn}$ . . . . . 71
5.8 $\chi^2$ versus $a_{nn}$ from the cross-section shape . . . . . 72

6.1 Compton-edge position . . . . . 79
6.2 $\xi(E)$ for detectors T1 and R1. . . . . 84
6.3 Comparison of experimental and calculated PH responses . . . . . 85
6.4 $r_i^{\frac{E}{C}}$ factors for detector T1 . . . . . 86
6.5 Comparison of calculated and experimental PH responses for detector R1 . 86
6.6 $r_i^{\frac{E}{C}}$ factors for detector R1 . . . . . 87
6.7 Comparison of calculated and experimental PH responses for detector B2 . 87
6.8 $r_i^{\frac{E}{C}}$ factors for detector B2 . . . . . 88
6.9 Top view of the general layout of neutron detectors . . . . . 91
6.10 Comparison of TUNL-obtained efficiencies to NEFFR1 . . . . . 93
6.11 Comparison of TUNL-obtained efficiencies to NEFF7 . . . . . 94
6.12 Comparison of efficiency for transmission-type detectors . . . . . 95
6.13 Deviation (ratio of experimental and calculated efficiency E/C) of TUNL experimental efficiencies . . . . . 97

7.1 Cross section for $\theta_{nn} = 20.5^\circ$ . . . . . 101
7.2 Cross section for $\theta_{nn} = 28.0^\circ$ . . . . . 102
7.3 Cross section for $\theta_{nn} = 35.5^\circ$ . . . . . 103
7.4 Cross section for $\theta_{nn} = 43.0^\circ$ . . . . . 104
7.5 Cross-section comparison for $\theta_{nn} = 25.0^\circ$ . . . . . 106

B.1 Kinematic curves for $E_2$ and $E_3$ as a function of $E_1$ ($\theta_{nn} = 43.0^\circ$). . . . . 111
B.2 Kinematic curves for $E_2$ and $E_3$ as a function of $E_1$ ($\theta_{nn} = 35.5^\circ$). . . . . 112
B.3 Kinematic curves for $E_2$ and $E_3$ as a function of $E_1$ ($\theta_{nn} = 28.0^\circ$). . . . . 113
B.4 Kinematic curves for $E_2$ and $E_3$ as a function of $E_1$ ($\theta_{nn} = 20.5^\circ$). . . . . 114

# List of Tables


2.1 Some basic properties of NE-213 and BC-501 liquid scintillators. . . . . 16

2.2 Electronic pair assignment. . . . . 20

2.3 TDC configuration for stop TOF and PSD signals . . . . . 26

4.1 Values for $\sigma$-meson coupling constants . . . . . 43

4.2 Angular span of $nn$ FSI libraries . . . . . 43

5.1 Summary of runs of the $a_{nn}$ experiment . . . . . 54

5.2 Luminosity $\beta_r$ extracted for each run . . . . . 60

5.3 Tag assignment to types of triple events . . . . . 64

6.1 Compton-edge position . . . . . 77

6.2 Fit factors $c_x$ and fluence-comparison ratios obtained for detector R1 . . . . 81

6.3 Fit factors $c_x$ obtained for detector T1. . . . . 82

6.4 Fit factors $c_x$ and fluence-comparison ratios obtained for detector B2 . . . . 89

7.1 $a_{nn}$ values extracted from the absolute $nn$ FSI cross sections . . . . . 99

7.2 $a_{nn}$ extracted from the shapes of three $nn$ FSI cross-sections . . . . . 100

A.1 $nd$ breakup cross sections . . . . . 109

# Chapter 1

# Introduction

### 1.0.1 Charge-Symmetry Breaking and the Nuclear Force

The neutron was the second hadronic constituent of atomic nuclei to be discovered. The existence of this electrically neutral particle with a mass close to that of the proton was recognized by J. Chadwick in 1932. It was thought for some time that nuclear cohesiveness was due to neutron-proton $np$ forces, but binding energy calculations of hydrogen and helium isotopes compared with experimental values showed the existence of a neutron-neutron $nn$ force [Pre36]. Soon after, scattering experiments pointed to the existence of a proton-proton $pp$ nuclear force [Tuv36]. In 1932 W. Heisenberg proposed that $pp$ and $nn$ interactions were the same [Hei32]. This principle, called charge symmetry (CS), implies that hadronic interactions are invariant under a 180° rotation in isospin space. Mirror nuclei (such as $^3$H and $^3$He) however, show larger binding energies for the more neutron-rich species. This is known as the Nolen-Schiffer anomaly, and suggests that $nn$ interactions are slightly stronger than $pp$ ones.

The modern theory of Quantum Chromodynamics (QCD) casts quarks as the elementary constituents of nucleons, with a neutron consisting of two Down and one Up quark and the proton of one Down and two Up quarks. The quark field can be put in the form of an isospin doublet which can further be expanded into left (L) and right (R) chirality pro-

jections. This allows the QCD Lagrangian $\mathcal{L}$ to be expressed as a sum of a scale-invariant term $\mathcal{L}_\lambda$ and a mass term $\mathcal{L}_M$. Because the Up and Down quark masses are not the same ($m_u \approx 6$ MeV, $m_d \approx 10$ MeV), $\mathcal{L}_M$ is not invariant under identical rotations of the L and R quark fields. Such rotations imply a change of a quark from its Up to its Down state (i.e., a neutron changing into a proton) or vice-versa. Thus, lack of invariance of $\mathcal{L}$ under identical rotations of L and R quark fields indicates that neutron and proton strong interactions are not identical and CS is broken.

### 1.0.2 Three-Particle Kinematics

The *nd* breakup reaction consists on a stationary deuteron target which interacts with a neutron projectile producing two neutrons and a proton in the exit channel. From conservation of momentum and energy we can write an expression relating the energies of the outgoing neutrons $E_1$ and $E_2$ in the laboratory frame

$$\begin{aligned}\frac{1}{m_3}[E_1(m_1+m_3)+E_2(m_2+m_3) \\ - 2\sqrt{m_0 m_1 E_0 E_1}\cos\theta_1 - 2\sqrt{m_0 m_2 E_0 E_2}\cos\theta_2 \\ + 2\sqrt{m_1 m_2 E_1 E_2}\cos\theta_{12}] = Q + E_0(1-\frac{m_0}{m_3}).\end{aligned} \tag{1.1}$$

The projectile energy and mass have the subscript 0. The subscripts 1 and 2 refer to the neutrons and 3 to the proton. Given the momenta in the laboratory frame $\vec{k}_1$, $\vec{k}_2$ and $\vec{q}_0$ we have

$$\cos\theta_i = \hat{k}_i \cdot \hat{q}_0 \tag{1.2}$$

and

$$\cos\theta_{12} = \hat{k}_1 \cdot \hat{k}_2. \tag{1.3}$$

The Q-value of the reaction is given by

$$Q = ((m_d + m_0) - (m_1 + m_2 + m_3))c^2, \tag{1.4}$$

where $m_d$ is the mass of the deuteron and $m_0$ is the mass of the projectile particle (a neutron in this case). Once $\theta_{12}$ and $\theta_i$ are chosen, Equation 1.1 describes the so-called kinematic S-curve relating $E_2$ to $E_1$. The $nd$ breakup cross section is determined along the length of the S-curve, which is defined to begin at $E_2 = 0$ MeV (see Figure 1.1).

Kinematically-complete $nd$ breakup experiments measure the energy of the neutrons in the exit channel. The $\theta_i$ angles are also known and the momenta $\vec{k}_1$ and $\vec{k}_2$ can be obtained by time-of-flight analysis. In the TUNL experiment we have also measured the proton energy $E_3$ for a kinematically-overdetermined analysis. Kinematically-incomplete experiments measure only the proton energy at 0° with respect to the incoming neutron beam. In this case, neutrons in the $nn$ FSI configurations have only $\sim$ 50 keV of kinetic energy, and cannot be reliably detected. In general, the undetected neutrons associated with a given proton energy can have a large range of momenta, so kinematically-incomplete $nd$ breakup experiments span a much larger region of phase space than the kinematically-complete ones.

### 1.0.3 Scattering Length

The $^1S_0$ scattering length $a_0$ is a parameter directly related to the interaction strength and the scattering cross section $\sigma$ between two particles. It is defined as

$$\lim_{k \to 0} \sigma = 4\pi a_0^2, \tag{1.5}$$

where $k$ is the relative momentum of the particles. One can also write

$$a_0 = \pm \lim_{k \to 0} \frac{\delta_0}{k}, \tag{1.6}$$

where $\delta_0$ is the $l = 0$ phase shift induced on the scattered wave function by a potential. The positive and negative signs indicate bound and unbound two-particle states, respectively.

For nearly-bound nucleon-nucleon (NN) systems the scattering length is very sensitive to small variations of the nuclear potential. A $\sim$1% change in the nuclear interaction

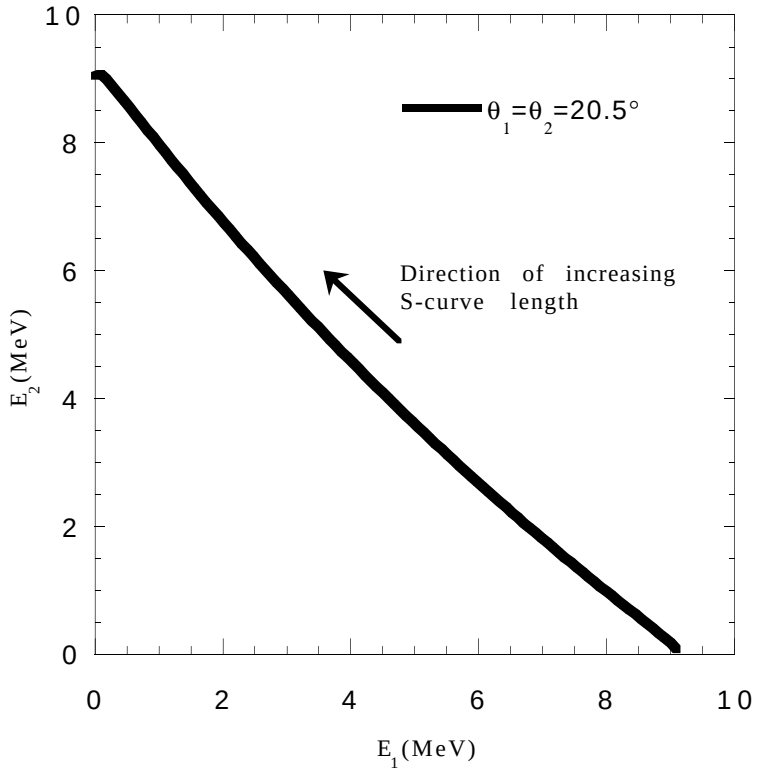


Figure 1.1: Kinematic S-curve for $nd$ breakup, where $\phi_{12} = 0^\circ$ and $\theta_i = 20.5^\circ$. The neutron projectile has $E_0 = 13.0$ MeV.

potential leads to a $\sim 3$ fm change in the NN scattering length $a_{NN}$, making it an ideal parameter to determine charge-symmetry breaking (CSB) [Tér89].

The magnitude of the proton-proton $^1S_0$ scattering length $a_{pp}^N$ has been determined to be $-17.3 \pm 0.4$ fm [Mil90]. Most of the uncertainty is rooted in difficulties in accounting for the Coulomb part of the $pp$ interaction. Because of the lack of a neutron target, determination of the neutron-neutron $^1S_0$ scattering length $a_{nn}$ has been attempted by indirect means via kinematically-incomplete and kinematically-complete $nd$ breakup and $\pi^-$d capture experiments [Gab84, Sch87]. The average $a_{nn}$ values extracted from these two families of experiments are $-16.7 \pm 0.5$ fm (kinematically-complete $nd$ breakup) and $-18.6 \pm 0.3$ fm (average of a kinematically-incomplete and a kinematically-overdetermined $\pi^-$d capture experiment) [Mil90]. Removing this discrepancy and finding an accurate value for $a_{nn}$ would help to determine the magnitude of CSB at the nucleon level.

Kinematically-incomplete $nd$ breakup experiments give $a_{nn} = -19.1 \pm 2$ fm [Šla89], where the large error bar is due to the sensitivity of the extracted $a_{nn}$ to the theoretical models used in the data analyses, experimental resolution and energy uncertainties. A modern and rigorous analysis of the same data gives much less negative values [Tor96, Tor93a].

Unless otherwise stated, future mention of $nd$ breakup in this work will refer implicitly to the kinematically-complete case. One reason for the disagreement between the $\pi^-$d and $nd$ breakup results is that various methods that are presently outdated were used to extract $a_{nn}$ from the $nd$ breakup reaction. Like the present experiment, the earlier $nd$ breakup experiments focused on $nn$ final state interaction (FSI) configurations, consisting of cases where the two detected neutrons in the exit channel have zero relative momentum (see Figure 1.2). For these configurations the cross section peaks dramatically due to the existence of a nearly-bound virtual $^1S_0$ state in the $nn$ interaction. In the past, the shapes of various $nn$ FSI yields and cross-section ratios were fitted using a charge-dependent exponential form factor model [Zei74, vW79] or the Watson-Migdal (WM) formalism [One78].

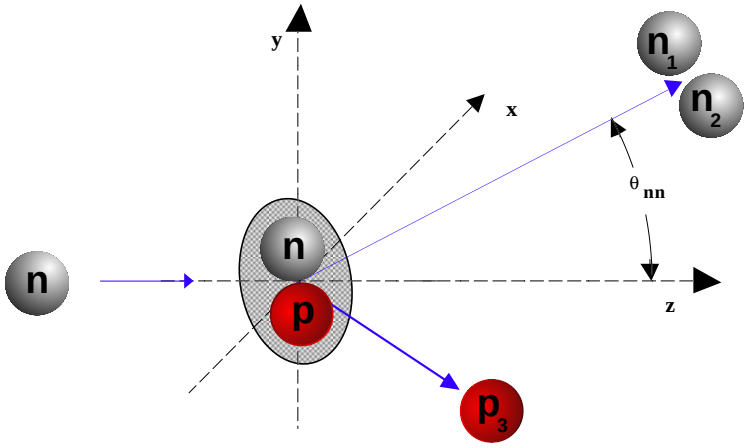


Figure 1.2: In the *nn* FSI both outgoing neutrons have the same momentum. $\theta_{nn}$ denotes the *nn* production angle in the laboratory frame.

More recently, supercomputers allowed the performance of rigorous three-nucleon (3N) calculations of observables in the continuum using realistic NN meson-exchange potentials in a reasonable amount of time [Wit88]. Rigorous 3N calculations indicate that the $a_{nn}$ sensitivity is most evident in the absolute magnitude of the *nn* FSI differential cross-section peak and not in its shape [Wit, Tor93b] (see Figure 1.3).

Gebhardt *et al.* at the Erlangen-Nürnberg University measured the absolute differential *nd* breakup cross section for a *nn* FSI at $\theta_{nn} = 25^{\circ}$ with an incident neutron energy $E_n^{lab} = 13$ MeV. The experimental data were analyzed via the W-matrix approximation [Fra88] to the NN interaction using the Paris potential with $j_{max} \leq 2$ (total two-body angular momentum) as the two-body input. They found $a_{nn} = -17.0 \pm 1.0$ fm [Geb93]. It has recently been shown that the W-matrix approximation results disagree with rigorous 3N cross-section calculations for the *nn* FSI at $\theta_{nn} = 25^{\circ}$, invalidating the $a_{nn}$ extracted from the Erlangen-Nürnberg experiment. A reanalysis of the Erlangen data using rigorous

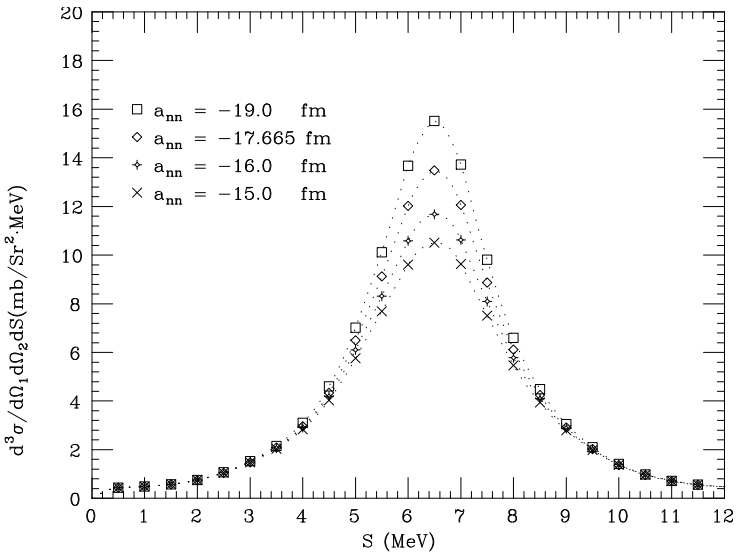


Figure 1.3: Monte-Carlo calculation of the absolute $nn$ FSI cross section for $E_0 = 13.0$ MeV and $\theta_{nn} = 20°$ using the Bonn-B OBEPQ NN potential with modified $^1S_0$ part to yield $a_{nn}$ values between -15.0 and -19.0 fm.

3N calculations yields $a_{nn} = -14.9 \pm 1$ fm [Wit96, Tor94].

The $\pi^-$d capture reaction has two strongly-interacting particles in the outgoing channel, whereas the $nd$ breakup has three, introducing the possibility of three-body forces (3NF), which appear when subnucleonic degrees of freedom (e.g. quark fields) are suppressed in 3N calculations. Studies of 3NF effects using the Tucson-Melbourne 3NF indicate a marked $nn$ production-angle dependence for the $nn$ FSI cross section [Wit96]. The $\theta_{nn} = 43.0°$ $nn$ FSI configuration is of special interest because in its vicinity the Tucson-Melbourne 3NF effect vanishes. In addition, rigorous 3N calculations show the $nn$ FSI cross section at $\theta_{nn} = 43°$ to be relatively insensitive to the details of various realistic potential models [Wit96], making it an ideal configuration from which to extract $a_{nn}$.

This thesis is based on a kinematically-complete $nd$ breakup experiment performed at the TUNL shielded neutron source target area. An $E_n^{lab} = 13$ MeV neutron beam was pro-

duced by the $^2$H(d,n)$^3$He reaction. The beam was collimated and directed to a deuterated scintillator $C_6D_{12}$ target (NE-232) where the *nd* breakup reaction occurs. Eight neutron detector pairs were used to detect the *nn* FSI neutrons at $\theta_{nn} = \pm 20.5^\circ, \pm 28.0^\circ, \pm 35.5^\circ$ and $\pm 43.0^\circ$ in coincidence with the recoiling proton detected in the deuterated scintillator target (also referred to as the center detector). The analysis presented in this thesis comprises a subset of four pairs of detectors covering the four production angles of interest. The neutron energies were determined by the time-of-flight (TOF) method. The data were stored on tape in event-by-event mode for later off-line analysis. The statistical precision for the cross-section peak for all *nn* FSI configurations was at least $\pm 5\%$.

Monte-Carlo simulations were used to evaluate the attenuation of the neutron flux in the center detector, to take into account detector resolution effects and neutron beam energy spread, and to calculate theoretical cross sections for *nn* FSI configurations considering finite-geometry effects. Extensive 3N calculations were done on the Cray Y-MP and T916 computers at the North Carolina Supercomputing Center to create *nn* FSI cross-section libraries needed to account for finite geometry and finite energy resolution of the neutron beam ($\pm 0.2$ MeV). Up to $10^5$ cross sections were calculated for each of the four detector arrangements in order to correctly average the theoretical cross sections over the finite-geometry of the experimental setup. The cross-section libraries were incorporated in Monte-Carlo simulations of the experiment. In this way it was possible to treat experimental and Monte-Carlo data identically and to compare experimental and theoretical cross sections directly. Neutron detector efficiencies obtained independently at TUNL and at PTB [1] were used in both experimental and Monte-Carlo data analyses to determine absolute cross sections for the *nn* FSI configurations of interest.

[1] Physikalisch-Technische Bundesanstalt, Braunschweig, Germany

# Chapter 2

# Experimental Setup

## 2.1 Introduction

Differential cross sections were measured for eight *nn* FSI configurations in a kinematically complete *nd* breakup experiment at the Triangle Universities Nuclear Laboratory (TUNL) Shielded Neutron Source Area. The laboratory's DENIS II ion source, accelerator and beam transport system descriptions can be found in several TUNL Ph.D. theses [Hon86, How84, Gus82] and will not be explained in detail in this work.

A deuteron beam was generated by the ion source and accelerated to 10.4 MeV by the TUNL FN tandem Van de Graaff accelerator. A beam of $E_n^0 = 13.0$ MeV monoenergetic (at 0°) neutrons is produced by the $^2$H(d,n)$^3$He reaction in a gas cell filled with deuterium at 7.8 atm of pressure. The neutron beam is collimated by tapered copper and polyethylene bars and directed to the TUNL Shielded Neutron Source Area, where it interacts with a deuterated scintillator target (center detector). Recoil deuterons from *nd* elastic scattering and protons from the *nd* breakup reaction are produced and detected at the target. Neutron detectors are placed behind one another in pairs at 1.5 m and 2.5 m from the center detector. These neutron detectors register *nn* FSI events by means of triple coincidences with the center detector. At the same time *nd* elastic scattering events are detected as

double coincidences between the center detector and the neutron detectors. Light-emitting diodes (LEDs) are attached to some detectors to measure the dead time of the electronics chain for triple and double events. Detector anode signals are used for TOF measurements, constant-fraction discrimination (CFD) and pulse-shape discrimination (PSD). Integrated and amplified dynode signals from each detector are used for pulse-height analysis.

The experiment took about 2500 net hours of beam time. Absolute neutron detection efficiencies for all detectors were determined at the Physikalisch-Technische Bundesanstalt (PTB) and TUNL. Efficiency measurement techniques and results are treated in Chapter 6.

## 2.2 Neutron Production and Collimation

Monoenergetic $E_n^0 = 13.0$ MeV neutrons are produced via the $^2$H(d,n)$^3$He reaction in a deuterium gas cell (shown in Figure 2.1) at 7.8 atm of pressure. This cell is the same one as described in [Set95]. The gas cell entrance is made of a 0.25 mil Havar foil, and its end consists of a gold beam stop with a thickness of 0.051 cm. The beam stop is soldered to the end of the gas cell to ensure good heat conduction. Copper tubes wound around the gas cell carrying 10°C water to cool the system while a stream of compressed air helps to remove heat from the beam stop. The complete assembly is electrically insulated from the beam pipe so that all the deuteron current on the beam stop is integrated and measured before going to ground. Locally, we refer to this charge deposited by the deuteron beam as BCI (beam current integration).

The $^2$H(d,n)$^3$He reaction has a large and very forward-peaked cross section for production of nearly monoenergetic neutrons [Dro78]. The high Q-value (+3.3 MeV) for this reaction sets monoenergetic neutrons apart by $\gtrsim 5$ MeV from the energy spectrum continuum of breakup neutrons generated in the beam stop and in the deuterium gas via the $^2$H(d,n)dp and $^2$H(d,n)ppn reactions.

The target area is separated from the deuterium gas cell by a multi-layered wall

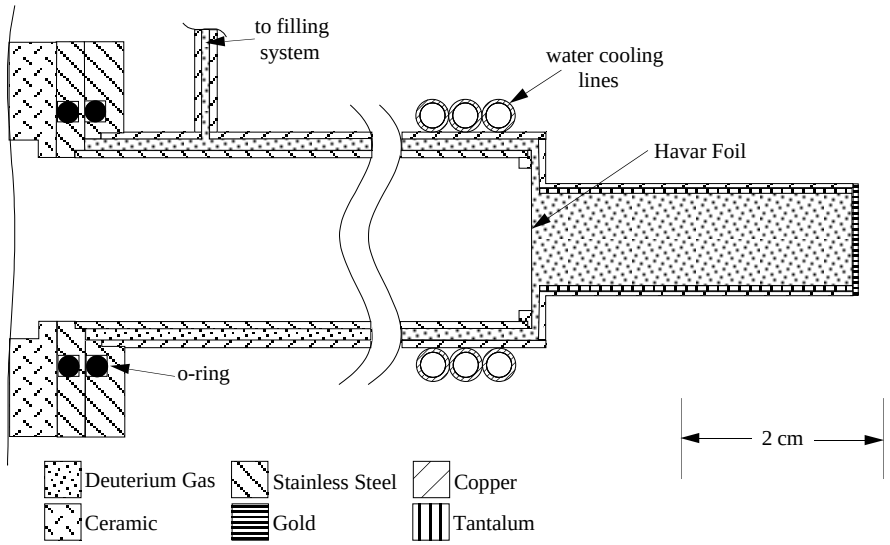


Figure 2.1: Lateral cross-section view of the gas cell used for the $^{2}$H(d,n)$^{3}$He reaction.

composed of concrete, steel, iron, lead and paraffin (see left side of Figure 2.4). This wall shields the target area from most background neutron and gamma radiation produced at the gas cell. An opening with a rectangular cross section allows neutrons produced in the gas cell at $\sim 0^{\circ}$ to reach the center detector located on the opposite side of the shielding wall at a distance of 1.7 m. Copper and polyethylene bars inside the shielding wall opening collimate the neutron beam. Four bars make up the walls of the collimator. Each bar is tapered in order to minimize the number of inscattered neutrons impinging on the target while allowing the target's exposure to a spatially homogeneous field of unscattered neutrons from the gas cell.

## 2.3 Detector Types

### 2.3.1 Center Detector

The center detector consists of a glass cylinder 6 cm high and 4 cm in diameter filled with $C_6D_{12}$ liquid scintillator (NE-232)[1], with a density of 0.96 g/cm$^3$ and a ratio of deuterium to carbon atoms of 1.96. There is a small expansion chamber on the side of the cylinder. Neutrons from the gas cell incident on NE-232 may interact with deuterons through *nd* elastic scattering or *nd* breakup. The resulting charged particles (deuterons or protons) will travel some distance within the center detector's active volume and lose kinetic energy, exciting the NE-232's molecules to states from which they decay in a matter of nanoseconds while emitting light in the ultraviolet end of the spectrum with an intensity proportional to the kinetic energy of the charged particles.

The glass cylinder's exterior is covered with reflector paint except for the bottom surface, where light is allowed to escape. The cylinder rests on top of an RCA 8575 photomultiplier tube's (PMT) window covered with a film of BC-630 optical grease to better couple the indices of refraction of the glass cylinder-PMT interface. The PMT converts the scintillator's light into pulses of electric current of proportional amplitude.

### 2.3.2 Neutron Detectors

Three types of neutron detectors are used in this experiment: ring, transmission and Bicron. These detectors differ in shape, volume and type of liquid scintillator used. The ring and transmission detectors were built at TUNL and filled with NE-213 liquid scintillator in an argon atmosphere to prevent oxygen contamination and loss of pulse-shape discrimination.

The ring detectors consist of a vessel built of two concentric 4 cm-high cylindrical walls. The inner wall is made of 1.5 mm-thick aluminum. The outer wall is made of

[1] Nuclear Enterprises, Edinburgh, Scotland

3.2 mm-thick glass. Front and back 1 mm-thick aluminum plates close the space between the concentric walls to complete the vessel. The inner diameter of the scintillator is 7.6 cm, and the outer diameter is 13.44 cm. A small filling pipe and a Teflon tube used as an expansion chamber are attached to the front and back plates, respectively. The inside of the vessel is coated with BC-624 reflector paint, except for two windows that allow light to be transmitted through lucite light guides into the 2-inch diameter PMTs (see Figure 2.2).

The transmission detectors are similar to the ring detectors, except that the liquid scintillator vessel is built out of only one cylindrical glass wall with front and back aluminum plates glued to it. A single window allows photons from scintillation to escape through a light guide into a PMT (see Figure 2.3).

The Bicron detector vessels are simple aluminum cylinders where one of the ends is a glass window and the opposite end is a 1 mm-thick aluminum plate. The inner radius is 6.34 cm and the interior depth is 5.08 cm. The interior surfaces are coated with BC-622 reflector paint. The vessels are mounted directly on a 5-inch diameter PMT's window with optical grease between the glass surfaces.

The ring and transmission detectors' active volumes consist of NE-213 liquid scintillator. The Bicron detectors use BC-501 fluid (see Table 2.1). These organic liquid scintillators contain hydrogen and carbon in a H:C ratio of 1.2:1 and provide for pulse-shape discrimination (PSD) between detected $\gamma$ rays and neutrons (see Table 2.1).

Two types of detectors (ring and transmission) were constructed because at the time we were not sure the ring detectors would work well due to their complicated geometry, so the transmission detectors would serve as backup. In addition, there were not enough phototubes available to construct more ring detectors. The ring detectors proved to be far more effective in the detection of triple-coincidence events than the transmission detectors. This was due to the larger solid angle subtended by the ring detectors and the fact they do not attenuate the flux of neutrons meant to be detected by the Bicron detectors behind them. The *nn* FSI configurations which included ring detectors accumulated roughly four

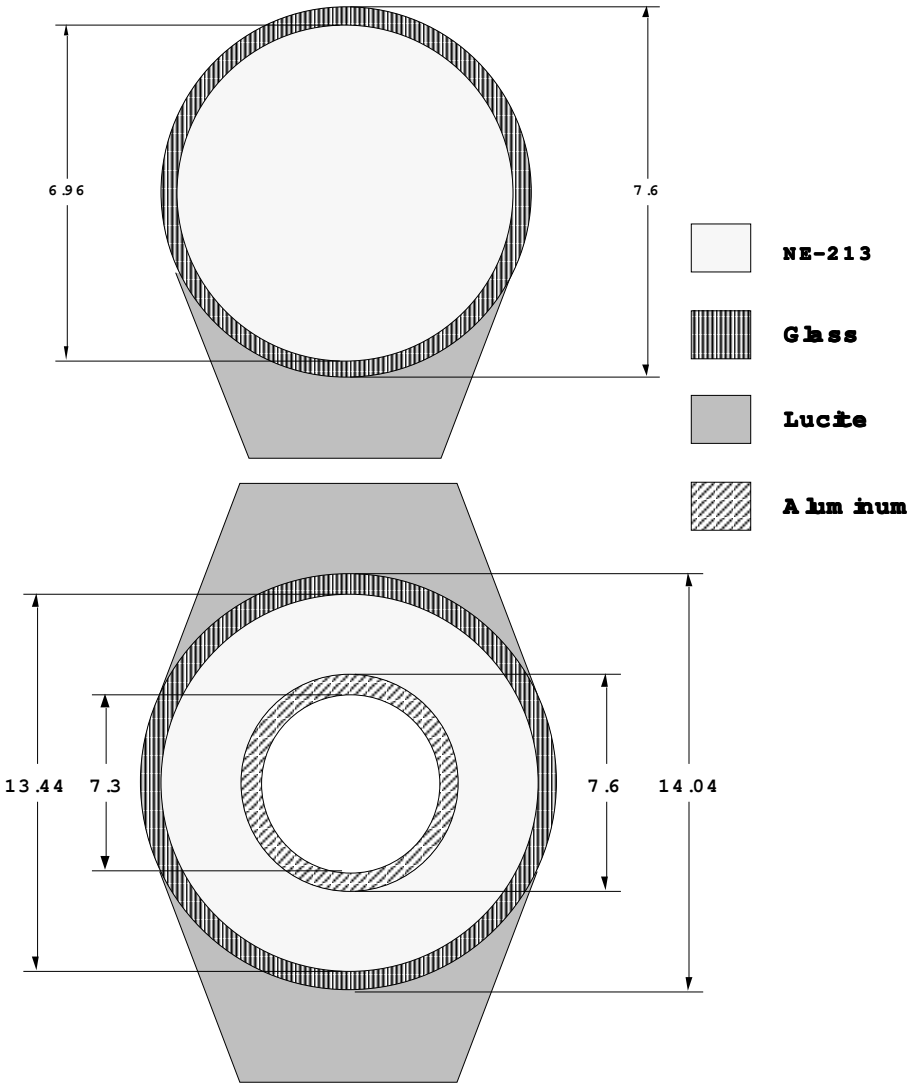


Figure 2.2: Front view of ring (bottom of figure) and transmission detectors (top of figure) with light guides (all dimensions in cm).

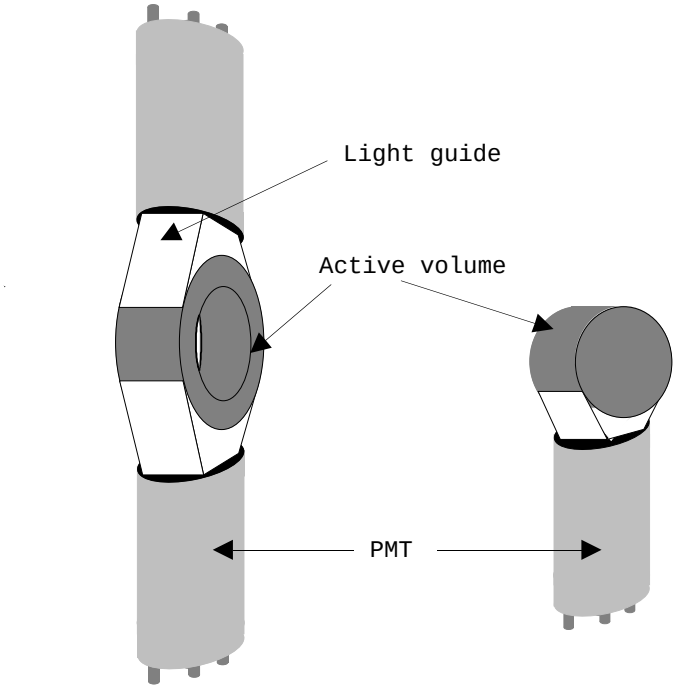


Figure 2.3: Sketch of complete ring and transmission detectors.

times the number of events than their transmission-detector counterparts.

### 2.3.3 Layout of Detectors

Eight *nn* FSI configurations were investigated using sixteen neutron detectors deployed as shown in Figure 2.4. Each detector pair consists of a ring or transmission detector associated with a Bicron detector, registering *nn* FSI events in coincidence with the center detector.

In a transmission-Bicron pair, the transmission detector is placed in front of the Bicron detector, with both active volumes subtending approximately the same solid angle. To register an *nn* FSI event, one neutron must be detected by the transmission detector

Table 2.1: Some basic properties of NE-213 and BC-501 liquid scintillators.

| Scintillator type | density(g/cm$^3$) | Hydrogen/Carbon ratio | Wave length of maximum light emission (nm) |
|---|---|---|---|
| NE-213 | 0.874 | 1.213 | 425 |
| BC-501 | 0.901 | 1.287 | 425 |

while the other neutron passes through it without interacting and is detected by the Bicron detector.

In a ring-Bicron pair, the ring detector's center opening subtends approximately the same solid angle as the active volume of the Bicron detector behind it. One neutron from an *nn* FSI event is detected by the ring detector, while the other neutron travels through the ring's opening and is detected by the Bicron detector.

The Bicron detectors are located $2.5 \pm 0.005$ m from the center detector, while ring and transmission detectors are $1.5 \pm 0.005$ m from it. All detectors are mounted on aluminum holders and placed on iron stands bolted to the concrete floor. All detectors have their height adjusted with the aid of a telescope, so that the center of their faces are in the horizontal plane of the neutron beam (about 1.77 m from the lab floor).

## 2.4 Detector Electronics

### 2.4.1 Neutron Detectors

The neutron detectors' anode signals are used for the following:

1. To provide a stop signal for TOF measurements.

2. For pulse-shape discrimination between $\gamma$ rays and neutrons.

3. To set a hardware lower-level detection threshold. This threshold is always set below

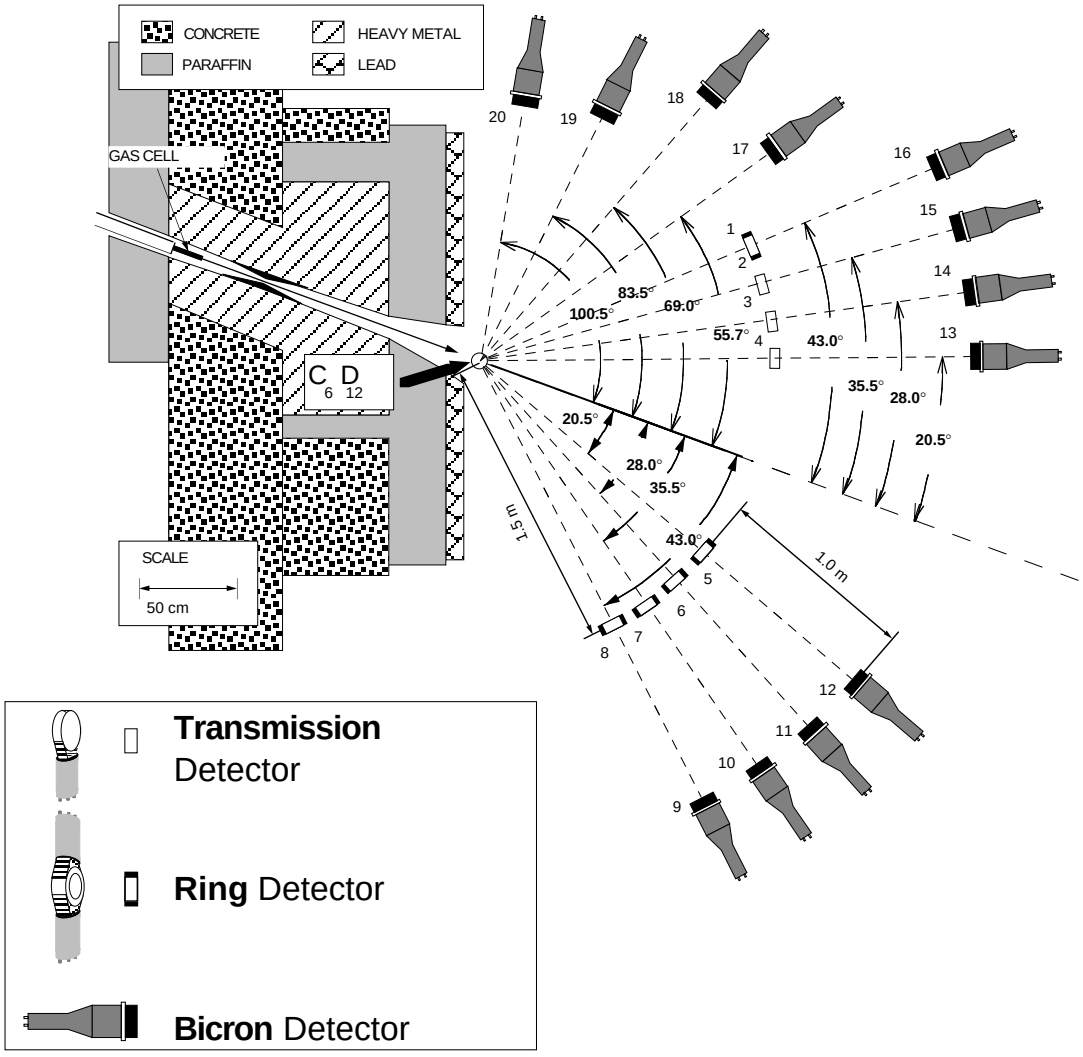


Figure 2.4: Layout of detectors in the TUNL Shielded Neutron Source experimental area.

one-third the pulse height of the Compton edge of $^{137}$Cs, which corresponds to a neutron energy of about 900 keV.

4. To help provide an input logical signal for the computer trigger circuit.

5. To strobe pulse-shape discriminators.

The ring detectors have two PMTs whose anode signals are summed passively at the target area using "T" coaxial junctions.

The neutron detectors' dynode signals are integrated by Ortec 113 or by TUNL preamplifiers. The two dynode signals from a ring detector are summed either passively at the end of 60 cm cables right before the input of an Ortec 113 preamplifier, or summed actively through the double inputs of a TUNL preamplifier. The resulting integrated signal is amplified and sent to an Analog-to-Digital Converter (ADC) to be used for pulse-height analysis.

The neutron detector electronics are associated in pairs because of limited availability of PSD NIM modules and ADC channels. Figure 2.5 shows the detection electronics associated with detector pair #1, consisting of detectors one and five. A list of electronic pairs with their corresponding detectors is given in Table 2.2. The constant-fraction discriminator signal of each detector belonging to an electronic pair is directed into a logical OR, whose output in coincidence with a center detector logic signal (see Figure 2.6) provides an input to the computer trigger circuit.

### 2.4.2 Center Detector

The center detector (CD) anode signal provides timing information from breakup and elastic scattering events occurring in the deuterated liquid scintillator target. The CD anode signal is taken into a CFD which determines a pulse-height rejection threshold to decrease noise and pile-up from low pulse-height events. The threshold is typically set below one-tenth of the pulse height for the Compton edge of a $^{137}$Cs $\gamma$ ray source.

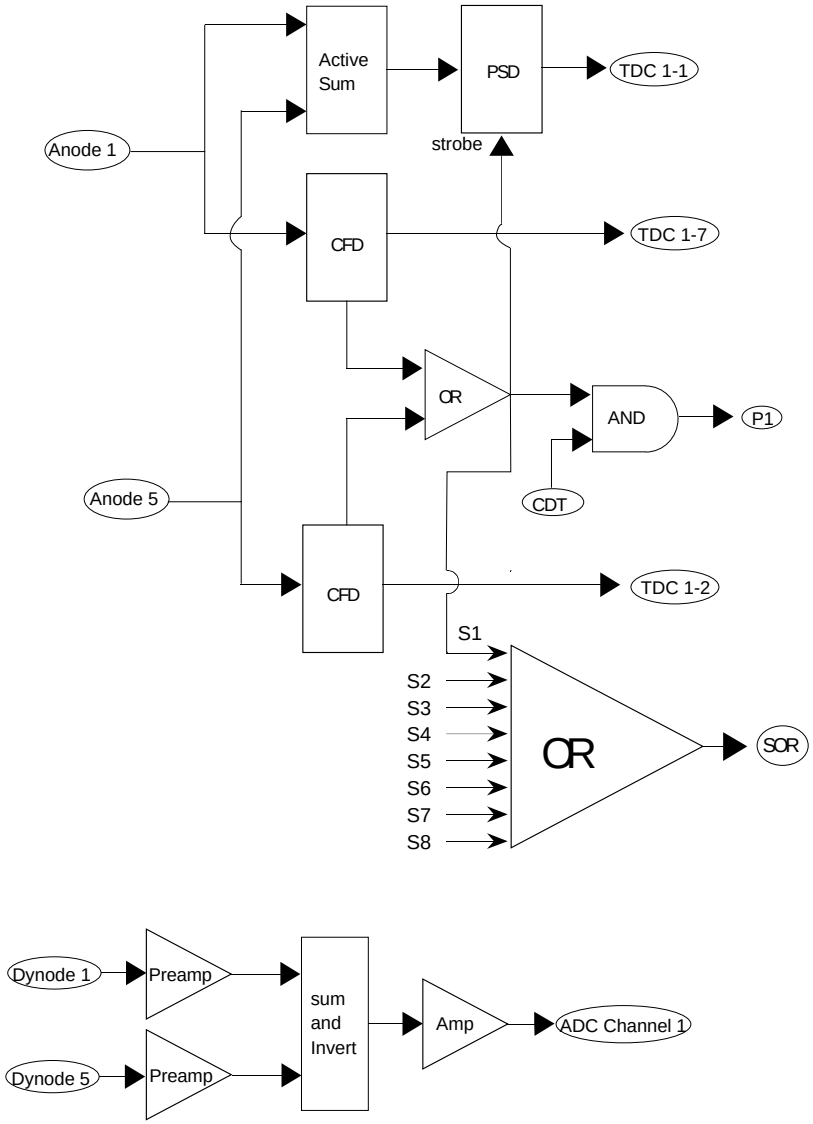


Figure 2.5: Simplified electronics diagram for neutron detector electronic pair #1.

Table 2.2: Electronic pair assignment.

| Electronic Pair # | Detectors |
|---|---|
| 1 | 1,5 |
| 2 | 2,6 |
| 3 | 3,7 |
| 4 | 4,8 |
| 5 | 9,13 |
| 6 | 10,14 |
| 7 | 11,15 |
| 8 | 12,16 |
| 9 | 17,19 |
| 10 | 18,20 |

Pulses from dynodes 10 and 11 (Low and High) are necessary to cover the full range of CD pulse heights of interest. These dynode pulses are independently amplified and then selected at linear gate modules by the coincidence output from the computer trigger (see Figure 2.7), decreasing the frequency of CD linear signals from $\sim$ 400 kHz down to $\sim$ 100 Hz. Finally, the gated linear High and Low pulses go to slow amplifiers whose outputs are digitized by ADCs.

The center detector is set up to run in "beam" or "source" mode. In "source" mode the single OR (SOR) logic signal from the neutron detectors is combined in a logical AND to a negative DC signal from the source/beam module. Every stop signal from the neutron detectors then generates a computer trigger start and events are accepted without any coincidence requirement. A $^{137}$Cs pulse-height spectrum for every neutron detector is accumulated in this fashion every twelve hours. The stability of every neutron detector gain is monitored by determining the Compton edge of its $^{137}$Cs pulse-height spectrum. When running in "beam" mode, the center detector's CFD output is combined with a negative DC

signal from the source/beam module into a logical AND. This introduces the requirement that any input signal for the computer trigger must be a coincidence between the center detector and a neutron detector. Alternation between "beam" and "source" mode is done by means of a switch at the source/beam module.

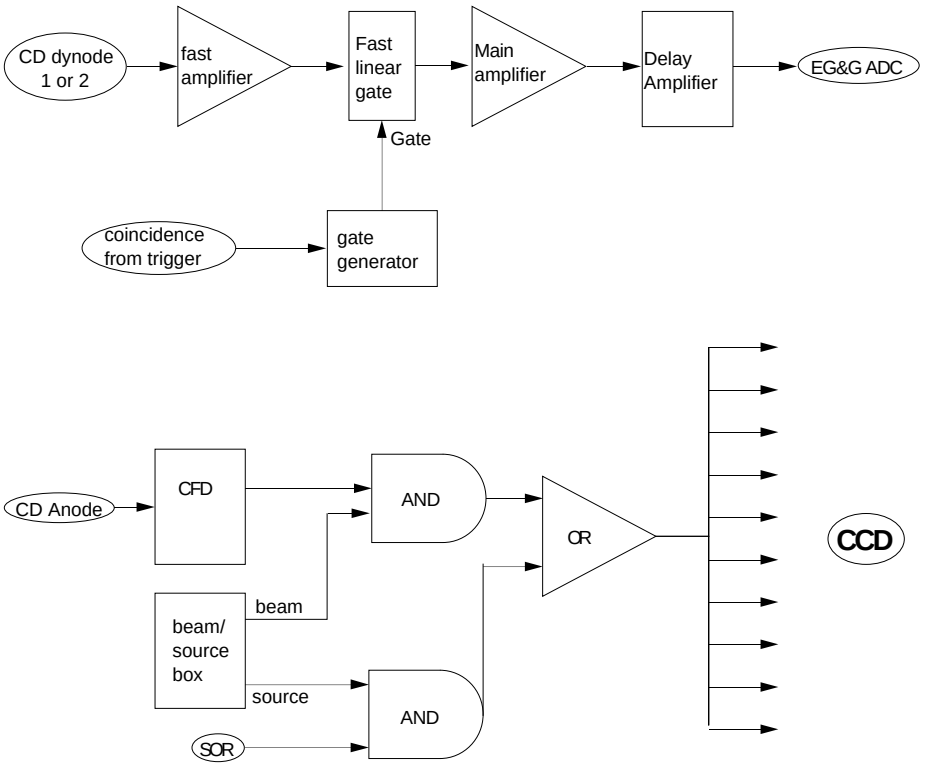


Figure 2.6: Electronics diagram for the center detector.

### 2.4.3 Computer Trigger

The computer trigger circuit provides common start signals and gates for the TDCs and ADCs. The trigger's coincidence output is used by fast linear gate modules to select

CD linear signals. The input signals for the computer trigger consist of electronic pairs designated P1, P2, P3, etc., where each neutron detector in a pair is in coincidence with the center detector and no coincidences are required between neutron detectors forming an electronic pair (see Figure 2.5). P1 through P4 are combined into a logical OR group. The same is done with P5 through P8 (see Figure 2.7). All triple coincidences of interest ($nn$ FSI) will occur between two neutron electronic pairs not belonging to the same logical OR group. The output signals from these two OR groups are either combined in a logical AND (for triple coincidences) or a logical OR (for double coincidences). When a triple coincidence is registered, the associated double-coincidence signals are vetoed so as not to double-count an event as both triple and double.

Because of the large rate of double events it is necessary to implement a divide-down circuit (see Figure 2.9). This is accomplished by branching the doubles signal and introducing a dead time in one of the branches by increasing the signal's width using a gate generator. Both branches then recombine in a logical AND. Typical doubles dividing factors used during the experiment are $\sim 22$.

A fast-clear circuit is implemented to insure that after every registered event the TDCs are properly reset (see Figure 2.8). A computer trigger start signal vetoes any further starts until the OLAM#1 signal (see section 2.4.4) turns on the TDCs' "clear" function, resetting their hit registers and front ends, and stopping digitization.

An LED pulser system is set up to determine the dead time losses for double and triple coincidences (see Figure 2.10). Two independent LED pulser drivers are used with rates of $\sim 6$ Hz. Double pulser events are obtained by simultaneous LED firing in the center detector and neutron detector 9. Triple pulser events come from simultaneous LED firing in the center detector, detector 20 and detector 12. Both pulser drivers send trigger signals to separate scaler channels. In addition, electronic pulsers were coupled to the ADC and TDC signals for each pair of detectors (see Appendix 2.9), and were used to measure the dead time of the computer. The correction associated with the computer dead time was

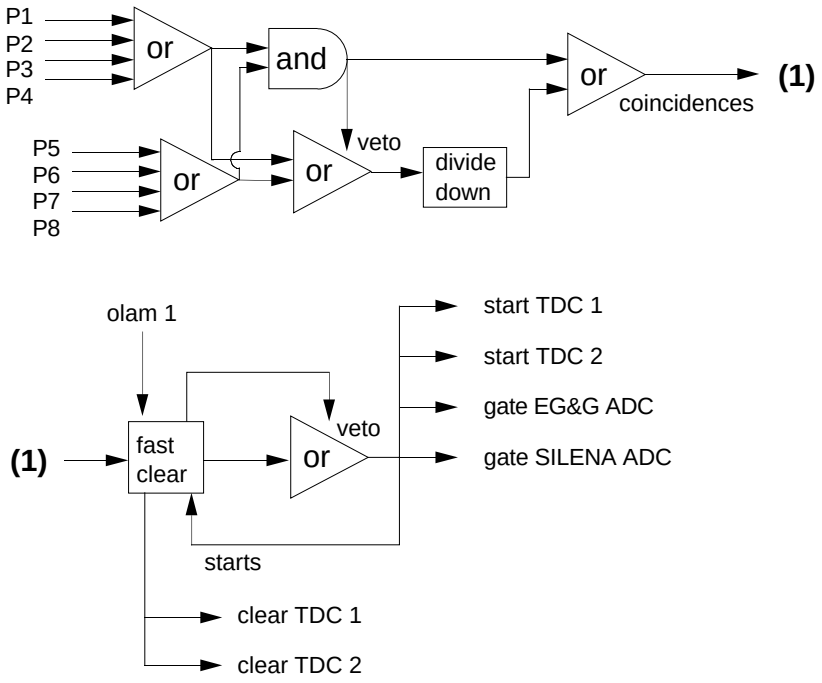


Figure 2.7: Simplified computer trigger electronics diagram.

$\sim 1.06$.

### 2.4.4 CAMAC Electronics

TDCs and ADCs in a CAMAC (Computer Automated Measurements and Control) crate are used for data digitalization. Table 2.4.4 shows the arrangement of stop TOF and PSD signals going into the two TDCs. The computer trigger provides the common start for the TDCs and master gates for the ADCs.

The start signals are vetoed either by the crate inhibit which is activated whenever

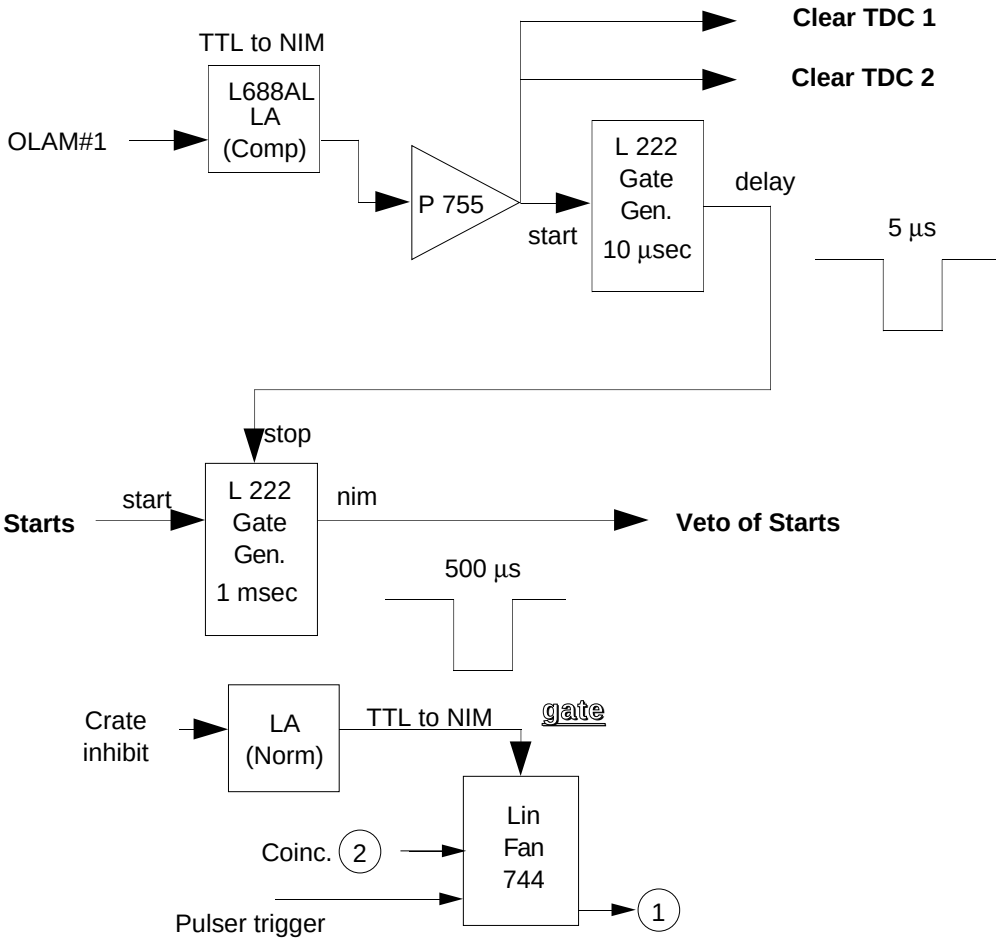


Figure 2.8: Fast-clear circuit for TDCs and crate inhibit for the start signals.

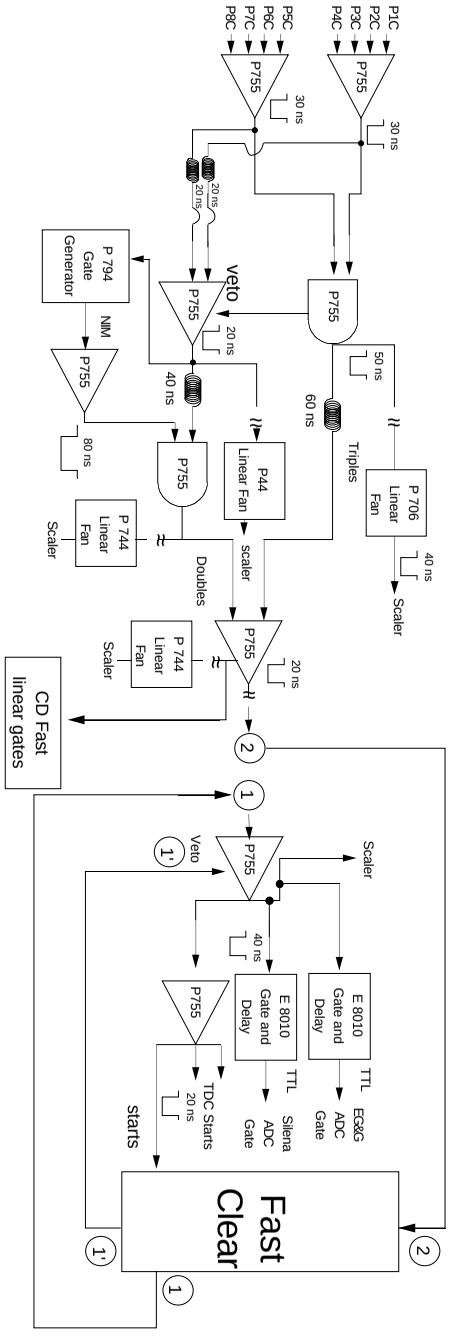


Figure 2.9: Computer trigger electronics diagram.

data are not being taken, or by the OLAM#1 signal generated by any of the CAMAC modules in use. A LAM (Look at Me) signal is given by a TDC or ADC that has digitized a pulse and is ready to send information to the computer. An OLAM consists of the logical OR of the LAMs from all TDCs and ADCs. When an OLAM signal is raised, the computer reads the information digitized in all modules. Once the OLAM signal falls, the fast-clear circuit resets both TDCs. A 5 $\mu s$ delay follows to allow the TDCs enough time to reset before the start veto signal ends and the next event is digitized and read by the computer.

Table 2.3: TDC configuration for stop TOF and PSD signals.

| TDC | TDC 1 | | TDC 2 | |
|---|---|---|---|---|
| slot | PSD signal | TOF Signal | PSD signal | TOF signal |
| 1 | 1 | | 2 | |
| 2 | 3 | | 4 | |
| 3 | 5 | | 6 | |
| 4 | 7 | | 8 | |
| 5 | 9 | | 10 | |
| 6 | - | - | - | - |
| 7 | | 1 | | 2 |
| 8 | | 3 | | 4 |
| 9 | | 5 | | 6 |
| 10 | | 7 | | 8 |
| 11 | | 9 | | 10 |
| 12 | | 11 | | 12 |
| 13 | | 13 | | 14 |
| 14 | | 15 | | 16 |
| 15 | | 17 | | 18 |
| 16 | | 19 | | 20 |

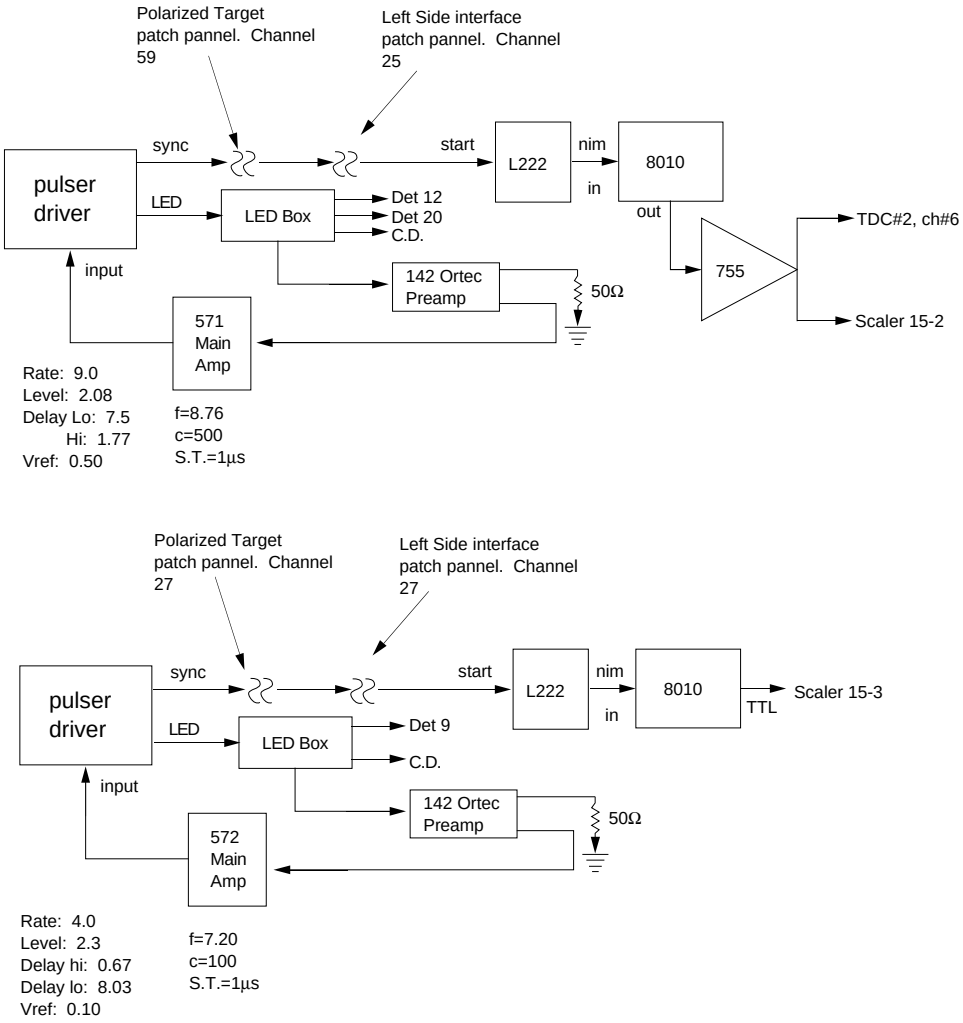


Figure 2.10: LED pulser electronic diagram.

# Chapter 3

# Theory

## 3.1 Introduction

The framework for the solution to the three-nucleon (3N) problem was proposed by Faddeev in 1960 [Fad61]. He introduced a set of coupled equations expressed in terms of solutions to pair-wise interactions, and proved that this set has a unique solution for short-ranged forces.

The unavailability of adequate computing power at that time forced the search for simplified versions of the Faddeev scheme. Finite-rank t-matrix approximations were pursued by Lovelace [Lov64], leading to coupled sets of one-dimensional integral equations which were numerically tractable.

Separable nucleon-nucleon (NN) potentials like the spin-dependent s-wave Yamaguchi forces provided qualitative insights into the 3N problem and were used in numerous sensitivity studies of 3N observables [Aar65]. It soon became clear that more realistic NN forces and an exact treatment of the Faddeev equations were necessary to carry out meaningful comparisons between theoretical predictions and experimental data.

With the advent of more powerful computers and improved numerical techniques it became feasible to solve the Faddeev equations to the desired accuracy using arbitrary

short-range potentials [Wit88]. For the analysis of the TUNL $nd$ breakup experiment we rely on a computer program[1] which solves the Faddeev equations numerically [Glö96] using the Bonn-B Potential [Mac87]. This program calculates $nd$ breakup cross sections in narrow angle and energy steps relevant to the TUNL experimental setup. These cross sections were included in libraries which are used in a Monte-Carlo simulation of the experiment.

## 3.2 Meson-Exchange Theory and the Bonn-B Potential

The meson-exchange theory[2] of the NN interaction was introduced in 1935 by Yukawa's hypothesis that internucleon forces were mediated by a massive particle, in agreement with the empirical observation of the short range of the NN interaction. The initial idea of a scalar field interaction was quickly extended to pseudoscalar and pseudovector fields.

The splitting of the nuclear interaction into three regions was proposed by Taketani, Nakamura and Sasaki (TNS) in 1951 [Tak51]. The first (classical) region corresponds to internucleon distances $r \gtrsim 2$ fm, and is dominated by single-pion (1-$\pi$) exchange. The second region (dynamical) corresponds to $1 \lesssim r \lesssim 2$ fm and is characterized by two-pion (2-$\pi$) and heavy-meson ($\omega$) contributions to the interaction. The third region (core) is dominated by short-ranged ($r \lesssim 1$ fm) interactions consisting of multi-pion, heavy-meson and quark-gluon exchanges. The TNS conjecture is of great value since it allows for a step-wise approach to the modeling of nuclear forces based on the range of the contributing meson-exchange interactions.

The Bonn potential [Mac87] is a field-theoretical meson-exchange model for the NN interaction below the pion production threshold. Form-factor cutoff masses of 1.3 and 1.2 GeV are used for $\pi NN$ and $\pi N\Delta$-type diagrams, respectively. The Bonn potential is built on a series of meson-exchange terms.

[1] Program supplied by H. Witała of the Bochum-Cracow theory group

[2] The meson-exchange picture is presently regarded as an effective interaction model of the fundamental QCD theory, but in the context of NN interactions it is still traditionally referred to as a theory.

1. One-Meson Exchange Contributions: In the classical range we have pions as the main intermediaries of the nuclear interaction, which is mostly tensor in character. The strong spin-orbit interaction is provided by the $\omega$ meson (783 MeV) which also provides a short-range repulsion. In addition, a $\delta$-meson exchange is included for a consistent description of the s-wave phase shifts, but constitute a very small effect.

2. 2-$\pi$ Exchange Contribution: Nucleon resonances ($\Delta$) and two-pion exchanges have their greatest effect in the dynamical region. These diagrams are responsible for the attractive character of the nuclear force in this range. It is important to include the effect of correlated 2-$\pi$ exchanges which account for roughly two-thirds of the strength of the total 2-$\pi$ exchange.

3. $\pi$-$\rho$ Exchange Contributions: These diagrams give the core region its repulsive characteristic and have their greatest effect on the lower partial-wave states ($^1S_0$, $^3P_1$, $^3P_0$). They compensate for the excessive attractive effect of the 2-$\pi$ contribution in this region.

In order to carry out practical (one-boson exchange) calculations, the 2-$\pi$ and $\pi$-$\rho$ contributions are replaced by the exchange of a fictitious $\sigma$ meson. The parameters related to the $1-\pi$, $\rho$ and $\omega$-meson exchanges are kept almost unchanged while the $\sigma$ and $\delta$ parameters are tuned to reproduce the properties of the deuteron (binding energy, quadrupole moment, D-state probability, magnetic moment, etc.) and low-energy NN scattering observables (neutron-proton $^1S_0$ scattering length, $^1S_0$ effective range, etc.). This parameterization is referred to as the Bonn-B OBEPQ (one-boson exchange parameterization in momentum space), and is tuned to give the value $a_{np} = -23.748$ fm for the $^1S_0$ $np$ scattering length (experimental value is $a_{np} = -23.748 \pm 0.010$ fm [Mac87]). In the scattering of nucleons on deuterons both $np$ and $nn$ forces are present, and theoretical calculations must be performed for both kinds of $^1S_0$ interactions, introducing charge dependence. In order to analyze the TUNL $nd$ breakup experimental data we calculated theoretical cross-section libraries

corresponding to different values of $a_{nn}$ by modifying the $\sigma$ coupling-constant value for the $^1S_0$ part of the Bonn-B potential.

## 3.3 3N Breakup Formalism

### 3.3.1 NN Forces

Because the Faddeev equations are given in terms of solutions to two-body (NN) problems, we need to introduce the NN t-matrix. This operator, given by Equation 3.1, is defined as the probability amplitude for a particle to make the transition from an initial state $\mid \alpha\rangle$ to a final state $\mid \beta\rangle$ when encountering a potential $V$

$$t_{\beta\alpha} = \langle \beta \mid t \mid \alpha \rangle. \tag{3.1}$$

The t-matrix obeys the Lippmann-Schwinger equation

$$t = V + VG_0t, \tag{3.2}$$

where $G_0$ is the free propagator

$$G_0 = \frac{1}{E + i\varepsilon - H_0}, \tag{3.3}$$

$H_0$ is the free Hamiltonian, and $E$ is the energy of the two-nucleon system.

We now consider a system of three nucleons. Initially particles 2 and 3 are bound forming the deuteron and particle 1 is free. In the final state all nucleons are free. The breakup operator ${U_0}^{(1)}$ acting on the initial state $\phi_1$ (where the subscript refers to the free particle) is expressed by the infinite series

$${U_0}^{(1)}\phi_1 = V_3\phi_1 + V_2\phi_1 + V_1G_0V_3\phi_1 + V_3G_0V_2\phi_1 + ..., \tag{3.4}$$

where $V_i = V_{jk}$ is a pair-wise interaction between particles $j$ and $k$, and $G_0$ is the three-body free propagator. This multiple-scattering series corresponds to a simple physical picture of the 3N scattering as a sum of contributions from processes where nucleons interact for an

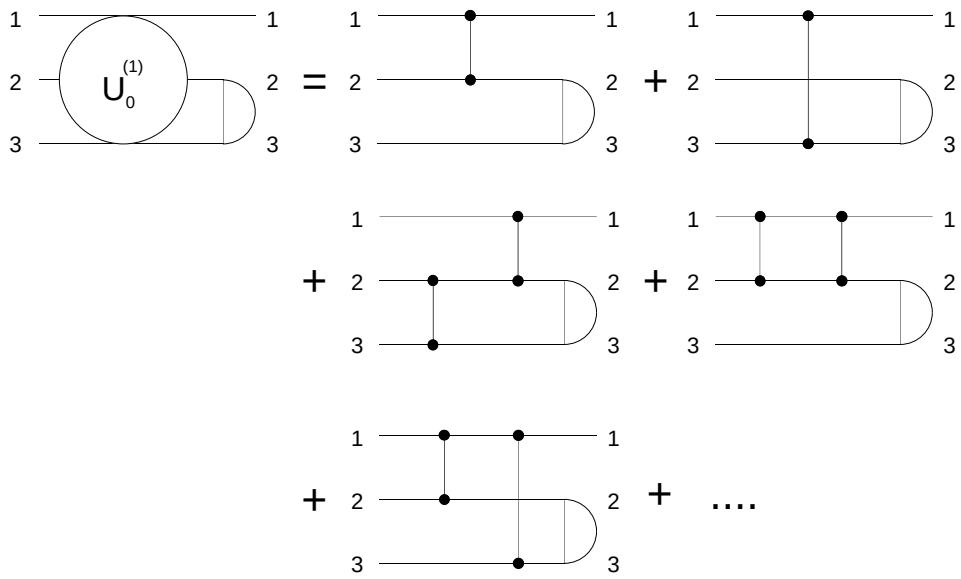


Figure 3.1: Infinite multiple-scattering series for the *nd* breakup reaction. The initial state consists of nucleons 2 and 3 forming a deuteron and nucleon 1 is free. In the final state all three nucleons are free. All the physics of the reaction are contained in this sum over terms composed of interactions within all pairs of nucleons and free propagations in between [Glö96].

instant and then move freely (see Figure 3.1). The right-hand side of Equation 3.4 can be rearranged into three groups so that each group contains terms ended from the left on a particular interaction $V_i$

$$\begin{aligned} {U_0}^{(1)}\phi_1 = &(V_3 + V_3G_0V_3 + V_3G_0V_2 + ...)\phi_1 \\ &+ (V_2 + V_2G_0V_2 + V_2G_0V_2 + ...)\phi_1 \\ &+ (V_1G_0V_2 + V_1G_0V_1G_0V_2 + ...)\phi_1 \\ \equiv &({U_0}^{(1,3)} + {U_0}^{(1,2)} + {U_0}^{(1,1)})\phi_1. \end{aligned} \tag{3.5}$$

From the above definition we see that ${U_0}^{(1,i)}$ satisfies the following system of coupled equa-

tions

$$\begin{aligned} {U_0}^{(1,3)}\phi_1 &= V_3\phi_1 + V_3G_0({U_0}^{(1,3)} + {U_0}^{(1,2)} + {U_0}^{(1,1)})\phi_1 \\ {U_0}^{(1,2)}\phi_1 &= V_2\phi_1 + V_2G_0({U_0}^{(1,3)} + {U_0}^{(1,2)} + {U_0}^{(1,1)})\phi_1 \\ {U_0}^{(1,1)}\phi_1 &= \qquad V_1G_0({U_0}^{(1,3)} + {U_0}^{(1,2)} + {U_0}^{(1,1)})\phi_1. \end{aligned} \tag{3.6}$$

Solving for the operator ${U_0}^{(1,i)}$ on the left-hand side of Equations 3.6 and introducing the two-body t-matrices $t_i$ generated by $V_i$

$$t_i = V_i + V_iG_0t_i, \tag{3.7}$$

we obtain the following set of three coupled Faddeev equations

$$\begin{aligned} U_0^{(1,3)}\phi_1 &= t_3\phi_1 + t_3G_0(U_0^{(1,2)} + U_0^{(1,1)})\phi_1 \\ U_0^{(1,2)}\phi_1 &= t_2\phi_1 + t_2G_0(U_0^{(1,3)} + U_0^{(1,1)})\phi_1 \\ U_0^{(1,1)}\phi_1 &= \qquad t_1G_0(U_0^{(1,3)} + U_0^{(1,2)})\phi_1. \end{aligned} \tag{3.8}$$

Working in isospin formalism and treating nucleons as identical particles, the properly antisymmetrized breakup amplitude $U_0$ is written as

$$U_0\phi_1 \equiv U_0^{(1)}\phi_1 + U_0^{(2)}\phi_2 + U_0^{(3)}\phi_3 = \sum_i \sum_k U_0^{(i,k)}\phi_k \equiv \sum_i U_{0,i}\phi_1. \tag{3.9}$$

Introducing the permutation operator $P_{ij}$ which exchanges nucleons $i$ and $j$ one has

$$U_{0,2} = P_{12}P_{23}U_{0,1} \tag{3.10}$$

and

$$U_{0,3} = P_{13}P_{23}U_{0,1}. \tag{3.11}$$

Thus, for identical nucleons, knowledge of only $U_{0,1}$ is sufficient.

Defining the $P$, $T$ and $t$ operators as

$$P \equiv P_{13}P_{12} + P_{23}P_{12}, \tag{3.12}$$

$$T \equiv U_{0,1}, \tag{3.13}$$

and

$$t \equiv t_1, \tag{3.14}$$

the Faddeev equations can be rewritten in the compact form

$$T = tP + tPG_0T, \tag{3.15}$$

resulting in the three-body breakup amplitude

$$U_0 = (1 + P)T. \tag{3.16}$$

When describing 3N systems we use the Jacobi linear and angular momentum coupling scheme shown in Figure 3.2 to parameterize the relative motion of the three nucleons. The Jacobi momenta are defined in the standard way by

$$\vec{p}_i = \frac{1}{2}(\vec{k}_j - \vec{k}_k), \tag{3.17}$$

$$\vec{q}_i = \frac{2}{3}(\vec{k}_i - \frac{1}{2}(\vec{k}_j - \vec{k}_k)), \tag{3.18}$$

where $\vec{k}_{i,j,k}$ are the momenta of the three particles in the laboratory frame. Introducing the basis of momentum states $\mid pq\alpha\rangle$ defined as

$$\mid \phi_0\rangle = \mid pq\alpha\rangle = \mid pq(ls)j(\lambda\frac{1}{2})IJ(t\frac{1}{2})T\rangle \tag{3.19}$$

and performing partial-wave decomposition of Equation 3.15 in this basis, one obtains an infinite system of coupled two-dimensional integral equations for $\langle\phi_0 \mid T \mid \phi\rangle$ amplitudes, where $\mid \phi\rangle$ is the initial state (nucleon + deuteron) and $\mid \phi_0\rangle$ is the final state (three-nucleons after *nd* breakup). In the case of the TUNL experiment, the partial-wave expansion can be truncated at $j = 3$ ($j$ is the two-nucleon total angular momentum), reducing the number of coupled integral equations to about sixty.

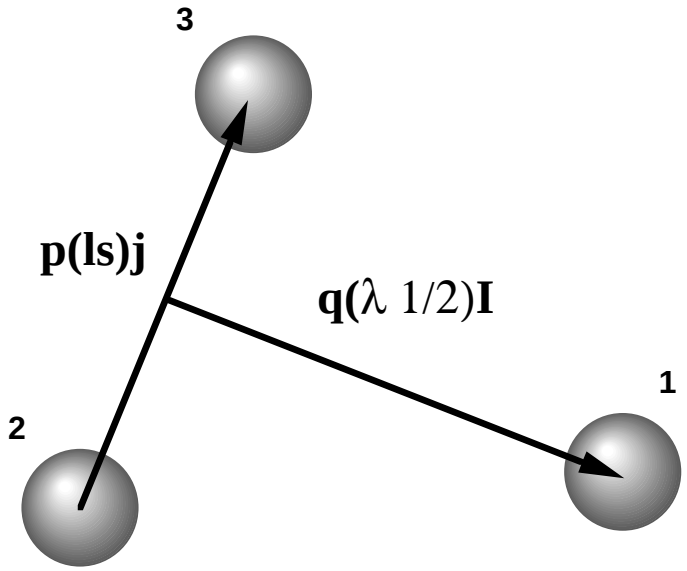


Figure 3.2: Jacobi linear and angular momentum coupling scheme for the three-nucleon system. The relative momentum between particles 2 and 3 is $p$. The angular momentum and total spin of the 2-3 sub-system are $l$ and $s$, and the total angular momentum is $j$. The relative momentum between particle 1 and the center of mass of the 2-3 sub-system is $q$. The corresponding orbital angular momentum is $\lambda$ and the spin of nucleon 1 is $\frac{1}{2}$, which couple to give the total angular momentum $I$.

### 3.3.2 Three-Body Forces

Three-body forces (3NF) in nuclear physics are dependent in an irreducible way on the coordinates of the three nucleons. These types of forces must exist in the three-nucleon system, but their form, properties and extent to which they contribute to the 3N observables are still being investigated.

Underlying QCD interactions can manifest themselves as 3NFs due to the suppression of quark and gluon degrees of freedom in the meson-exchange picture of the NN force. Therefore, the addition of a 3NF to a meson-exchange potential model may be viewed as a way of parameterizing the underlying physics in order to model effects that are not

well-known or calculable.

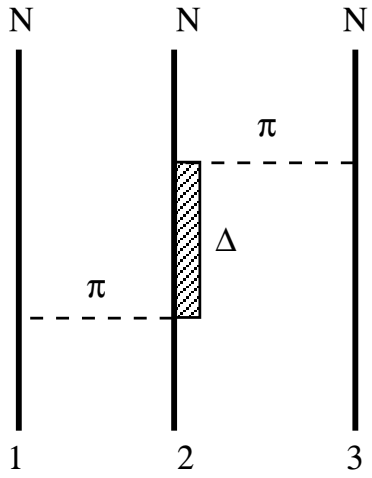


Figure 3.3: 3NF diagram due to 2-$\pi$ exchange and a $\Delta(1232)$ excitation in a three-nucleon system.

In the meson-exchange picture, three-body forces arise due to two-meson exchange processes (e.g. 2-$\pi$ exchange) as shown in Figure 3.3. The Tucson-Melbourne (TM) 3NF [Coo79] is based on this class of diagrams, where the pions exchanged are off-mass shell and space-like.

The addition of a three-body force modifies the 3N Faddeev equations obtained for the case of pure two-nucleon interactions. Allowing for a 3NF contribution $V_4$ to the potential energy of the 3N system and following steps similar to those in Section 3.3.1 we obtain a set of two coupled operator equations for $T$ and $T_4$

$$T = tP + tG_0(PT + T_4), \tag{3.20}$$

$$T_4 = t_4(1 + P) + t_4G_0(1 + P)T, \tag{3.21}$$

with $t_4$ generated by a three-body force $V_4$

$$t_4 = V_4 + V_4G_0t_4. \tag{3.22}$$

The symmetrized transition breakup operator is then given by

$$U_0 = (1 + P)T + T_4. \tag{3.23}$$

The Bochum-Cracow group carried out calculations to test the sensitivity of $nn$ FSI cross sections to the TM 3NF using $j \leq 2$ for all NN and 3NF interactions ($j$ is the total two-particle sub-system angular momentum, see Figure 3.4). These 3NF cross-section calculations used a standard form-factor cutoff parameter $\Lambda = 5.8\mu$ ($\mu = 139.6$ MeV), which when used in conjunction with the Bonn-B NN potential, overbinds the $^3$H by 1.84 MeV. The Bonn-B OBEPQ was used for the NN part of the interaction [Wit96]. For $\theta_{nn} \lesssim 43^\circ$ the $nn$ FSI peak cross section is enhanced by the TM 3NF. Correcting the $nn$ FSI cross section for this effect would lead to less negative values of $a_{nn}$, taking the kinematically complete $nd$ breakup $a_{nn}$ values further away from those extracted from $\pi$-d experiments. At $\theta_{nn} = 20.5^\circ$, for example, the TM 3NF would introduce a $\Delta a_{nn} = a_{nn}(NN) - a_{nn}(NN + 3NF) \approx 2.0$ fm. This indicates that the TM 3NF force cannot account for the present discrepancy between $a_{nn}$ values extracted from kinematically-complete $nd$ breakup and $\pi$-d measurements, but it may indicate the production angle $\theta_{nn}$ dependence as the probable effect of a 3NF on the $nn$ FSI cross sections.

### 3.3.3 Breakup Cross Sections

From time-dependent scattering theory we know that the transition rate for the breakup process between an initial state $\mid \phi\rangle$ (composed of a nucleon moving with relative momentum $\vec{q}_o$ with respect to the deuteron) and a final state $\mid \phi_0\rangle$ is given by

$$\begin{aligned} dN &= 2\pi |\langle \phi_0 \mid U_0 \mid \phi \rangle|^2 \int d\vec{p} d\vec{q} \delta(\frac{3q_0^2}{4m} + \epsilon_d - \frac{p^2}{m} - \frac{3q^2}{4m}) \\ &= 2\pi |\langle \phi_0 \mid U_0 \mid \phi \rangle|^2 k_E d\Omega_1 d\Omega_2 dE_1, \end{aligned} \tag{3.24}$$

where $k_E$ is the phase-space factor or density of final states. It is convenient to use the phase-space factor $k_E$ to obtain a new phase-space factor $k_S$ for solid angles $d\Omega_1$, $d\Omega_2$ and

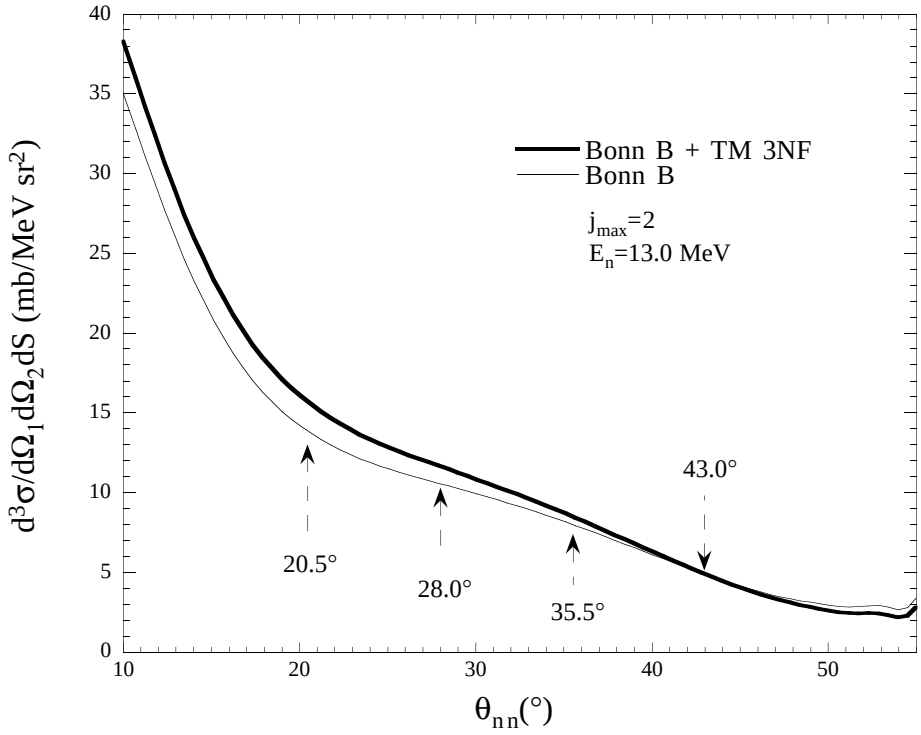


Figure 3.4: The Tucson-Melbourne 3NF (cutoff parameter $\Lambda = 5.8\mu$) effect on the $nn$ FSI cross-section peak for the production angles $\theta_{nn}$ considered in the TUNL $nd$ breakup experiment ($j \leq 2$). If the TM model is correct, then for $\theta_{nn} = 43.0^\circ$ the 3NF effect on the cross section vanishes, making it an ideal configuration from which to extract $a_{nn}$.

an interval on the kinematic S-curve $dS$ (see Section 1.0.2). In terms of $\vec{k}_i$ and the projectile laboratory momentum $\vec{q}_0$ we get

$$k_S \equiv k_E \frac{dE_1}{dS} = \frac{m^2 k_1^2 k_2^2}{\sqrt{k_1^2(2k_2 - \hat{k}_2 \cdot (\vec{q}_0 - \vec{k}_1))^2 + k_2^2(2k_1 - \hat{k}_1 \cdot (\vec{q}_0 - \vec{k}_2))^2}}. \tag{3.25}$$

The $nd$ breakup cross section can then be obtained by dividing the transition rate given by Equation 3.24 by the projectile particle flux ($\frac{3q_0}{2m}$), obtaining

$$\frac{d^3\sigma}{d\Omega_1 d\Omega_2 dS} = (2\pi)^4 |\langle \phi_0 \mid U_0 \mid \phi \rangle|^2 \frac{2m}{3q_0} k_S. \tag{3.26}$$

The final breakup state of the nucleon system is given by

$$\mid \phi_0 \rangle = \mid \vec{k_1} m_1 \vec{k_2} m_2 \vec{k_3} m_3 \rangle, \tag{3.27}$$

where $\vec{k_i}$ are laboratory momenta of the nucleons and $m_i$ their spin projections. The initial state is composed of a neutron and a deuteron (wave function $\psi_{m_d}$) having spin projections $m_n$ and $m_d$, respectively, and relative momentum $\vec{q}_0$

$$\mid \phi \rangle = \mid \psi_{m_d}, \vec{q}_0, m_n \rangle. \tag{3.28}$$

Because we are using an unpolarized beam in the TUNL experiment and we do not select outgoing spin states, we must average over the initial magnetic quantum numbers and sum over the final ones. This introduces a statistical spin factor

$$g = \frac{1}{(2s_d + 1)(2s_N + 1)} = \frac{1}{6}, \tag{3.29}$$

where $s_d$ is the spin of the deuteron and $s_N$ is the spin of the nucleon. Therefore, the breakup cross section for an unpolarized beam and target is

$$\frac{d^3\sigma}{d\Omega_1 d\Omega_2 dS} = \frac{1}{6}(2\pi)^4 \sum_{m_1, m_2, m_3} |\langle \phi_0 \mid U_0 \mid \phi \rangle|^2 \frac{2m}{3q_0} k_S. \tag{3.30}$$

Further details on the technical aspects of the calculations, accuracy tests and applications can be found in [Glö96] and [Fri95].

# Chapter 4

# Monte-Carlo Simulations

## 4.1 Introduction

In order to analyze the experimental *nd* breakup data we made use of Monte-Carlo (MC) Fortran programs to simulate two general processes: *nd* breakup and *nd* elastic scattering. The code was written with a three-fold aim:

1. To calculate the background due to multiple scattering (MS) in the *nd* elastic scattering center detector pulse-height spectrum.

2. To determine appropriate kinematic gates to use on the *nd* breakup experimental data analysis, while accounting for finite-geometry and energy-resolution effects of the experimental setup.

3. To calculate theoretical *nn* FSI cross sections including finite-geometry and energy-resolution effects of the experimental setup.

The *nd* breakup MC code uses a set of cross-section libraries stored as text files.

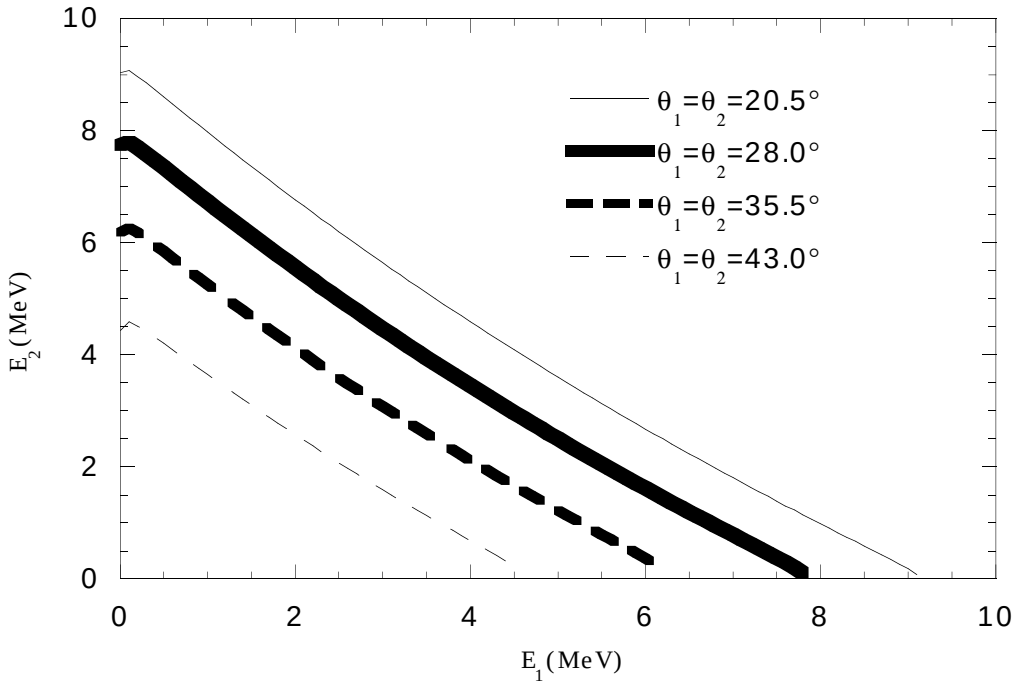


Figure 4.1: Point-geometry S-curves for several $nn$ FSI configurations, with $\phi_{12} = 0°$, $E_0 = 13.0$ MeV.

## 4.2 Cross-Section Libraries

Extensive ($\sim 10^5$ points) $nd$ breakup differential cross-section libraries were created for the $nn$ FSI configurations of interest. These libraries are required to span the finite geometry of the experimental setup and the energy spread of the incoming neutron beam.

Differential cross sections were generated along kinematic S-curves for breakup configurations determined by the $nn$ production angles $\theta_1, \theta_2, \phi_{12}$, and the incoming neutron beam energy $E_n$ (see Figure 4.1). The point-geometry theoretical $nd$ breakup differential

cross sections $\frac{d^3\sigma_t}{d\Omega_1 d\Omega_2 dS}(S)$ are given as a function of S-curve length (see Section 1.0.2) in steps of 0.1 MeV, always starting at the point where $E_2 = 0$ MeV. The $nn$ FSI differential cross section has a characteristic enhancement in the neighborhood of the S-curve point where $E_1 = E_2$. This enhancement is very sensitive to the $^1S_0$ part of the $nn$ interaction [Wit96]. The origin of the sensitivity is in the presence of an anti-bound state in the $nn$ interaction, which gives a virtual-state pole in the $^1S_0$ NN t-matrix. This pole leads to a $q$-dependence of the T-matrix of the form

$$\langle pq\alpha|T|\phi\rangle = \mathcal{O}(\frac{1}{\sqrt{E - \frac{3}{4m}q^2} + i\sqrt{\mid E_v \mid}}), \tag{4.1}$$

where $E_v \approx -100$ keV. Thus, when the relative momentum between neutrons 1 and 2 goes to zero ($p \to 0$, $k_1 = k_2$) then the absolute value squared of the T-matrix element and the $nd$ breakup cross section are maximized.

The Bochum-Cracow group prepared a code that uses the Faddeev scheme to rigorously calculate the $nd$ breakup differential cross sections based on the Bonn-B OBEPQ NN potential. The $\sigma$-meson coupling constant $g_\sigma^2/4\pi$ was modified in the code in order to alter the $^1S_0$ component of the $nn$ interaction, yielding different values of $a_{nn}$ (see Table 4.1 [Tor96]) while keeping the $np$ part of the interaction fixed using $a_{np} = -23.748$ fm. All NN force components with total two-body angular momentum $j \leq 3$ are considered. For every experimental $nn$ FSI configuration we created cross-section libraries for $a_{nn} = -16.0$, $-17.0$, $-17.7$, $-18.0$, $-19.0$ and -20.0 fm taking into account the following experimental conditions:

1. The full angular range due to the finite geometry of the experimental setup given by the possible extreme values of $\theta_1$, $\theta_2$, $\phi_{12}$ (see Table 4.2) is spanned.

2. All cross-section curves for $E_0 = 12.8, 13.0$ and 13.2 MeV are calculated in order to account for the energy spread of the neutron beam produced in the gas cell.

3. The angles and incoming neutron energies change in steps such that the variation

Table 4.1: Values for $\sigma$-meson coupling constants and associated effective-range parameters.

| $g_\sigma^2/4\pi$ | $a_{nn}$ (fm) | $r_{nn}$ (fm) |
|---|---|---|
| 8.6023 | -10.0 | 3.06 |
| 8.6543 | -11.0 | 3.00 |
| 8.6980 | -12.0 | 2.96 |
| 8.7353 | -13.0 | 2.92 |
| 8.7676 | -14.0 | 2.88 |
| 8.7957 | -15.0 | 2.85 |
| 8.8204 | -16.0 | 2.83 |
| 8.8423 | -17.0 | 2.81 |
| 8.8620 | -18.0 | 2.79 |
| 8.8796 | -19.0 | 2.77 |
| 8.8955 | -20.0 | 2.76 |
| 8.9099 | -21.0 | 2.74 |
| 8.9231 | -22.0 | 2.73 |
| 8.9351 | -23.0 | 2.72 |
| 8.9462 | -24.0 | 2.71 |
| 8.9564 | -25.0 | 2.70 |
| 8.9659 | -26.0 | 2.69 |
| 8.9747 | -27.0 | 2.68 |

Table 4.2: Angular span of $nn$ FSI libraries due to the finite geometry of the experimental setup.

| configuration | $\theta_{nn}(^\circ)$ | $\theta_1(^\circ)$ | $\theta_2(^\circ)$ | $\phi_{12}(^\circ)$ | $\Delta\theta_1(^\circ)$ | $\Delta\theta_2(^\circ)$ | $\Delta\phi_{12}(^\circ)$ |
|---|---|---|---|---|---|---|---|
| nnfsr1 | 43.0 | 38.5-47.5 | 40.0-46.0 | 0-9.0 | 1.5 | 1.2 | 4.5 |
| nnfsr2 | 35.5 | 31.0-40.0 | 32.5-38.5 | 0-11.0 | 1.8 | 1.2 | 3.7 |
| nnfsr3 | 28.0 | 23.5-32.5 | 25.0-31.0 | 0-13.0 | 1.8 | 1.2 | 4.3 |
| nnfsr4 | 20.5 | 16.0-25.0 | 17.5-23.5 | 0-18.0 | 1.3 | 0.9 | 4.5 |

between cross-section values among the FSI peaks with neighboring angles or incoming neutron energy is $\lessapprox 4\%$.

The calculation of the cross-section libraries took approximately 70 hours of CPU time on Cray Y-MP and T90 supercomputers[1].

## 4.3 Monte-Carlo Codes

### 4.3.1 *nd* Elastic Scattering

The extraction of accurate experimental *nd* elastic scattering yields is of fundamental importance in determining the absolute *nd* breakup cross sections. Neutrons produced by the $^2$H(d,n)$^3$He reaction are incident on the deuterated target scintillator and undergo *nd* elastic scattering onto the neutron detectors. The number of *nd* elastic scattering neutrons detected during a given run $r$ by a detector at a certain angle $\theta$ is denoted $\Upsilon^r_{el}(\theta)$. The yields $\Upsilon^r_{el}(\theta)$ are related to the *nd* elastic-scattering cross section by:

$$\Upsilon^r_{el}(\theta) = (\frac{d\sigma_{lab}}{d\Omega}(\theta))\alpha(E_{el})\varepsilon(E_{el})\beta_r[BCI]_r\Omega, \tag{4.2}$$

where

$$\beta_r = \frac{N^r_n N_d}{[BCI]_r} \tag{4.3}$$

is the luminosity. The energy of the scattered neutron is $E_{el}$, the density of deuterons in the target is $N_d$, the number of neutrons that hit the deuterated target is $N^r_n$ and the total charge deposited by the deuteron beam on the deuterium gas cell during the run $r$ is $[BCI]_r$. The quantity $\alpha(E_{el})$ is the transmission probability of the elastically-scattered neutrons with energy $E_{el}$, taking into account the building materials of the deuterated target and neutron detector and including air attenuation. The absolute detection efficiency for the scattered neutrons is $\epsilon(E_{el})$. The solid angle subtended by the neutron detector is denoted

[1] MCNC, Research Triangle Park, NC-27709-2889

$\Omega$. The $nd$ elastic scattering differential cross-section tables ($\frac{d\sigma_{Lab}}{d\Omega}(\theta)$) were calculated by the Bochum-Cracow group. Once the experimental yield $\Upsilon^r_{el}$ has been properly determined, $\beta_r$ can be found from Equation 4.2. In Chapter 5 we show how $\beta_r$ is used to normalize the $nd$ breakup yields to obtain absolute cross sections. Because of the finite size of the deuterated target, it is possible for beam neutrons to elastically scatter more than once within the target. These multiply-scattered (MS) neutrons and the singly-scattered (SS) neutrons cannot be resolved completely by TOF. Hence the MS neutrons form a background beneath the prominent SS peak in the TOF spectrum (see Figure 4.2) and the associated CD (center detector) pulse-height spectrum (see Figure 4.3). A MC Fortran program was written to calculate the MS neutron contribution to the experimental $nd$ elastic yields, along with the following effects associated with $nd$ elastic scattering:

1. time-of-flight and CD pulse-height resolution effects;
2. finite-geometry effects due to the deuterated target volume and different kinds of neutron detectors; and
3. deuterated target edge effects.

### 4.3.2 $nd$ Breakup

The $nd$ breakup experimental data are distorted by effects such as the finite pulse-height resolution of the center detector, the energy-dependent efficiencies of neutron detectors, the attenuation effects from structural materials and the finite geometry of detectors and target. Instead of trying to extract point-geometry cross sections from the experimental $nd$ breakup data, we model the distorting effects in a Monte-Carlo simulation of the experiment. This requires the calculation of the following quantities:

1. The product of the transmission probabilities of both $nd$ breakup neutrons emitted to the neutron detectors (neutron transmission product)

$$\bar{\alpha}(E_1, E_2, E_3) = \alpha_1(E_1)\alpha_2(E_2); \tag{4.4}$$

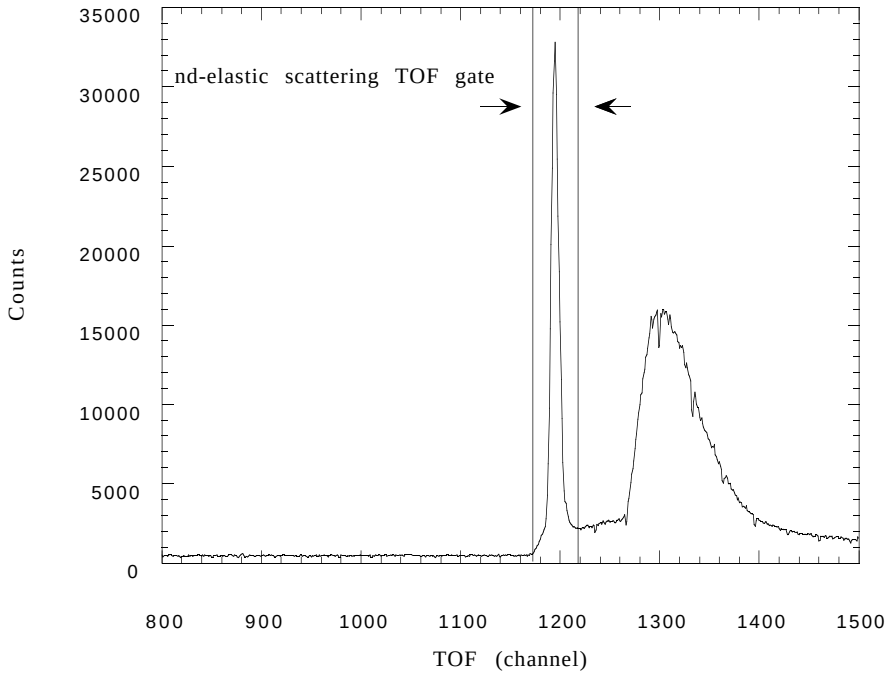


Figure 4.2: Time-of-Flight spectrum associated with detector 9 showing the gated *nd* elastic scattering peak. The resolution of the spectrum is ∼0.2 ns/channel.

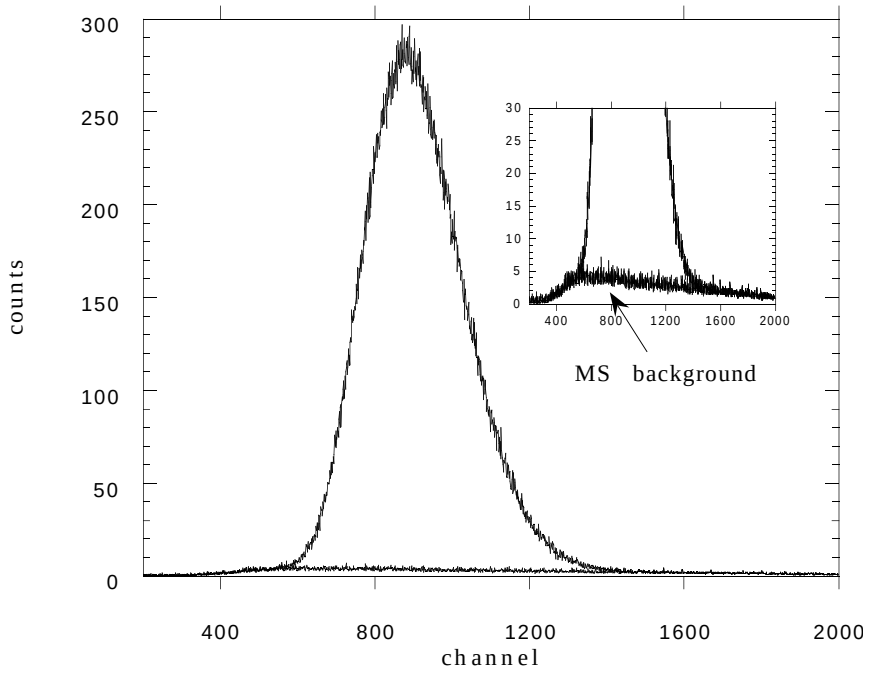


Figure 4.3: MC Center Detector pulse-height spectrum associated with the *nd* elastic scattering TOF peak of detector 9.

2. The absolute neutron detection efficiency product

$$\bar{\varepsilon}(E_1, E_2, E_3) = \varepsilon_1(E_1)\varepsilon_2(E_2); \tag{4.5}$$

3. The Gaussian proton energy distribution weight factor $\omega(E_3)$ due to the finite pulse-height resolution of the center detector; and

4. The point-geometry differential cross section $\frac{d^3\sigma_t}{d\Omega_1 d\Omega_2 dS}(E_1, E_2, E_3)$.

The energies of the breakup neutron 1, neutron 2 and the proton are $E_1$, $E_2$ and $E_3$, respectively. In the experiment, the energies of the outgoing neutrons are determined by time of flight, where it is assumed that the neutrons travel from the geometric center of the CD to the center of the neutron detectors. In order to be able to directly compare experimental and MC results it is necessary to express the MC output as a function of TOF energies ($E_1$, $E_2$, $E_3$) using the expressions

$$E_3 = E_{tot} - E_1 - E_2, \tag{4.6}$$

where $E_{tot}$ is the total kinetic energy available to the three nucleons in the outgoing channel (10.775 MeV for a $E_n = 13.0$ MeV neutron beam), and

$$E_i' = (\frac{{d_i'}^2}{{d_i}^2})E_i, \tag{4.7}$$

where $i = 1$ or 2. The center-to-center distance from target to neutron detector is $d_i'$, and $d_i$ is the actual distance traveled by the simulated neutron. For the proton we have $E_3' = E_3$.

The $nd$ breakup MC output for a simulated event is generated in the following way:

1. Points are randomly selected within the deuterated target and the pair of neutron detectors in an $nn$ FSI configuration This choice fixes the angles $\theta_1, \theta_2, \phi_{12}$, while the bombarding neutron energy $E_n$ is chosen from a distribution between 12.8 and 13.2 MeV, determining a kinematic locus in $(E_1, E_2, E_3)$ space (S-curve).

2. The theoretical cross-section libraries (see section 4.2) are used as basis for a multi-parameter linear interpolation to obtain the $nn$ FSI cross section as a function of S-curve length. The interpolation parameters used are $\theta_1, \theta_2, \phi_{12}$, $E_n$, and the breakup nucleon momenta $k_1$, $k_2$, $k_3$ (see Equation 4.10).

3. The values for $\bar{\varepsilon}(E_1, E_2, E_3)$, $\bar{\sigma}(E_1, E_2, E_3)$, $\bar{\alpha}(E_1, E_2, E_3)$ and $\omega(E_3)$ are calculated for each point on the MC event's S-curve. The individual neutron detector efficiencies $\varepsilon_1(E_1)$ and $\varepsilon_2(E_2)$ are introduced into the MC code by means of data tables.

4. The weight factors elements $k(E_1', E_2', E_3')$ are given by

$$k(E_1', E_2', E_3') = \omega(E_3)\bar{\alpha}(E_1, E_2, E_3)\bar{\varepsilon}(E_1, E_2, E_3). \tag{4.8}$$

   Likewise, the cross-section elements $s(E_1', E_2', E_3')$ are given by the product

$$s(E_1', E_2', E_3') = \bar{\sigma}(E_1, E_2, E_3)\omega(E_3)\bar{\alpha}(E_1, E_2, E_3)\bar{\varepsilon}(E_1, E_2, E_3), \tag{4.9}$$

   where $\bar{\sigma}(E_1, E_2, E_3)$ is the $nd$ breakup differential cross section for the MC event, obtained after interpolation using the cross-section libraries.

The finite-geometry theoretical $nd$ breakup differential cross sections $\frac{d^3\sigma_{ann}^{MC}}{d\Omega_1 d\Omega_2 dS}(S)$ are obtained through the following procedure:

1. The point-geometry locus $S(E_1^c, E_2^c, E_3^c)$ is calculated for the $nn$ FSI configuration in steps of $\Delta S = 0.5$ MeV (the superscript "c" denotes the ideal point-geometry locus). The locus $S$ and $\kappa$ and $\bar{\Sigma}$ elements are re-indexed in terms of the momenta

$$k_i' = \sqrt{2E_i' m}, \tag{4.10}$$

   where i=1,2,3 and the mass of the proton and the neutron are taken to be identical ($m = 939$ MeV).

2. The value of each element $k(k_1', k_2', k_3')$ and $s(k_1', k_2', k_3')$ is assigned to a point on the $S(k_1^c, k_2^c, k_3^c)$-curve where

$$K = \sqrt{\sum_{i=1,2,3} (k_i^c - k_i')^2} \tag{4.11}$$

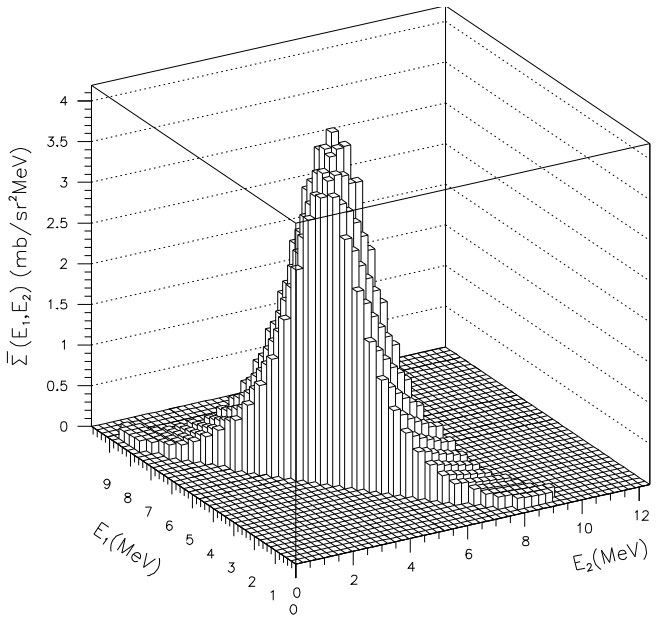


Figure 4.4: $\bar{\Sigma}(E_1', E_2', E_3')$ matrix projected onto the $E_1' - E_2'$ plane for easier viewing (nnfsr4 configuration).

is minimized [Fin87]. From these projections we obtain the simulated yields curve and the weight factor curve $\kappa(S)$: $\bar{\Sigma}(S)$

$$\bar{\Sigma}(S) = \frac{\sum_{k_i'} s(k_1', k_2', k_3')}{\sum_{k_3'} \omega(k_3')} \tag{4.12}$$

and

$$\kappa(S) = \frac{\sum_{k_i'} k(k_1', k_2', k_3')}{\sum_{k_3'} \omega(k_3')}. \tag{4.13}$$

The summations go over the indices $k_i'$ that correspond to a point $S$ on the ideal S-curve according to the criterion given by Equation 4.11.

3. Finally, the expression

$$\frac{d^3\sigma_{a_{nn}}^{MC}}{d\Omega_1 d\Omega_2 dS}(S) = \frac{\bar{\Sigma}(S)}{\kappa(S)} \tag{4.14}$$

yields the finite-geometry theoretical *nd* breakup differential cross section for discrete values of $S$ along the ideal *nn* FSI kinematic locus $S(E_1^c, E_2^c, E_3^c)$ (see Figure 4.5). The subscript $a_{nn}$ indicates the neutron-neutron scattering length corresponding to the library used in the cross-section calculation. Thus, the point-geometry theoretical and experimental *nn* FSI cross-section curves can be compared directly.

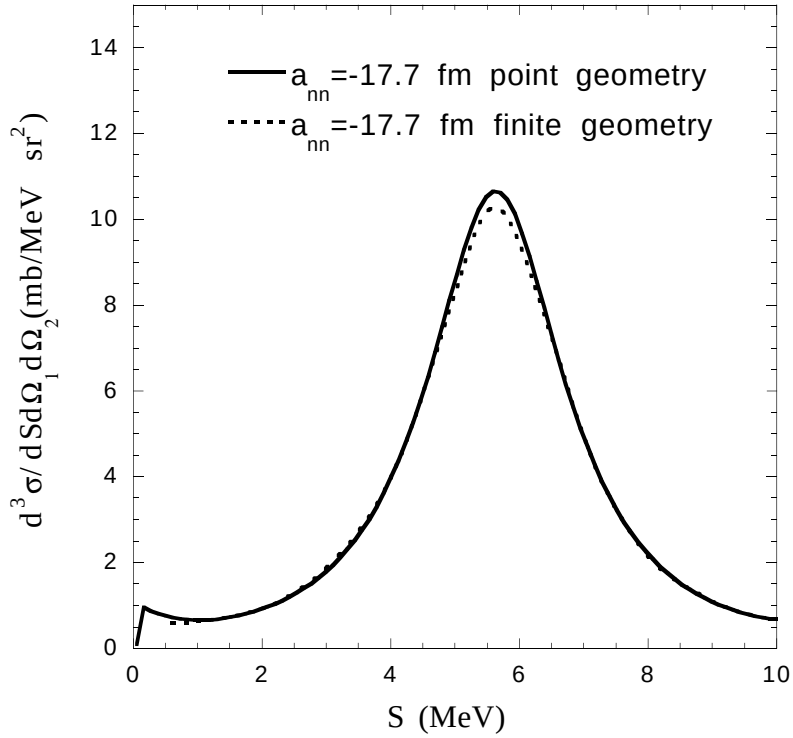


Figure 4.5: Comparison of finite and point-geometry *nd* breakup differential cross sections for the nnfsr3 configuration.

# Chapter 5

# Data Analysis

The experimental data were acquired during ten runs lasting one to two weeks each. Because of changing experimental conditions, each run was individually analyzed off-line. The events accumulated are divided into double and triple events. Double events consist of the correlated "firing" of the center detector (CD) and any neutron detector. Triple events consist of the correlated "firing" of the CD and any pair of neutron detectors belonging to a $nn$ FSI configuration.

Data were partially sorted on-line in order to monitor essential experimental variables such as the neutron and center detector pulse-heights (PH), time of flight (TOF) for double and triple events and pulse-shape discrimination (PSD) for all detectors. The on-line sorting was kept to a minimum in order to reduce the dead time of the data acquisition system, which was mostly due to the computer. The IUCF XSYS code was used for data acquisition because of its ability to read and manipulate data only from those channels that had a "hit" in the time-to-digital converter (TDC), saving processing time, disk and tape space.

Two-dimensional plots of yields in $E_1$ versus $E_2$ space were created on-line to insure that $nn$ FSI events were indeed occurring in the vicinity of the ideal loci. These distributions of $nn$ FSI yields became evident for all four configurations only after about a day of data

| r (run index) | start date | end date | sub-runs |
|---|---|---|---|
| 1 | 6 June 94 | 16 June 94 | 108 |
| 2 | 12 August 94 | 24 August 94 | 284 |
| 3 | 21 October 94 | 3 November 94 | 353 |
| 4 | 22 January 95 | 5 February 95 | 365 |
| 5 | 28 February 95 | 8 March 95 | 239 |
| 6 | 27 March 95 | 3 April 95 | 215 |
| 7 | 10 May 95 | 19 May 95 | 327 |
| 8 | 2 July 95 | 17 July 95 | 494 |
| 9 | 23 August 95 | 31 August 95 | 250 |
| 10 | 14 September 95 | 22 September 95 | 269 |
| | | Total sub-runs | 2904 |
| | | Total hours | 2178 |

Table 5.1: Summary of runs of the $a_{nn}$ experiment

accumulation.

The data sorting was divided into two parts:

1. Double events were sorted to find the yields from *nd* elastic scattering, and to extract the luminosity $\beta_r$ for a particular run. In this way the *nd* breakup yields from each run can be normalized for later determination of the *nn* FSI cross section.

2. Triple events were sorted to find the *nd* breakup yields corresponding to each *nn* FSI configuration, and to obtain absolute cross sections from these yields.

## 5.1 Luminosity Determination

The calculation of the absolute *nn* FSI cross section hinges on knowing the luminosity per unit charge of beam deposited on the deuterium gas cell, defined as

$$\beta_r = \frac{N_n^r N_d}{[BCI]_r}, \tag{5.1}$$

where $N_n^r$ is the number of neutrons incident on the CD during a particular run $r$ and $N_d$ is the number of deuterium atoms per cm$^3$ of the CD.

By determining the net yields from $nd$ elastic scattering events for various neutron scattering angles it is possible to determine $\beta_r$ from the expression

$$\Upsilon_{el}^r(\theta) = \frac{d\sigma_{lab}}{d\Omega}(\theta)\alpha(E_{el})\epsilon(E_{el})\beta_r[BCI]_r\Omega, \tag{5.2}$$

where $\alpha(E_{el})$ is the transmission probability of the elastically-scattered neutrons with energy $E_{el}$, taking into account the building materials of the deuterated target and including air attenuation. The absolute detection efficiency of the neutron detector for scattered neutrons with energy $E_{el}$ is $\epsilon(E_{el})$. The solid angle subtended by the neutron detector is $\Omega$. The $nd$ elastic scattering differential cross sections in the lab frame ($\frac{d\sigma_{lab}}{d\Omega}(\theta)$) were calculated for us by the Bochum-Cracow group. The methods and accuracy of the $nd$ elastic scattering cross-section calculations are discussed in [Wit89]. The integrated current measured during run $r$ is $[BCI]_r$. The $nd$ elastic scattering yields $\Upsilon_{el}^r(\theta)$ are determined from the center detector pulse-height (CDPH) corresponding to those neutron events that fall within the gate assigned to the TOF $nd$ elastic scattering peak. These yields are determined for several detectors (typically three) at different angles for each run $r$.

### 5.1.1 Accidental $nd$ Elastic Scattering Events

There is a possibility that a stop TDC signal from a neutron detector will be accidentally in coincidence with a trigger signal starting the TDC. The net effect is that events with shorter TOFs can appear in the spectrum at longer TOFs. These types of events are referred to as accidentals, and since they are random in time, they produce a flat background in TOF. It is necessary to correct for accidentals in order to extract the net $nd$ elastic scattering yields $\Upsilon_{el}^r(\theta)$.

The contribution of accidentals can be estimated by setting a gate in the TOF spectrum before the $\gamma$-ray peak, where no truly correlated double events can exist. This

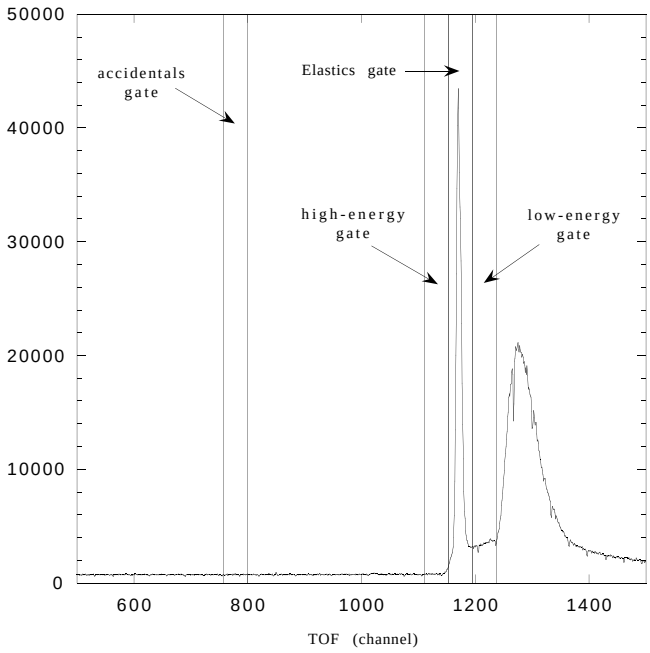


Figure 5.1: Doubles TOF spectrum for detector 8 after applying pulse-shape discrimination. The enhancement to the right of the low-energy gate is due to neutrons produced by the breakup of deuterons in the gas cell.

gate has the same width as the gate used for the *nd* elastic scattering events (see Figure 5.1). The accidentals are then sorted in the same way as the events within the elastic scattering events' TOF gate, generating an accidental CDPH spectrum.

### 5.1.2 Sample-Correlated Background

The $^{2}$H(d,n)$^{3}$He reaction that creates a beam of 13.0 MeV neutrons also creates a continuum of lower-energy neutrons via breakup of deuterons in the foil, gas or the beam stop of the deuterium gas cell. These so-called gas-cell breakup neutrons can scatter successively on carbon and deuterium or vice-versa in the center detector (CD), and arrive at a neutron detector with the same TOF as a 13.0 MeV neutron that scattered only once on

a deuteron in the CD. These scattered gas-cell breakup neutrons form a sample-correlated background beneath the *nd* elastic scattering TOF peak. In addition, neutrons produced by *nd* breakup reactions in the center detector may also undergo scattering on carbon and arrive with a TOF indistinguishable from that of the *nd* elastic scattering neutrons of interest.

The sample-correlated background was estimated by combining information from Monte-Carlo (MC) simulations and experimental CDPH events from the two gates adjacent to the elastic scattering peak gate in TOF (low and high-energy gates are shown in Figure 5.1). The CDPH spectra were generated for events falling within these gates and stored in separate data areas and their accidental background was subtracted.

The experimental *nd* elastic scattering TOF peak was Monte-Carlo simulated assuming only single-scattering *nd* elastic processes (see Section 4.3.1). The input parameters of the simulation were adjusted to reproduce the centroid position and full-width half-maximum (FWHM) of the experimental *nd* elastic scattering TOF peak. We also matched the MC CDPH spectrum associated to *nd* elastic scattering events (after accidental subtraction) to the shape and area of the experimental CDPH spectrum (with accidental events already subtracted). This was accomplished by calculating an exponential background under the experimental CDPH deuteron-recoil peak, matching the flat region to the left of the peak and the high pulse-height tail end to the right of the peak. The calculated background was subtracted from the experimental CDPH and the input parameters of the MC simulation were modified to reproduce the net CDPH spectrum. The MC *nd* elastic scattering simulations for multiple-scattering (MS) events could then be properly normalized and subtracted from the CDPH experimental spectra for events falling in the *nd* elastic scattering, low and high-energy TOF gates.

The MS contributions were calculated for CDPH spectra for events falling in the low-energy, elastic scattering, and high-energy TOF gates. These simulated MS contributions were normalized and subtracted from their corresponding experimental CDPH spectra (with

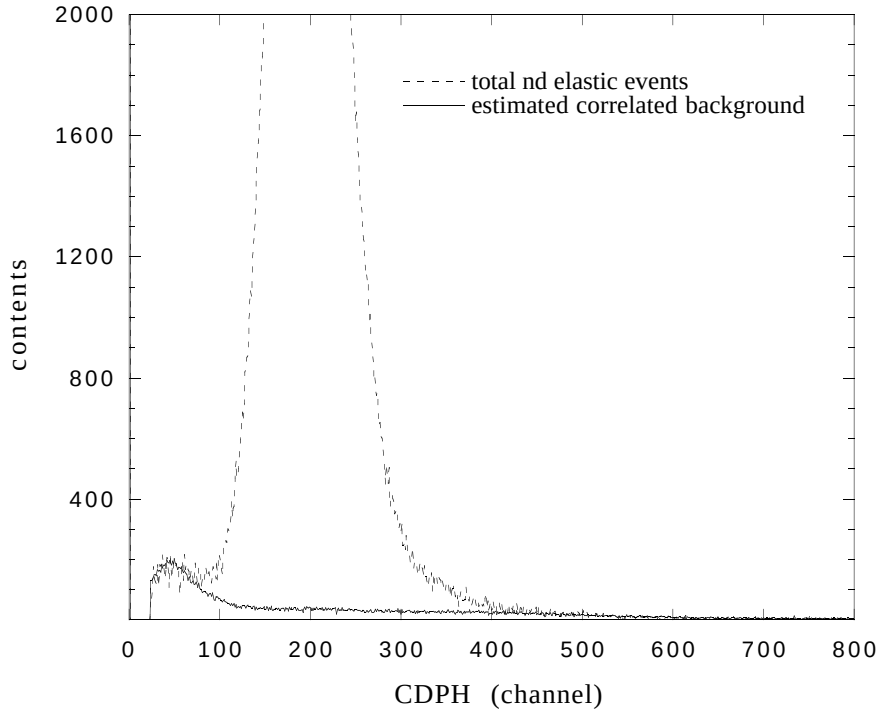


Figure 5.2: Elastic scattering events CDPH spectrum for detector 8 after subtraction of accidentals and calculated MS background. The solid curve is the sample-correlated background estimated from averaging the net CDPH spectra for events from the low-energy and high-energy TOF gates corrected for multiple scattering, accidentals. The resulting spectrum is normalized to match the high pulse-height end and beginning of the elastics' CDPH enhancement.

accidental events already subtracted). The resulting CDPH spectra belonging to the low-energy and high-energy TOF gates were averaged channel-by-channel and normalized to fit the tail-end and the low PH part of the enhancement of the CDPH spectrum derived from the events in the elastic scattering TOF gate (see Figure 5.2). An exponential fit was made of the sample-correlated background and subtracted from the elastics' CDPH spectrum. The resulting net CDPH spectrum was integrated between the channels where the calculated exponential background meets the experimental CDPH spectrum in the low

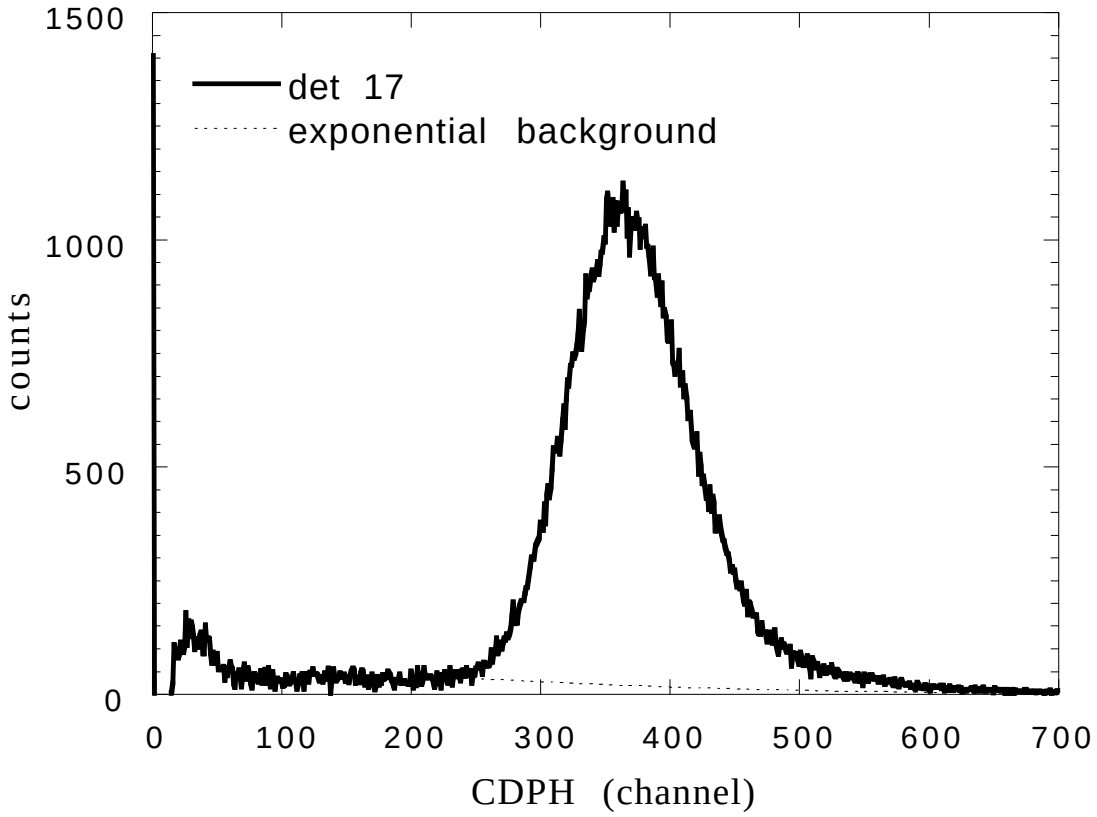


Figure 5.3: Elastic scattering events CDPH spectrum for detector 17.

pulse-height end, and up to the end of the experimental CDPH spectrum. Thus we obtained the net elastic scattering yields $\Upsilon^r_{el}(\theta)$ for a particular $nd$ elastic scattering angle and run (see Figure 5.3). The $nd$ elastic scattering yields were determined for at least three neutron detectors (typically detectors 8, 17 and 18) for a given run to check for systematic errors in the extraction of $\Upsilon^r_{el}(\theta)$. Table 5.2 shows the luminosity values for each run. The standard deviation of the mean reflects the error associated with the technique of correlated-background subtraction.

| run | $\beta_r(\frac{yields}{kBCI})$ | standard deviation | standard deviation of the mean | % standard deviation of the mean |
|---|---|---|---|---|
| Jan-95 | 1538. | 24. | 14. | 0.9 |
| Feb-95 | 1524. | 45. | 26. | 1.7 |
| Mar-95 | 1894. | 37. | 21. | 1.1 |
| May-95 | 1764. | 14. | 8. | 0.5 |
| Jul-95 | 1696. | 69. | 40. | 2.3 |
| Aug-95 | 1577. | 71. | 41 | 2.6 |
| Sep-95 | 1632. | 60. | 35. | 2.1 |

Table 5.2: Luminosity $\beta_r$ extracted for each run.

## 5.2 Dead-Time and ADC-Loss Corrections

Dead-time correction (DTC) factors were determined using the LED and electronic pulsers (see Section 2.4.3). The electronic signals generated by each pulser driver were sent to scalers and counted by the computer.

Most of the dead time of the system was incurred by the computer in processing the data and vetoing further incoming trigger signals until it was ready to register the next event. This was tested by independent LED and electronic pulsers.

An LED pulser was coupled to the center detector and neutron detectors 12 and 20, correlating events for every pulse and forcing them to go through the triple-coincidence part of the trigger circuit (see Section 2.4.3). We made sure the LED pulses always satisfied the $\frac{1}{3}\times$Cs PH threshold and PSD requirements. Thus, pulser events were lost mostly to dead time (some were also lost to ADC false-peak triggering, as explained at the end of this section).

Every LED pulser event was tagged in the computer by sending the pulser driver's electronic signal to a TDC channel. The pulser events were then selected using the tag and accumulated in separate PH, PSD and TOF spectra. To obtain the DTC we divided the number of LED pulser driver hits counted in the scaler by the number of LED pulser events

registered by the computer.

An electronic pulser sent signals directly to the TDC channels used for TOF and PSD, to the trigger circuit that provided start signals, and to a scaler. A TDC channel was used for tagging. The pulser signal was also sent into the neutron detector preamplifiers to allow PH analysis. The DTC was obtained just as in the case of the LED pulser. Both electronic and LED pulsers gave DTCs which agreed within $\pm 0.005$. For most detectors the DTCs were $\sim$1.06. The triple-event DTC for a pair of detectors in an $nn$ FSI configuration is given by whichever detector in the pair has the largest doubles DTC.

Sometimes an ADC would trigger on a false peak signal causing a zero pulse-height count to be recorded instead of the true linear signal. This type of misfire is random and accumulates in the zero channel of the PH spectrum. These ADC losses were measured by taking the ratio of zero-channel counts to the total number of counts in the PH spectrum for each detector. The ADC losses were $\sim$2%, and depended on the ADC module and to a lesser extent on the channel used within an ADC. An LED pulser was used to confirm the ADC losses calculated from the PH spectra.

## 5.3 Center Detector Light-Output Functions

Kinematically overdetermined measurements are possible through the detection of signals from neutrons and from protons from $nd$ breakup processes (See Section 2.3.1). The center detector pulse-height spectra associated with $nd$ elastic scattering events are used to establish a deuteron light-output function $L_d(E)$ by making a plot of the channel position of the centroid of the CDPH distribution versus the recoil energy of the corresponding deuteron. We collected data for recoil deuteron energy ranges of $1.0 \leq E \leq 9.0$ MeV (low gain) and $0.4 \leq E \leq 3.0$ MeV (high gain). Deuteron light-output functions were obtained independently for high and low CDPH gains. Because experimental conditions changed somewhat from one run to the next (e.g., changes in the gain of the CD phototube) we obtained $L_d(E)$ for every run (see Figure 5.4). The light-output function for protons ($L_p(E)$)

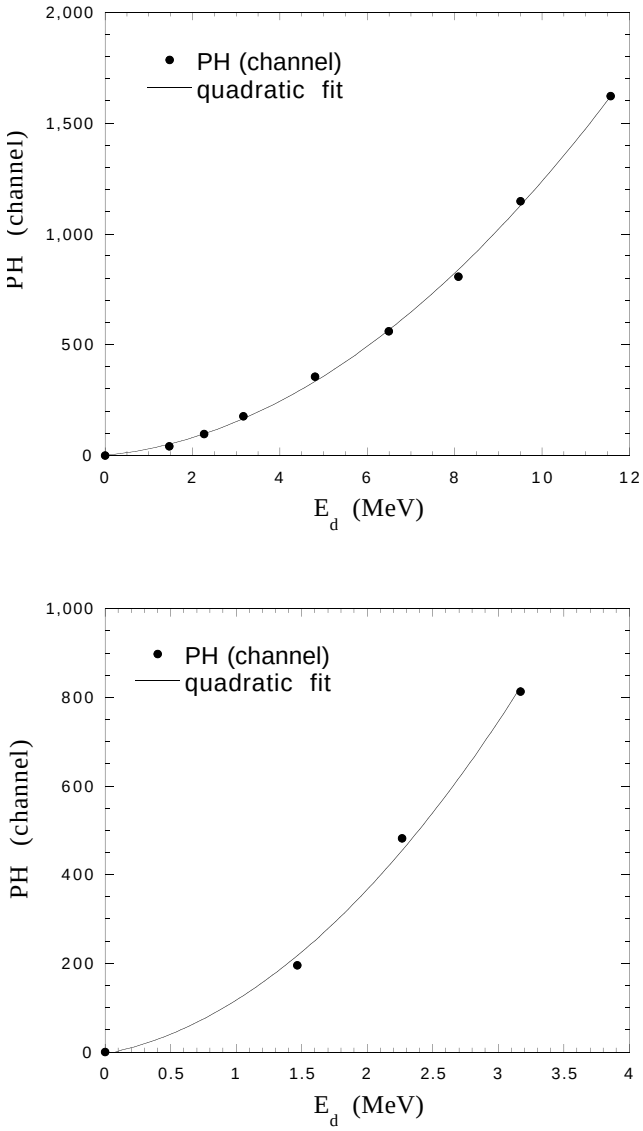


Figure 5.4: Low-gain $L_d(E)$ for the Feb95 run (top). High-gain $L_d(E)$ for the Feb95 run (bottom). Quadratic functions were used to fit the data points for both gains.

was determined using the expression [Tor86]

$$L_p(E) = \frac{1}{2} L_d(2E), \tag{5.3}$$

allowing us to find the proton energy associated with the neutrons detected in $nn$ FSI events.

## 5.4 Breakup Event Sorting

Breakup events were identified using a series of PH, PSD and kinematic requirements on the experimental data stored on tape. These software cuts reduced the breakup data to be stored on summary tapes by a factor of 10000. Only events belonging to the four $nn$ FSI configurations studied were written onto summary tapes. Each event had to exceed a pulse-height threshold of $\frac{1}{3}\times$Cs, satisfy PSD requirements identifying it as a neutron event, have a proton energy greater than 0.4 MeV and fall within a total energy gate of 10.775$\pm$4.0 MeV. The energies of both neutrons in an event were calculated from TOF, and the proton energy was established by means of the light-output for protons $L_p(E)$.

Triple events fulfilling the kinematic software cuts consisted of the following parameters: Configuration number, event-type tag (see Table 5.3), TOFs of both of neutrons, low and high-gain CDPH, neutron and proton energies (calculated from TOF and CDPH, respectively). All events written onto summary tapes were converted to ntuples for faster analysis using the Physics Analysis Workstation software package. The TOFs for a detector may fall within either of two possible gates: Accidental (A) or true+accidental (T+A) (see Figure 5.5). The accidental gate has one-half the width of the true+accidental gate. Accidental events do not have a real TOF (and energy) associated with them, but since they are randomly spread throughout the TOF spectrum, we can assign them a TOF in the following way: If an event has a TOF that falls within the T+A gate, and another TOF falling on channel $c$ within the accidental gate, then that event is assigned a TOF channel

$$c' = (c - c_a) + c_t, \tag{5.4}$$

| tag | detector 1 event type | detector 2 event type |
|---|---|---|
| 1 | A | A |
| 2 | T+A | A |
| 3 | A | T+A |
| 4 | T+A | T+A |
| 5 | A' | A' |
| 6 | T+A | A' |
| 7 | A' | T+A |
| 8 | A' | A |
| 9 | A | A' |

Table 5.3: Tag assignment to types of triple events. The primes refer to additional accidental events generated because of size difference between T+A and accidental gates.

where $c_a$ is the first channel of the accidental gate and $c_t$ is the first channel of the true+accidental gate. Because the accidental gate is only one-half the width of the T+A gate, an additional event is generated with TOF channel

$$c' = (c - c_a) + c_t + \frac{\Delta C_{t+a}}{2}, \tag{5.5}$$

where $\Delta C_{t+a}$ is the width of the T+A gate. If both TOFs in an event fall within the accidental gates, then four events are generated with TOFs given by the procedure described above.

## 5.5 Breakup Cross-Section Determination

### 5.5.1 Event Projection onto the Ideal-Locus S-Curve

Events that satisfied all kinematic software cuts for a particular $nn$ FSI configuration were indexed according to the momenta of the neutrons and the proton. Accidental events were treated in the same way, but separated from true + accidental events for later subtraction. The ideal point-geometry locus for a given $nn$ FSI configuration was discretized

in steps of 0.5 MeV, and each point on the S-curve had its associated energies ($E_1^c$, $E_2^c$, $E_3^c$) converted into momenta ($k_1^c$, $k_2^c$, $k_3^c$). To obtain yields as a function of S-curve length we projected the experimental points in momentum space ($k_1^{exp}$,$k_2^{exp}$,$k_3^{exp}$) onto the ideal kinematic locus points that are nearest to them by minimizing the distance in momentum space [Fin87]

$$K_{min} = \sqrt{\sum_{i=1,2,3} (k_i^c - k_i^{exp})^2}. \tag{5.6}$$

### 5.5.2 Cross-Talk Background Subtraction

A neutron from the beam can scatter off the CD, causing a recoil deuteron to produce a detectable signal. The same neutron can then proceed to interact with the ring detector of an *nn* FSI configuration via multiple-scattering (single scattering off a proton or carbon will not produce a signal above the PH threshold of $\frac{1}{3}\times$Cs) and then interact with the back detector of the same *nn* FSI configuration. This type of event is kinematically indistinguishable from a true *nd* breakup event. Usually the energy deposited in the CD is below our detection threshold, but because of CDPH pile-up due to $\gamma$ rays and the continuum of neutrons from the deuterium gas cell, the pulse height may exceed our CD threshold and the event is detected.

Another type of cross-talk event comes from true *nd* breakup processes where the proton is detected in the CD, one of the neutrons leaves in an unspecified direction and the second neutron is detected via multiple-scattering in a ring detector and then is detected by the associated Bicron detector. Due to their large kinematic range, the cross-talk events are smoothly distributed in $(E_1, E_2, E_3)$ space.

In order to estimate the contribution of the cross talk to the raw *nn* FSI yields, every event that was projected onto its closest point on the ideal S-curve was also assigned to $E_h = E_1 + E_2$ in a new *diagonal projection histogram* (DPH) binned in steps of 0.1 MeV. Every point on the ideal S-curve for every *nn* FSI configuration had a corresponding DPH. This is equivalent to projecting events corresponding to a point on the ideal S-curve onto the

diagonal $E_1 = E_2$. The diagonal projections consisted of a prominent $nn$ FSI enhancement on a smooth background of cross-talk events (see Figure 5.6). The experimental DPHs for each run were normalized and summed over according to the expression

$$\bar{Y}_{raw}(E_h, S) = \frac{1}{R} \sum_r \frac{Y_r(E_h, S) k_r^{dtc}}{\beta_r [BCI]_r}, \tag{5.7}$$

where $Y_r(E_h, S)$ are the raw yields projected onto the $E_1 = E_2$ diagonal for a particular run, $\beta_r$ is the luminosity/BCI (see Section 5.1), $[BCI]_r$ is the integrated current measured during run $r$, $k_r^{dtc}$ is the dead-time correction factor for $nn$ FSI events and $R$ is the number of runs considered. The $nd$ breakup Monte-Carlo program generated DPH distributions. The experimental diagonal projections $\bar{Y}_{raw}(E_h, S)$ were fitted by a Monte-Carlo simulated DPH curves (multiplied by a normalization factor) plus a fifth-degree polynomial to model the background underneath and around the $nn$ FSI peak. The polynomial curve was then subtracted from the experimental DPH and the remaining distribution was summed over using the limits provided by the Monte-Carlo simulation of the DPH, thus obtaining the net average yield as a function of S-curve length $\bar{Y}_{net}(S)$ for each $nn$ FSI configuration. The differential $nd$ breakup cross section as a function of S-curve length was determined using the expression

$$\frac{d^3\sigma(S)}{d\Omega_1 d\Omega_2 dS} = \frac{\bar{Y}_{net}(S)}{\kappa(S)\Omega_1\Omega_2\Delta S}, \tag{5.8}$$

where $\Delta S = 0.5$ MeV, $\Omega_i$ are the solid angles subtended by the detectors used in the $nn$ FSI configuration, and $\kappa(S)$ are the Monte-Carlo-calculated attenuation and efficiency factors (see Section4.3.2).

### 5.5.3 Breakup Cross-Section Uncertainties

The systematic errors associated to the experimental $nd$ breakup cross sections originate from several sources:

1. The error in the solid angles $\Omega_1$ and $\Omega_2$ (0.67%, 0.4%) are due in part to the uncertainty in the distance of the neutron detectors from the CD ($\pm$0.5 cm), and also from the

uncertainty in the radii of the ring detectors. These solid angle errors are assumed to have a normal distribution.

2. The systematic uncertainty in the neutron detection efficiency of each detector is partly due to the normalization to the $^2$H(d,n)$^3$He reaction cross section [Dro78] (see Section 6.3). This normalization uncertainty ($\pm 1.5\%$) has the same sign and magnitude for all detectors. In addition, there is some uncertainty $\Delta\epsilon^R$ in the efficiency due to errors in distance measurement, deuterium pressure in the gas cell, beam heating effects, etc. The latter error ($\pm 1.0\%$) is assumed to have a normal distribution.

3. The attenuation factors $\alpha_i$ have a normalization uncertainty of $\pm 1.5\%$.

4. The systematic error in $\beta_r$ is partly due to the $nd$ elastic scattering cross-section uncertainty ($\pm 1.5\%$). The efficiency and attenuation errors in $\beta_r$ are taken to have the same sign and magnitude as in the $nd$ breakup case. The uncertainty of the solid angle $\Omega$ is $\pm 0.67\%$.

The systematic error of the $nd$ breakup cross section follows from Equations 5.8 and 5.2, where the normalization errors from all sources are added linearly. When calculating the final systematic error, cancellations occur between some uncertainties due to their equal sign, proportion and presence in the numerator and denominator of Equation 5.8.

$$(\frac{\Delta\sigma}{\sigma})^s = (\frac{\Delta\alpha_1}{\alpha_1}) + (\frac{\Delta\alpha_2}{\alpha_2}) - (\frac{\Delta\alpha}{\alpha}) + (\frac{\Delta\epsilon_1^s}{\epsilon_1}) + (\frac{\Delta\epsilon_2^s}{\epsilon_2}) - (\frac{\Delta\epsilon^s}{\epsilon}) + (\frac{\Delta\sigma_{el}}{\sigma_{el}}). \tag{5.9}$$

The systematic errors which are assumed to obey a normal (random) distribution are added according to the expression

$$(\frac{\Delta\sigma}{\sigma})^R = \sqrt{(\frac{\Delta\epsilon_1^R}{\epsilon_1})^2 + (\frac{\Delta\epsilon_2^R}{\epsilon_2})^2 + (\frac{\Delta\epsilon^R}{\epsilon})^2 + (\frac{\Delta\Omega_1}{\Omega_1})^2 + (\frac{\Delta\Omega_2}{\Omega_2})^2 + (\frac{\Delta\Omega}{\Omega})^2}. \tag{5.10}$$

Finally, the error components $(\frac{\Delta\sigma}{\sigma})^R$ and $(\frac{\Delta\sigma}{\sigma})^s$ are added in quadrature. The resulting total uncertainty due to systematic errors is $\pm 5\%$. The statistical error was calculated for each point on the ideal S-curve and is $\lesssim 5\%$ for all cross-section maxima.

## 5.6 Extraction of $a_{nn}$

### 5.6.1 Extraction from the Absolute $nn$ FSI Cross Section

Finite-geometry $nn$ FSI cross section curves ($\frac{d^3\sigma^{MC}_{a_{nn}}(S)}{d\Omega_1 d\Omega_2 dS}$) were generated by Monte-Carlo simulations for all configurations of interest and for values of $a_{nn}$ ranging from $-17.0$ fm to $-20.0$ fm. The expression

$$\chi^2(a_{nn}) = \sum_S \frac{(\frac{d^3\sigma^{MC}_{a_{nn}}(S)}{d\Omega_1 d\Omega_2 dS} - \frac{d^3\sigma(S)}{d\Omega_1 d\Omega_2 dS})^2}{(\Delta\frac{d^3\sigma(S)}{d\Omega_1 d\Omega_2 dS})^2} \tag{5.11}$$

gives $\chi^2$ as a function of $a_{nn}$, where $\Delta\frac{d^3\sigma(S)}{d\Omega_1 d\Omega_2 dS}$ is the statistical error associated with the experimental cross section. A plot was made of $\chi^2$ versus $a_{nn}$ for each $nn$ FSI configuration. The plot was then fitted by a quadratic polynomial, whose minimum $\chi^2_{min}$ gives the value for $a_{nn}$ (See Figure 5.7). The statistical error in the $a_{nn}$ determination is given by

$$\Delta a^{stat}_{nn} = |a_{nn}(\chi^2_{min}) - a_{nn}(\chi^2_{min} + 1)|. \tag{5.12}$$

To estimate the effect of the cross section's systematic uncertainty on $a_{nn}$, we multiplied the experimental cross-sections by 1.05 and found the $a^{max}_{nn}$ value corresponding to the new minimum in $\chi^2$ using Equation 5.11 and as described above. The same procedure was used to obtain $a^{min}_{nn}$ for experimental cross sections normalized by 0.95. For each $nn$ FSI configuration we obtained a systematic error for $a_{nn}$ given by

$$\Delta a^{sys}_{nn} = \frac{1}{2}(|a^{min}_{nn} - a^{max}_{nn}|). \tag{5.13}$$

### 5.6.2 Extraction from the Shape of the $nn$ FSI Cross Section

Attempts have been made in the past to extract $a_{nn}$ solely from the shape of the cross section using Watson-Migdal [One78] and Yamaguchi Form Factor formalisms [Zei74, vW79]. A similar approach was used in our case, although we employed rigorous Faddeev calculations using the Bonn-B OBEPQ potential instead of the previous more approximate methods. Neutron-Neutron scattering lengths we extracted from the cross-section shapes

are denoted by the *shape* superscript to tell them apart from the $a_{nn}$ values we extracted from absolute $nn$ FSI cross sections, as described in Section 5.6.1.

For each $nn$ FSI configuration analyzed the experimental cross section was multiplied by a normalization factor $K_n$ used as a free parameter to find the minimum $\chi^2$ from the expression

$$\chi^2(a_{nn}, K_n) = \sum_S \frac{(\frac{d^3\sigma^{MC}_{a_{nn}}(S)}{d\Omega_1 d\Omega_2 dS} - K_n \frac{d^3\sigma(S)}{d\Omega_1 d\Omega_2 dS})^2}{(\Delta \frac{d^3\sigma(S)}{d\Omega_1 d\Omega_2 dS})^2}, \tag{5.14}$$

where the variable definitions are the same ones used in Equation 5.11. For every $nn$ FSI configuration we made a plot of $\chi^2(a_{nn})$ versus $a_{nn}$, which was fitted by a quadratic function whose minimum corresponds to the $a_{nn}^{shape}$ (see Figure 5.8). The associated error is given by

$$\Delta a_{nn}^{shape} = |a_{nn}^{shape}(\chi^2_{min}) - a_{nn}^{shape}(\chi^2_{min} + 1)|. \tag{5.15}$$

This approach was used for all $nn$ FSI configurations except $\theta_{nn} = 43^\circ$, where too few experimental cross-section points were available for a meaningful fit.

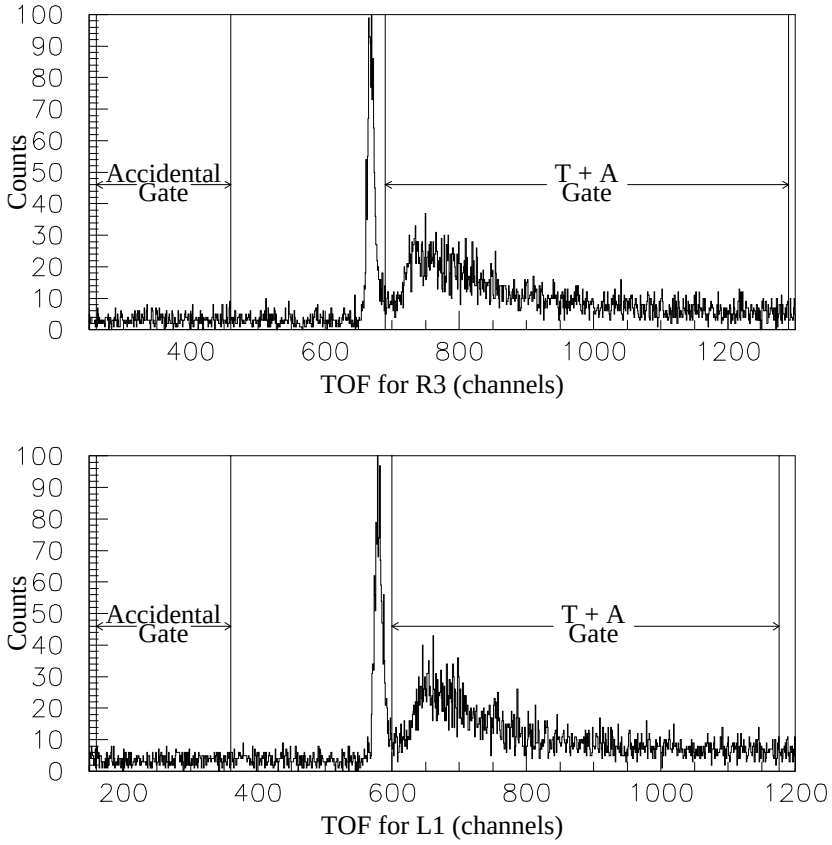


Figure 5.5: Typical triples TOF spectra showing accidental and T (true)+A (accidental) gates.

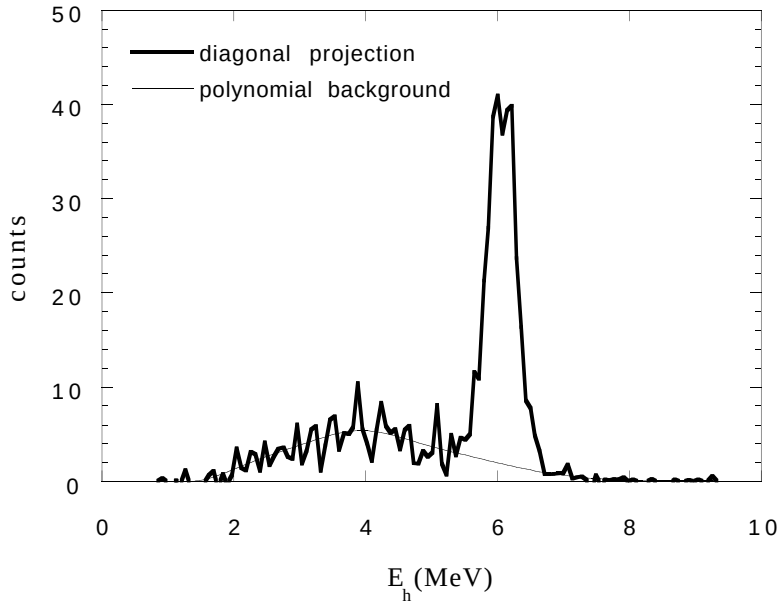


Figure 5.6: Experimental diagonal projection for $nn$ FSI configuration $\theta_{nn} = 20.5°$, $S = 6.5$ MeV. The cross-talk background under the $nn$ FSI peak is fitted by a fifth-degree polynomial.

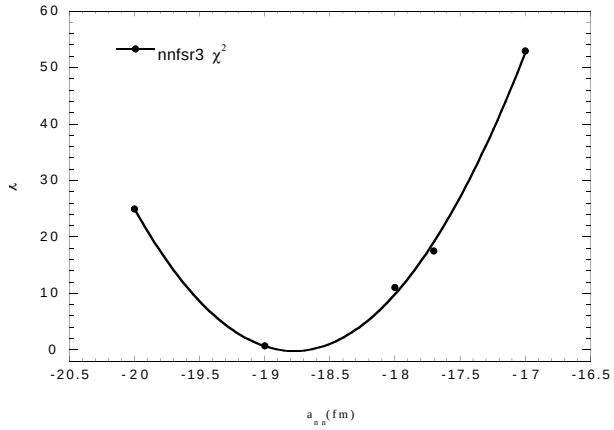


Figure 5.7: $\chi^2$ determination of $a_{nn}$ from the absolute cross section for $\theta_{nn} = 28°$.

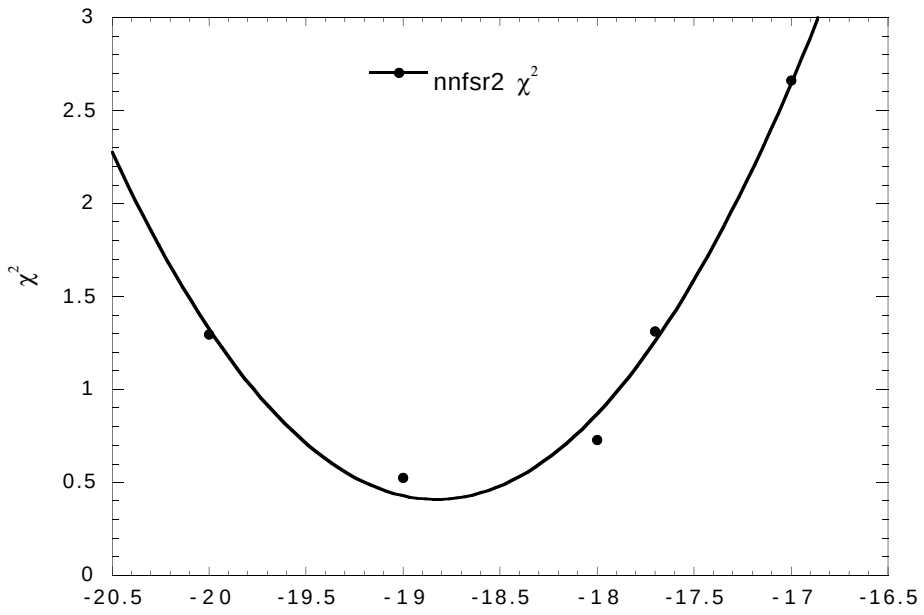


Figure 5.8: $\chi^2$ versus $a_{nn}$ from the cross-section shape for $\theta_{nn} = 35.5°$ (configuration nnfsr2).

# Chapter 6

# Neutron Detector Efficiencies

## 6.1 Introduction

Because neutrons have no charge it is necessary to rely on indirect methods to detect them. Plastic and liquid scintillators are traditionally used to detect neutrons in the low ($\sim$ 20 keV) to very high (GeV) energy range. Neutrons interact with organic scintillator materials through several mechanisms depending on the kinetic energy of the neutron projectile. For neutron energies below 20 MeV, the neutron may interact with scintillators in the following ways:

1. single and multiple elastic scattering on hydrogen nuclei,
2. single and multiple elastic and inelastic scattering on carbon,
3. breakup of excited carbon into $^{8}$Be ($\tau_{\frac{1}{2}} = 0.07$ fs) and an $\alpha$ particle, and
4. breakup of excited carbon into three $\alpha$ particles.

The charged particles resulting from these processes transfer at least part of their kinetic energy to the organic liquid scintillator molecules, which upon de-excitation emit photons in the ultraviolet with an intensity proportional to the charged particles' kinetic energy. The characteristic time periods of light emission are on the order of nanoseconds [Leo94]. For

a typical neutron detector the scintillator material is optically coupled to a photocathode. The resulting photon-induced electron current is amplified by the dynode chain of a photomultiplier tube. The pulse height (PH) of the output signal is proportional to the intensity of the light emitted and therefore proportional to the kinetic energy of the charged particles produced by the interaction of the incoming neutron with the organic liquid scintillator.

The probability of detecting a neutron depends on the following factors [Cub89]:

1. the neutron energy,
2. the detection threshold bias or lower pulse-height (PH) cutoff,
3. the volume and shape of the scintillator material, which determines the probability of occurrence and detection of multiple scattering events,
4. the chemical composition of the scintillator material,
5. the physical setup of the detector resulting in inscattering of neutrons from housing and structural materials into the scintillator volume, and
6. the direction of the incoming neutron flux with respect to the detector orientation.

## 6.2 Measurements at PTB

### 6.2.1 Experimental Setup

Three TUNL detectors were studied at PTB: Detector 8 (ring type, R1), detector 9 (bicron type, B2) and detector 1 (transmission type, T1). These detectors were then used as references for efficiency measurements of detectors of similar type at TUNL (see Section 2.3). The calibrations were performed at the PTB cyclotron accelerator fast neutron facility [Bre80] in a manner similar to that described in the PTB report by Tichy *et al.* [Tic92]. The detectors' PH characteristics were incorporated in Monte-Carlo (MC)

fortran programs (NRESP7 and NEFF7 [Die82b]) that reproduce the PH response and absolute detection efficiency of organic scintillator detectors.

Neutron beams were produced by bombarding a deuterium gas cell with deuteron beams at six different energies to produce prominent 0° mono-energetic neutron fluxes from the $^2$H(d,n)$^3$He reaction at $E_n$ = 8, 9, 10, 11, 12 and 14 MeV, in addition to a significant continuum of low-energy "breakup" neutrons. The background of neutrons generated in the deuterium gas cell due to interactions of the deuteron beam with the gas cell backing was estimated by taking measurements with an empty deuterium gas cell ("gas out" runs). The neutron production yield from the $^2$H(d,n)$^3$He reaction was monitored at all times by an NE213 liquid scintillator detector placed 60.4° from the direction of the outgoing neutron beam at 0°. This "monitor yield" was later used for relative fluence normalization among the detectors studied. The neutron beam at 0° was collimated to minimize the effect of neutrons scattered from air into the detectors. All detectors were placed successively at 0° and ∼12 m from the deuterium gas cell. An already fully characterized reference detector D1 was also irradiated. Detector D1 was used for fluence comparisons with the TUNL detectors.

### 6.2.2 Proton Light-Output Function Determination

The MC code NRESP7 models the PH response for a scintillator detector irradiated by fast neutrons with energies between 0.2 and 20 MeV. Scattering effects from aluminum housing and lucite light pipes are included by using comprehensive sets of cross sections and accounting for neutron transport throughout the different materials that compose the detector assembly. The NRESP7 code models cylindrically-symmetric bicron-type detectors. Modifications to the program were necessary to account for the special geometry of the ring and transmission detectors. These new programs are referred to as NRESPR1 and NRESPT1.

To model the response of a neutron detector realistically the following aspects must

be considered [Die82b]:

1. the scintillation detector geometrical design,
2. the neutron source specifications (incoming neutron mean energy, energy distribution, position of the source with respect to the neutron detector, etc.),
3. the neutron cross sections for the materials of the scintillator and its surroundings,
4. the neutron transport effects including relativistic kinematics,
5. the production of secondary charged particles,
6. the light production by charged particles including wall effects, and
7. the PH resolution of the detector system.

The light production by charged particles is given by proton and alpha particle light-output functions, which are to be determined from the experimental PH response using the PTB-developed SPEKT code [Die78]. The standard steps to obtain the proton light-output $L_p(E_p)$ function are as follows:

1. The zero-intercept channel (corresponding to zero pulse height) is determined for the complete electronics chain (preamp-main amp-ADC) by means of an electronic pulser. The recoil-edge channel of all spectra are then corrected accordingly.
2. The experimental PH spectra for various $\gamma$-ray sources with recoil electron energies $0.342 \leq E \leq 1.609$ MeV are accumulated for all detectors. The Compton edges for these spectra are determined with the aid of the GRESP code [Die82a] (see Table 2). The position $L_e$ (in channels) of the Compton edge should be directly proportional to $E$, with a slope $G_\gamma$ [Tic92]

$$L_e(E) = G_\gamma(E - E_0), \tag{6.1}$$

Table 6.1: Compton-edge position as a function of electron energy for detectors calibrated at PTB.

| $E$(MeV) | T1 | R1 | B2 |
|---|---|---|---|
| 0.336 | 133.0 | 131.0 | 30.1 |
| 0.472 | 190.0 | 185.7 | 43.6 |
| 0.634 | 256.8 | 251.5 | 58.6 |
| 0.694 | 281.6 | 274.4 | 64.7 |
| 0.902 | 367.2 | 359.0 | 84.6 |
| 1.056 | 428.3 | 420.0 | 99.7 |
| 1.607 | 644.4 | 630.6 | 153.8 |

where $E_0$ is a small offset of 5 keV. This was not the case for the entire energy ($E$) range of interest for detectors R1 and T1 due to an electronic PH nonlinearity introduced by the Hamamatsu phototube/base assemblies.

3. The single-scattering parts of the PH response spectra obtained for different neutron energies are fitted by rectangular distributions whose rightmost edges are folded with a Gaussian resolution function. A single-scattering edge channel position $L_p(E_p)$ (where $E_p$ is the maximum proton recoil energy) and a Gaussian folding parameter are obtained from each neutron PH spectrum.

4. The experimental PH resolution folding parameter $\frac{dL}{L}$ is established as a function of $L$ (light-output units given by $L_p(E_p)/G_\gamma$) according to the expression

$$\frac{dL}{L}(E) = \sqrt{A^2 + \frac{B^2}{L} + \frac{C^2}{L^2}}, \tag{6.2}$$

where the variables $\{A, B, C\}$ are determined by fitting a plot of $\frac{dL}{L}(E)$ against L using Equation 6.2.

5. the light-output function for protons is produced by plotting $E$ versus $E_p$ and smoothly interpolating between points, creating a numerical table for $E_p \leq 8.0$ MeV. A linear fit

is used to represent $E(E_p)$ for $E_p$>8.0 MeV.

6. the mean energy and energy spread of the incident neutron energies for the NRESP calculations were derived from the experimental TOF spectra. The experimental neutron TOF spectrum part belonging to the breakup continuum is transformed into energy. The mean energy and width were determined for each TOF slice or window used to generate an experimental PH spectrum. A rectangular energy distribution was used in the NRESP code with a mean energy and width corresponding to that obtained for each experimental TOF window. For the monoenergetic neutrons, the width of the incoming neutron energy distribution was derived from the energy loss of the deuterons along the gas target. Otherwise the energy distribution width derived from the experimental TOF spectra would be too large because of the electronic time resolution.

7. The table and function description for $E(E_p)$, the parameters $\{A, B, C\}$, the detector dimensions and the incoming neutron energies are stored in input files to be used by the NRESP7 program, which then generates PH responses with finite Gaussian resolutions set by the parameter given by Equation 6.2. The PH spectrum gain is adjusted according to the $G_\gamma$ factor.

8. The resulting NRESP7-generated PH spectra are fitted to the experimental ones with the same $E_n$, thus obtaining gain correction factors $c_x$ which are then applied to the proton light-output function. The process is then iterated until the gain correction factors are close to unity (typically $1.00 \pm 0.02$).

9. The PH spectra were corrected for gain shifts/drifts during the measurement period, derived from monoenergetic photon source measurements under the same conditions and from full gamma and zero-intercept calibration procedures before and after the neutron beam measurements. This shift was in the order of $2 - 3\%$ (this could have been reduced if gain stabilization of the PM were used). In fact, the PTB detector

(D1) was stabilized with an LED, making its gain shift less than 1% .

### 6.2.3 Phototube Nonlinearity Problem

The iteration procedure described in Section 6.2.2 assumes a linear relationship between the detector's pulse-height response and the maximum recoil energy of an electron in the scintillator due to a $\gamma$-ray source with a well-defined energy [Tic92]. The Hamamatsu H1161 phototubes and base assemblies employed for detectors R1 and T1 show a nonlinear behavior in the form of pulse-height saturation for currents above a certain threshold. This effect manifests itself as a decrease in slope for the plot of $L_e$ versus $E$ (electron recoil energy) starting at energies above 1.612 MeV. Because of the lack of suitable $\gamma$-ray sources the shape of the nonlinearity introduced by the phototube is not accurately known for $E > 1.612$ MeV, so it is possible to relate $E$ to $E_p$ in the standard way only for $E \leq 1.612$ MeV. The single-

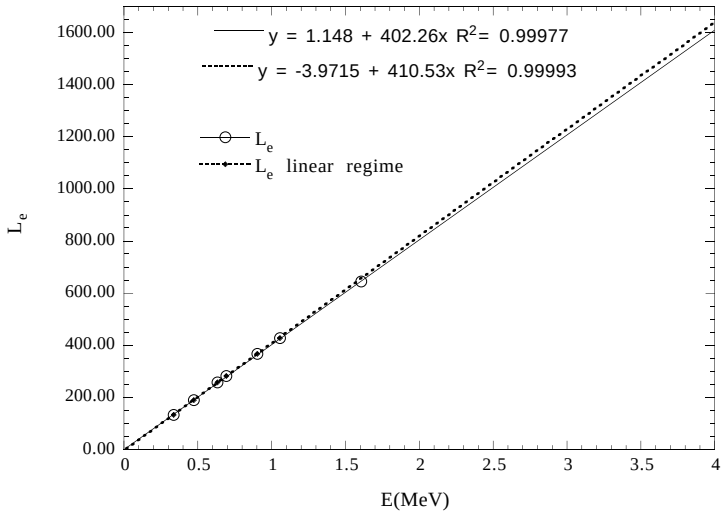


Figure 6.1: Compton-edge position as a function of electron energy for detector T1.

scattering edge channel positions $L_p(E_n)$ as well as Gaussian folding parameters were found for neutron PH responses using the method described in Section 6.2.2. We obtained the gain factor $G_\gamma$ using gamma sources with energies in the linear regime only. The proton light-output function was then generated in the following way:

1. A reference proton light-output function [Tic92] was used as a trial function:

$$E(E_p) = \begin{cases} 0.07269E_p + 0.11237{E_p}^2 & 0 < E_p < 1.5 \text{ MeV} \\ -0.20570 + 0.35260E_p + 0.01343E_p^2 + 0.00250E_p^3 & \\ & 1.5 < E_p < 3.5 \text{ MeV} \\ -0.25999 + 0.34141E_p + 0.03303E_p^2 + 0.00092E_p^3 & \\ & 3.5 < E_p < 8.0 \text{ MeV} \\ -1.43180 + 0.69325E_p & 8.0 < E_p < 20.0 \text{ MeV} \end{cases} \tag{6.3}$$

2. We generated PH responses using NRESPR1 (NRESPT1 for detector 1), expanded using the linear gain $G_\gamma$ and then folded with a Gaussian resolution function.

3. Each MC-generated response was fitted to its corresponding experimental spectrum, thus obtaining a compression factor $c_x$. The $c_x$ factor multiplies the corresponding $E \lessapprox 1.6$ MeV value given by Equation 6.3. For values of $E \gtrapprox 1.6$ MeV we cannot tell what proportion of $c_x$ is due to real deviations from the reference light-output function 6.3 and how much is due to nonlinearities introduced by the electronics. For detectors R1 and T1 we see that $c_x$ is slightly above unity up to $E \sim 1.6$ MeV.[1] For $E \gtrsim 1.6$ MeV the initial $c_x$ (first iteration) drops rapidly. This is expected because of the saturation effect introduced by the phototubes (see Tables 6.2 and 6.3).

4. Since we do not know the shape of nonlinearity introduced by the electronics, a correction factor $c_{xlast}$ for $E$ closest to but below $E = 1.6$ MeV is used to correct all

[1] Fits become less meaningful for the lowest neutron energy because the threshold is too close to the edge of the PH spectrum. Hence, the $c_x$ at the lowest neutron energy is not used as a correction factor to find the proton light-output function.

Table 6.2: Fit factors $c_x$ and fluence comparison ratios obtained for detector R1.

| $E_p$ (MeV) | $E$(MeV) Ref. Polynomial | Initial $c_x$ | $\frac{F_{R1}}{F_{D1}}$ | Final $c_x$ |
|---|---|---|---|---|
| 1.219 | 0.256 | 1.1363 | 0.6806 | 0.9914 |
| 1.776 | 0.477 | 1.0694 | 1.0326 | 0.9642 |
| 2.032 | 0.587 | 1.0318 | 0.9908 | 0.9737 |
| 2.287 | 0.701 | 1.0291 | 0.9876 | 0.9969 |
| 2.542 | 0.818 | 1.0221 | 0.9938 | 0.9972 |
| 2.789 | 0.936 | 1.0288 | 0.9900 | 1.0029 |
| 3.296 | 1.192 | 1.0221 | 0.9695 | 1.0008 |
| 3.800 | 1.464 | 1.0284 | 0.9995 | 0.9997 |
| 4.046 | 1.601 | 1.0282 | 1.0320 | 1.0098 |
| 4.307 | 1.750 | 1.0027 | 1.0210 | 0.9870 |
| 4.545 | 1.888 | 1.0156 | 1.0157 | 1.0013 |
| 4.802 | 2.039 | 1.0050 | 1.0262 | 0.9949 |
| 5.043 | 2.184 | 1.0064 | 1.0060 | 1.0016 |
| 5.283 | 2.330 | 0.9964 | 1.0034 | 0.9948 |
| 5.559 | 2.501 | 0.9941 | 1.0053 | 1.0004 |
| 6.060 | 2.817 | 0.9856 | 1.0109 | 1.0012 |
| 7.058 | 3.472 | 0.9640 | 0.9561 | 1.0012 |
| 9.012 | 4.816 | 0.9152 | 0.9890 | 1.0002 |
| 9.924 | 5.448 | 0.8877 | 0.9928 | 1.0005 |
| 10.858 | 6.096 | 0.8913 | 0.9911 | 1.0051 |
| 11.965 | 6.863 | 0.8683 | 0.9998 | 1.0052 |
| 14.142 | 8.372 | 0.8435 | 1.0067 | 1.0113 |

Table 6.3: Fit factors $c_x$ obtained for detector T1.

| $E_p$ (MeV) | $E$(MeV) Ref. Polynomial | Initial $c_x$ | $\frac{F_{T1}}{F_{D1}}$ | Final $c_x$ |
|---|---|---|---|---|
| 1.221 | 0.256 | 1.1350 | 0.6629 | 0.9903 |
| 1.777 | 0.477 | 1.0200 | 1.0330 | 0.9914 |
| 2.033 | 0.588 | 1.0070 | 0.9985 | 0.9852 |
| 2.288 | 0.701 | 1.0000 | 0.9959 | 0.9815 |
| 2.542 | 0.818 | 1.0034 | 1.0071 | 0.9918 |
| 2.79 | 0.937 | 1.0059 | 1.0081 | 0.9956 |
| 3.296 | 1.192 | 1.0027 | 0.9822 | 0.9930 |
| 3.803 | 1.465 | 1.0012 | 1.0207 | 0.9906 |
| 4.05 | 1.603 | 1.0035 | 1.0635 | 1.0010 |
| 4.309 | 1.751 | 1.0060 | 1.0104 | 0.9868 |
| 4.55 | 1.891 | 1.0070 | 1.0366 | 0.9953 |
| 4.804 | 2.04 | 1.0026 | 0.9920 | 0.9837 |
| 5.048 | 2.187 | 0.9974 | 1.0256 | 0.9840 |
| 5.281 | 2.329 | 0.9900 | 1.0019 | 0.9838 |
| 5.565 | 2.504 | 0.9805 | 1.0164 | 0.9916 |
| 6.066 | 2.821 | 0.9680 | 1.0182 | 0.9906 |
| 7.062 | 3.474 | 0.9482 | 1.0167 | 0.9943 |
| 9.073 | 4.858 | 0.8924 | 0.9962 | 0.9796 |
| 9.929 | 5.451 | 0.8790 | 0.9781 | 0.9822 |
| 10.869 | 6.103 | 0.8671 | 0.9957 | 0.9875 |
| 11.97 | 6.866 | 0.8400 | 0.9945 | 0.9813 |
| 14.138 | 8.369 | 0.8187 | 1.0211 | 0.9756 |

the $E > 1.6$ MeV in the proton light-output function. The values of $c_x$ obtained for $E > 1.6$ MeV are divided by $c_{xlast}$, obtaining correction factors $c_{nlinear}$ which are plotted against their corresponding value of $E$. We fit polynomial functions to these plots, obtaining correction functions $\xi(E)$ (see Figure 6.2). For detector T1 we get

$$\xi(E) = 0.9835 + 0.04386E - 0.02538E^2 + 0.003246E^3 - 1.345\times10^{-4}E^4, \tag{6.4}$$

and for detector R1

$$\xi(E) = 0.9918 + 0.02834E - 0.02260E^2 + 0.003308E^3 - 1.559\times10^{-4}E^4. \tag{6.5}$$

5. We incorporated the correction function into the NRESPR1 and NEFFT1 codes, where $\xi(E)$ is multiplied by the gain factor $G_\gamma$ to simulate the phototube nonlinearity and assign a channel position to each event corresponding to an energy $E$

$$L_p(E) = G_\gamma \xi(E) E. \tag{6.6}$$

After two iterations this procedure yielded $c_x$ factors very close to unity (see last column on Tables 6.2 and 6.3).

### 6.2.4 Comparison of Experimental and Simulated Pulse Heights and Fluences

The simulated pulse-height responses were normalized to a fluence of 1 neutron/cm$^2$. When fitting simulated responses to experimental ones we then obtained a "count rate" fit factor ($C_{R1}$ for detector R1, $C_{T1}$ for detector T1, etc.). This factor is by definition the neutron fluence at a particular neutron energy. For every detector we calculated the normalized quantity

$$F_d = \frac{C_d}{D_d M_d}, \tag{6.7}$$

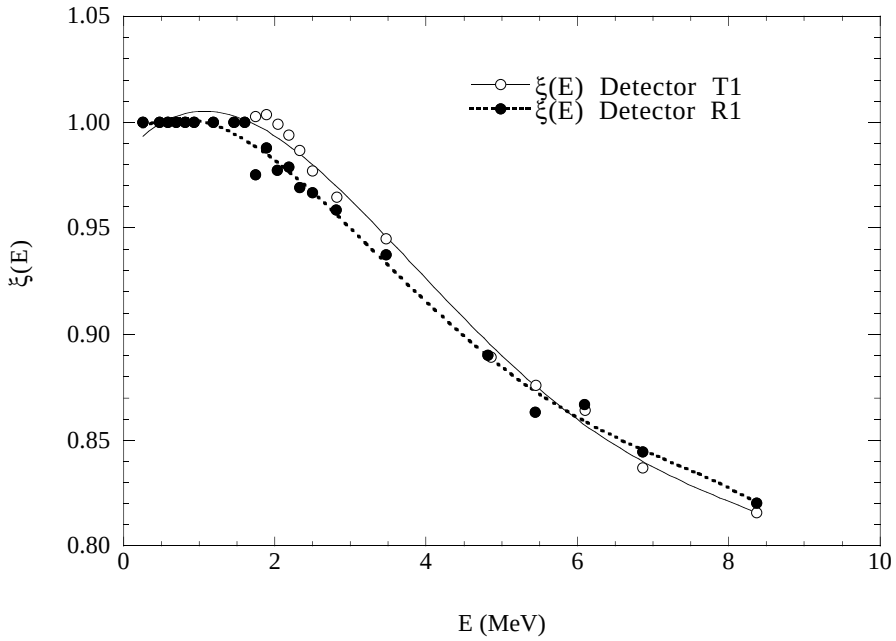


Figure 6.2: $\xi(E)$ for detectors T1 and R1.

where $d = \{T1, R1, D1\}$, $D_d$ is the divide-down factor which decreases the rate of events going into the computer during the experiment and $M_d$ is the monitor yield (see Section 6.2.1) taken during the irradiation of a particular detector at a specific mono-energetic neutron energy. All detector count rates were corrected for dead time. The probability for double-event detection from one neutron pulse was always below 1% and therefore neglected.

The reference detector $D1$ had already been fully studied and characterized at PTB. If the fluences were calculated correctly for detectors T1 and R1, then the ratios $\frac{F_{T1}}{F_{D1}}$ and $\frac{F_{R1}}{F_{D1}}$ should be near unity for all neutron energies investigated. In fact, these factors are

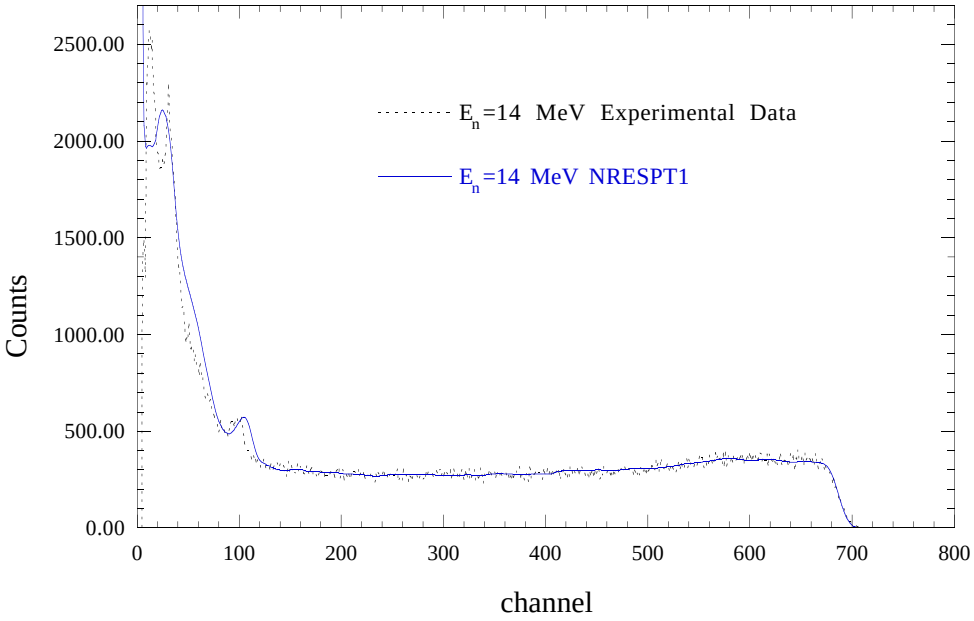


Figure 6.3: Comparison of experimental and calculated PH responses for detector T1 at $E_n \approxeq 14$ MeV.

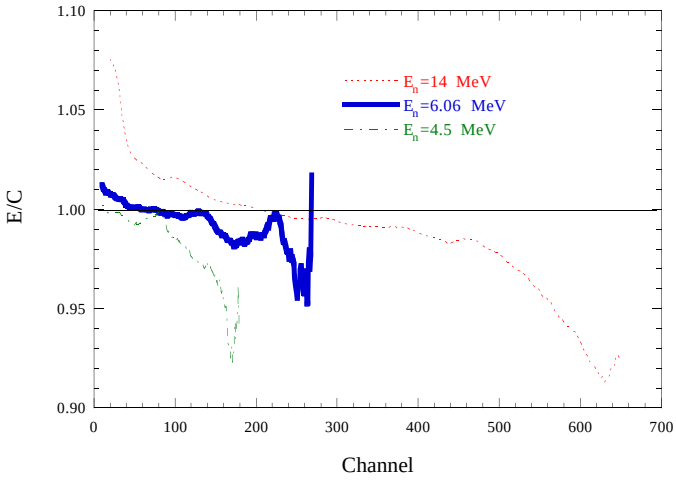


Figure 6.4: $r_i^{\frac{E}{C}}$ factors for detector T1 at various neutron energies.

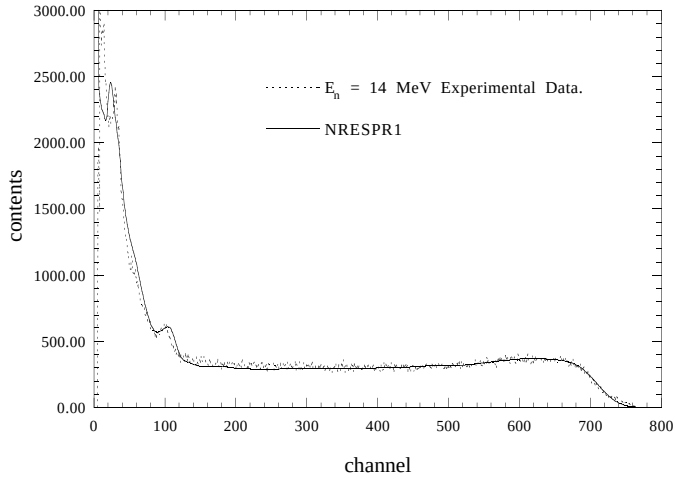


Figure 6.5: Comparison of calculated and experimental PH responses for detector R1 at $E_n = 14$ MeV.

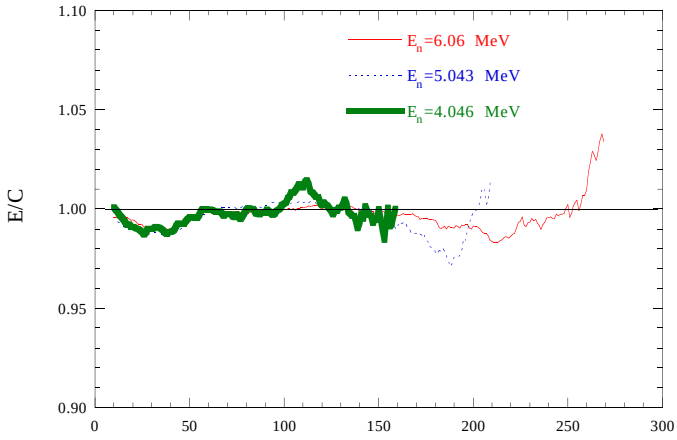


Figure 6.6: $r_i^{\frac{E}{C}}$ factors for detector R1 at various neutron energies.

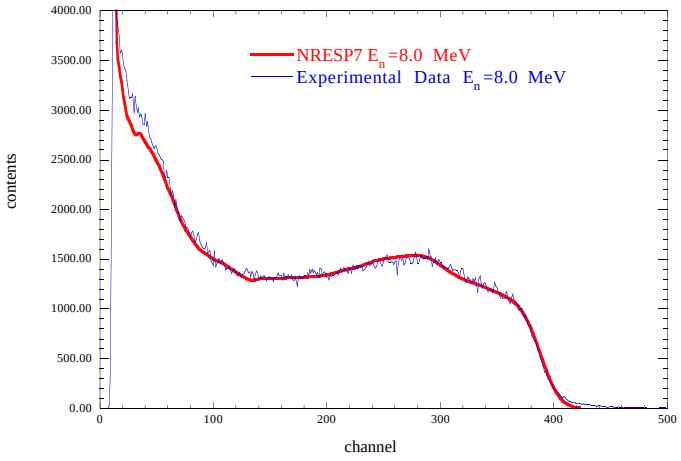


Figure 6.7: Comparison of calculated and experimental PH responses for detector B2.

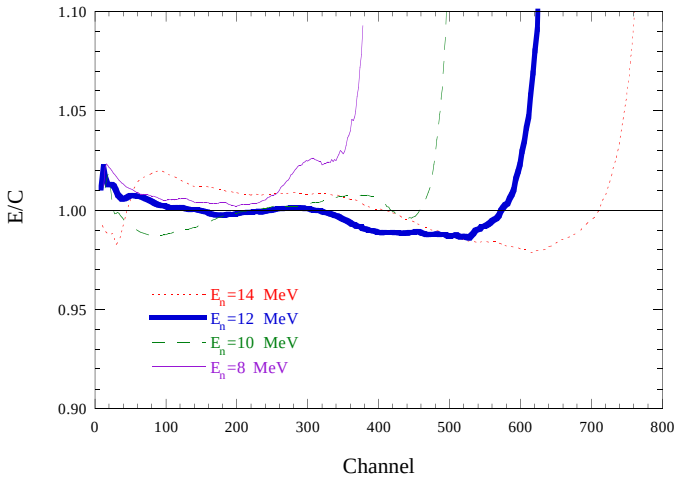


Figure 6.8: $r_i^{\frac{E}{C}}$ factors for detector B2 at various neutron energies.

within 1.00±0.04 for almost all energies (see Tables 6.2 and 6.3) and are comparable to the ones obtained by Tichy *et al.* [Tic92]. The agreement in shape between simulated and experimental responses was also comparable to Tichy's results (see Figures 6.5 and 6.3). A measure of this agreement is the ratio between areas of corresponding normalized MC-simulated and experimental PH responses as a function of lower integration channel $i$

$$r_i{}^{\frac{E}{C}} = \frac{\sum_{k=i}^{1023} {h_k}^E}{\sum_{k=i}^{1023} {h_k}^C}, \tag{6.8}$$

where ${h_k}^E$ and ${h_k}^C$ are the channel $k$'s contents of the experimental and the normalized simulated spectrum respectively. The behavior of $r_i{}^{\frac{E}{C}}$ is shown for some values of $E_n$ in figures 6.4 and 6.6. The systematic deviations of $r^{\frac{e}{c}}$ from 1.0 depend on the region of the PH spectrum and the neutron energy. For PH channels near the single-scattering edge the deviations reflect disagreements in shape between simulated and experimental spectra due to failure of the Gaussian resolution function to reproduce the experimental PH edge given the parameters found for Equation 6.2. Shortcomings in accounting for the PH non-linearity introduced by the electronics would cause an inaccurate estimate of the proton light-output

Table 6.4: Fit factors $c_x$ and fluence-comparison ratios obtained for detector B2.

| $E_p$ (MeV) | $\frac{F_{T1}}{F_{D1}}$ | $c_x$ |
|---|---|---|
| 1.757 | 1.0581 | 1.0198 |
| 2.009 | 1.0461 | 0.9871 |
| 2.259 | 1.0351 | 0.9913 |
| 2.509 | 0.9995 | 0.9984 |
| 2.756 | 0.9885 | 1.0092 |
| 3.259 | 0.9858 | 0.9856 |
| 3.759 | 0.9809 | 0.9586 |
| 3.985 | 0.9987 | 0.9755 |
| 4.262 | 1.0130 | 0.9942 |
| 4.476 | 1.0101 | 0.9790 |
| 4.755 | 1.0372 | 0.9909 |
| 4.965 | 1.0027 | 0.9774 |
| 5.232 | - | 0.9975 |
| 5.473 | 1.0088 | 0.9818 |
| 5.966 | 0.9999 | 0.9796 |
| 6.949 | 0.9879 | 0.9750 |
| 8.045 | 1.0263 | 1.0172 |
| 9.975 | 1.0357 | 0.9981 |
| 11.988 | 1.0157 | 0.9847 |
| 14.136 | 1.0109 | 0.9802 |

function and also lead to $r\frac{e}{c}$ deviations. At neutron energies above 8 MeV light production by the process $^{12}$C(n,3$\alpha$)n becomes important for the lower PH channels. The cross section for this breakup process is not accurately known, introducing inaccuracies in the NRESP pulse-height calculation. The results obtained from this analysis give us confidence in correct performance of the NRESPR1 and NRESPT1 programs, and the adequacy of the light-output function for protons found for detectors R1 and T1. Figures 6.7 and 6.8 show the agreement between experimental and simulated pulse-shape responses for various incident neutron energies.

Detector B2 (with linear electronics) was characterized according to the steps described in Section 6.2.2. Table 6.4 shows the final $c_x$ values obtained and the comparison of fluences with detector D1.

## 6.3 Measurements at TUNL

### 6.3.1 Introduction

The programs NEFF7, NEFFT1, and NEFFR1 generate efficiencies for the PTB-calibrated detectors B2, T1 and R1 for any given PH threshold. Other detectors of the ring, transmission and Bicron-type were used in the $a_{nn}$ experiment. Presumably all these detectors had similar efficiencies to their homologues characterized at PTB. This assumption was tested by direct efficiency measurements at TUNL using the $^2$H(d,n)$^3$He reaction as a source of neutrons.

### 6.3.2 Experimental Setup

A neutron field was generated by a pulsed deuteron beam bombarding a deuterium gas cell located in TUNL's Time-of-Flight target area. The deuterium gas cell pressure was 1.00±0.005 atm. The average beam current incident on the gas cell was ∼30 nA. The efficiencies were measured simultaneously for neutron detector pairs at 0° and 60° with respect to the deuteron beam axis in order to cover a wider neutron energy range (see Figure 6.9). Both detectors were placed at the same height as the gas cell with the aid of a telescope. Neutron energies were changed using the Van de Graaff accelerator in a sweep from 3.93 MeV up to 13.03 MeV (and then down again) in steps of roughly 0.5 MeV. The neutron detectors were interchanged after an energy sweep was completed so both would be exposed to the full range of available neutron energies. The measurements were done using the time-of-flight (TOF) technique with the start signal provided by the neutron detector and the stop provided by the pickoff signal from the pulsed beam. Pulse-shape

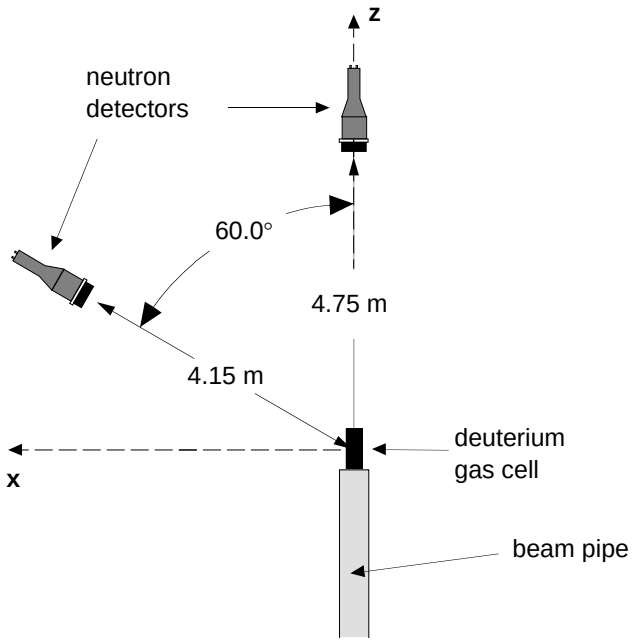


Figure 6.9: Top view of the general layout of neutron detectors for the TUNL efficiency measurements.

discrimination (PSD) was applied on the anode signals of the neutron detectors by means of Canberra 2160A modules. Gamma events were later rejected using software cuts. A detector's integrated and amplified dynode signals were used for the setting of bias thresholds. Time-to-Amplitude converters (TACs) were used for TOF and PSD spectroscopy. A timing coincidence circuit between the stop and start signals provided TTL gates for the analog-to-digital converters (ADCs). Each TAC, PSD and PH linear signal was sent to a channel of an EG&G AD413A ADC which digitized them for mass storage and off-line analysis.

The PH thresholds for all detectors were determined using $^{137}$Cs gamma sources. The convention used at TUNL is to set the 1×Cs Compton-edge channel at one-half the

height of the maximum near the Compton edge. This point is equivalent to an electron recoil energy of $0.47 \lesssim E \lesssim 0.55$ MeV, depending on the detector resolution. In addition, a $^{137}$Cs gamma PH spectrum was taken for each detector roughly every 8 hours to check the phototubes' gain stability.

### 6.3.3 Data Analysis

The efficiency for each detector is extracted from the yields/BCI ($Y_d$) from the neutron TOF peak from the $^2$H(d,n)$^3$He reaction (BCI is a unit of integrated beam current or charge deposited by the beam on the gas cell). The efficiency is related to $Y_d$ by

$$\varepsilon(E_n) = \frac{\eta_f Y_d}{T_{gc} \frac{d\sigma}{d\Omega}(E_n, \vartheta_{lab})}, \tag{6.9}$$

where $\frac{d\sigma}{d\Omega}(E_n, \vartheta_{lab})$ is the cross section for the $^2$H(d,n)$^3$He reaction as a function of neutron energy $E_n$ and lab neutron production angle $\vartheta_{lab}$ [Dro78], $T_{gc}$ is the neutron attenuation factor due to the deuterium gas and the construction materials of the gas cell (0.980±0.005) for all neutron energies and emission angles considered [Ped86]. The net neutron yield/BCI $Y_d$ is corrected for dead time and background in the TOF spectrum. The factor $\eta_f$ is given by

$$\eta_f = (\Omega N_t N_i)^{-1}, \tag{6.10}$$

where $\Omega$ is the solid angle subtended by the neutron detector. $N_i$ is the number of deuterons/BCI incident on the gas cell and $N_t$ is the density of deuterium atoms in the gas cell

$$N_t = \frac{lP}{RT}, \tag{6.11}$$

where $l$ is the length of the gas cell (3.1±0.05 cm), $P$ is the deuterium gas cell pressure and $T$ the ambient temperature during the measurement (∼293.6±0.5° K).

The uncertainty in the distance from the center of the gas cell to the center of the neutron detectors is estimated be $\Delta d = \pm 1.0$ cm (out of ∼4 m). For some detectors

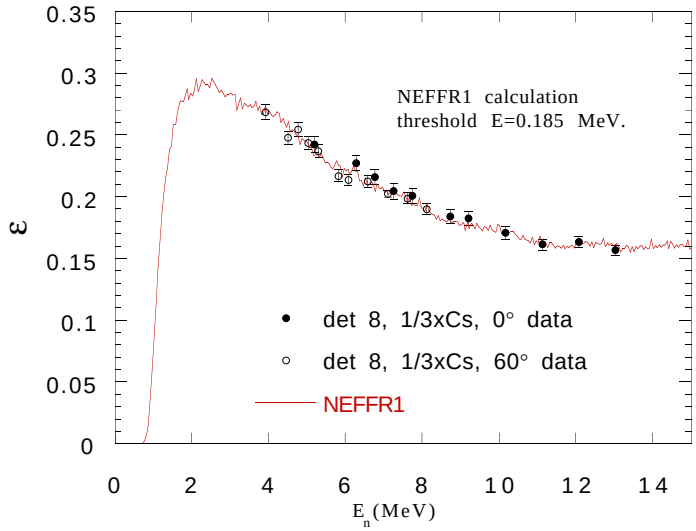


Figure 6.10: Comparison of TUNL-obtained efficiencies to NEFFR1 calculations for detector R1.

(ring, transmission) the radii are assumed to have an uncertainty of $\Delta r_d = \pm 0.05$ cm due to irregularities in the shape of the glass housing. The estimated uncertainty for the efficiencies extracted at TUNL are $\lesssim \pm 2.5\%$ for most neutron energies considered.

## 6.4 Results

Neutron detection efficiencies were extracted for all neutron detectors used in the $a_{nn}$ experiment with the exception of detectors 2, 3, 14 and 15 because the count rates for triple events for these detectors were very low. Therefore we decided to concentrate the *nd* breakup analysis and efficiency determination on other detector pairs.

The efficiency determinations of most importance are those at $\frac{1}{3}\times$Cs, since this PH threshold was used for all neutron detectors in the $a_{nn}$ experiment. Figures 6.10, 6.11 and

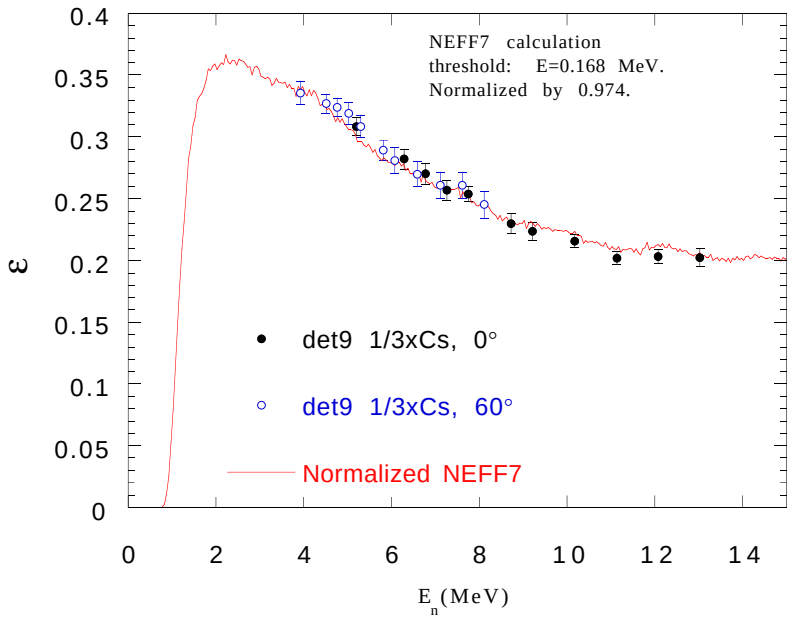


Figure 6.11: Comparison of TUNL-obtained efficiencies to NEFF7 calculations for detector B2.

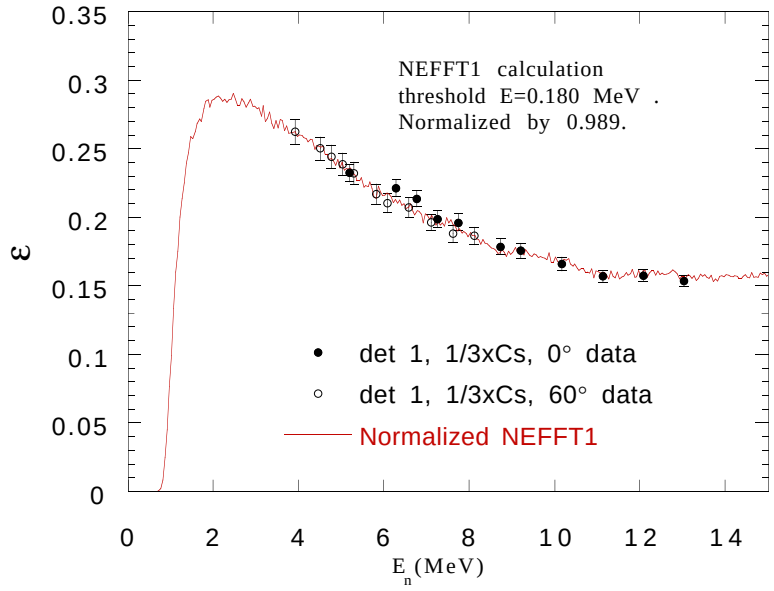


Figure 6.12: Comparison of efficiency for transmission-type detectors ($\frac{1}{3}\times$Cs threshold). The NEFFT1 calculation is normalized to the data.

6.12 show the TUNL-obtained efficiencies for detectors R1, B2 and T1 compared with the results of the associated Monte-Carlo calculated efficiencies. A normalization of ∼0.98 was applied to the calculated efficiencies to bring them in closer agreement with the TUNL experimental efficiencies. A systematic $E_n$-dependent deviation between experimental and calculated efficiencies is observed for all detectors (see Figure 6.13 where the deviation is shown for detector T1). This deviation is attributable to a combination of several effects:

1. Attenuation of neutrons in the gas cell and in air lowers the detected neutron yield by ∼3%. The attenuation becomes less significant with increasing $E_n$.

2. In-scattering of neutrons from the air surrounding the direct path between the gas cell and the detector increases the detected neutron yield, becoming less important with increasing $E_n$. This effect is difficult to calculate exactly, but it appears to be in the order of a few percent. It is expected that attenuation and inscattering effects should largely cancel each other out [Kle].

3. irregularities in the radial shape of the detector's housing lead to errors in the solid angle estimate.

In the analysis of the $a_{nn}$ experiment we use the normalized efficiency calculations because the Monte-Carlo codes that calculate *nd* breakup cross sections assume detectors with standard scintillator dimensions.

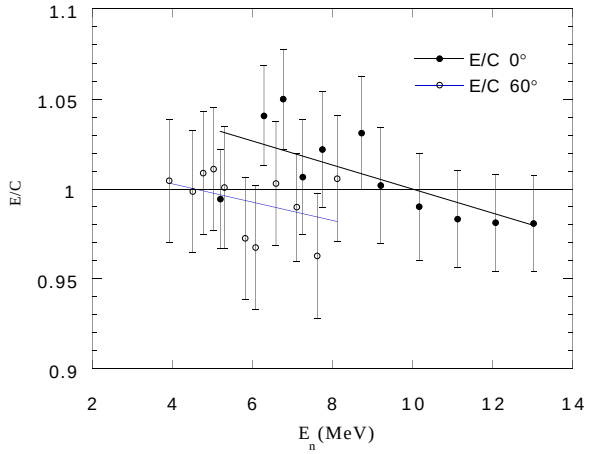


Figure 6.13: Deviation (ratio of experimental and calculated efficiency E/C) of TUNL experimental efficiencies from normalized NEFFT1 calculations for detector T1.

# Chapter 7

# Results and Conclusions

Finite-geometry *nn* FSI cross sections were determined at lab production angles $\theta_{nn}$ = 20.5°, 28.0°, 35.5° and 43.0°. Cross-section data points at the extremes of the S-curves were excluded, because for our bias settings the detectors' efficiencies become threshold and resolution dependent for $E_n \lesssim 2.0$ MeV, leading to errors in the respective cross-section values of ∼50% or more.

The first three experimental runs were left out of the analysis because of irregularities in the center-detector pulse height, which introduced problems in finding the luminosity from the *nd* elastic scattering scattering yields. Despite the exclusion of these breakup data, the statistical precision of the peak *nn* FSI cross sections remained better than 5%. Figures 7.1, 7.2, 7.3 and 7.4 show the experimental cross sections compared to Monte-Carlo-generated cross-section curves for a range of values of $a_{nn}$. The error bars are statistical only.

## 7.1 Resulting $a_{nn}$ from the TUNL Experiment

### 7.1.1 Extraction of $a_{nn}$ from the Absolute Cross Sections

Values for $\chi^2$ were obtained by comparing experimental cross sections to Monte-Carlo-generated finite-geometry $nn$ FSI cross sections based on rigorous 3N point-geometry calculations for values of $a_{nn}$ ranging from -17.0 to -20.0 fm. Using the approach described in Section 5.6.1 we obtained a function for $\chi^2(a_{nn})$ whose minimum corresponds to $a_{nn}$ for a particular $nn$ FSI configuration. Table 7.1.1 shows our results. The statistically-weighted

| i | $\theta_{nn}(^\circ)$ | $a^i_{nn}$ (fm) | $(\Delta a^{stat}_{nn})_i$ (fm) | $\Delta a^{syst}_{nn}$ (fm) |
|---|---|---|---|---|
| 1 | 20.5° | $-18.9$ | $\pm 0.2$ | $\pm 0.6$ |
| 2 | 28.0° | $-18.8$ | $\pm 0.2$ | $\pm 0.6$ |
| 3 | 35.5° | $-17.7$ | $\pm 0.4$ | $\pm 0.6$ |
| 4 | 43.0° | $-18.8$ | $\pm 0.4$ | $\pm 0.7$ |

Table 7.1: $a_{nn}$ values extracted from the absolute $nn$ FSI cross sections.

average of $a_{nn}$ is

$$a_{nn} = \frac{\sum_i \frac{a^i_{nn}}{(\Delta a^{stat}_{nn})_i{}^2}}{\sum_i \frac{1}{(\Delta a^{stat}_{nn})_i{}^2}}, \tag{7.1}$$

and the statistical error of the mean [Bev69] is given by

$$\Delta a^{stat}_{nn} = \sqrt{\frac{1}{\sum_i \frac{1}{(\Delta a^{stat}_{nn})_i{}^2}}}. \tag{7.2}$$

The statistically-averaged neutron-neutron scattering length is then $a_{nn} = -18.73 \pm 0.13$ fm. The systematic error of the average $a_{nn}$ is taken to be $\pm 0.6$ fm (representative of the systematic error of $a_{nn}$ for each $nn$ FSI configuration). Finally, adding the systematic and statistical uncertainties in quadrature we obtain $a_{nn} = -18.7 \pm 0.6$ fm.

| i | $\theta_{nn}(^\circ)$ | $a^i_{nn}$ (fm) | $\Delta a^i_{nn}$ (fm) |
|---|---|---|---|
| 1 | 20.5° | −19.0 | ±0.7 |
| 2 | 28.0° | −18.3 | ±0.9 |
| 3 | 35.5° | −18.8 | ±1.2 |

Table 7.2: $a_{nn}$ extracted from the shapes of three $nn$ FSI cross-sections.

### 7.1.2 Extraction of $a_{nn}$ from Cross-Section Shapes

Using the methods described in Section 5.6.1 we extracted $a_{nn}$ from the shape of the cross sections of three $nn$ FSI configurations at production angles $\theta_{nn} = 20.5^\circ$, $28.0^\circ$ and $35.5^\circ$ (see Table 7.1.2). The experimental cross section at $\theta_{nn} = 43.0^\circ$ had too few points for a meaningful determination of $a^i_{nn}$ ($i$ is the $nn$ FSI configuration index) from the cross-section shape. The $a^i_{nn}$ values can be averaged using the reciprocal-squared statistical uncertainties as weighting factors. The average $a^{shape}_{nn}$ is then given by

$$a^{shape}_{nn} = \frac{\sum_i \frac{a^i_{nn}}{{\Delta a^i_{nn}}^2}}{\sum_i \frac{1}{{\Delta a^i_{nn}}^2}}. \tag{7.3}$$

The error of the mean is given by

$$\Delta a^{shape}_{nn} = \sqrt{\frac{1}{\sum_i \frac{1}{{\Delta a^i_{nn}}^2}}}. \tag{7.4}$$

The average neutron-neutron scattering length extracted from the shapes of the $nn$ FSI cross sections is $a^{shape}_{nn} = -18.8 \pm 0.5$ fm. The agreement between the $a_{nn}$ values determined using the shape and the absolute cross-section methods is a good indication that, within the estimated uncertainties, our average value for $a_{nn}$ extracted from the absolute cross sections is correct.

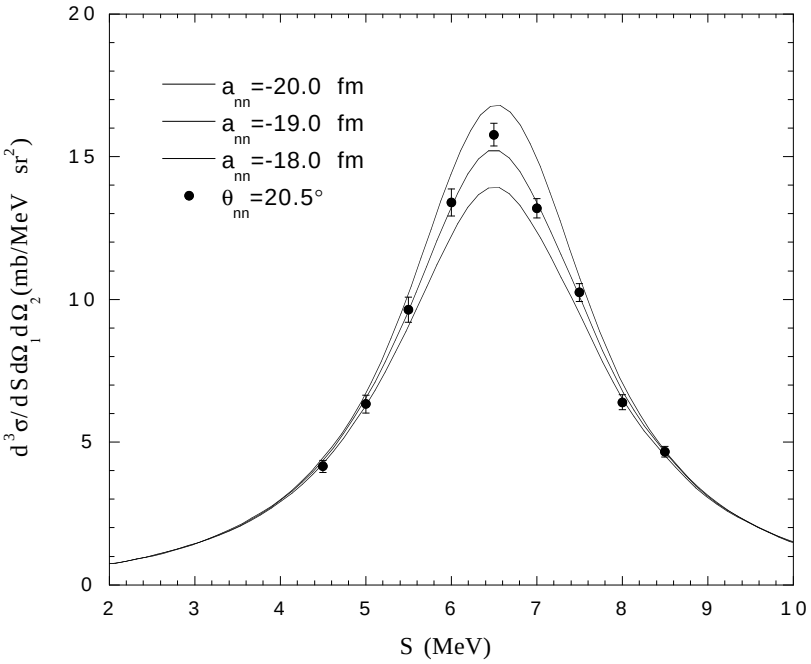


Figure 7.1: Cross section for $\theta_{nn} = 20.5°$.

## 7.2 Conclusions

### 7.2.1 Charge-Symmetry Breaking in the Nuclear Force

The effect of charge-symmetry breaking (CSB) on the nucleon-nucleon (NN) scattering lengths is given by

$$\Delta a_{CSB} = a_{pp}^N - a_{nn}^N, \tag{7.5}$$

where the superscript N refers to the purely nuclear scattering lengths. The experimentally-determined $a_{nn}$ includes contributions from nuclear and electromagnetic interactions. For a version of the Nijmegen potential, the $nn$ magnetic component of the experimental $a_{nn}$ varies between $-0.35$ and $-0.33$ fm [Mil90]. Therefore, our $a_{nn}^N = -19.0 \pm 0.6$ fm.

In meson-exchange theory CSB is introduced by a combination of isospin mixing

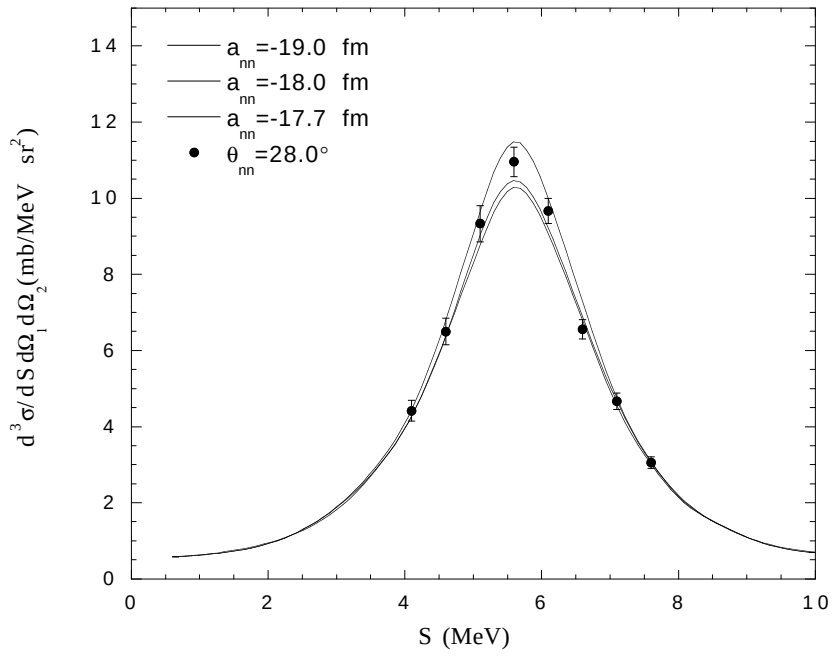


Figure 7.2: Cross section for $\theta_{nn} = 28.0°$. The cross-section datum obtained at $S = 3.6$ MeV was excluded because of difficulties in establishing a reliable estimate of the cross-talk background.

of vector mesons ($\rho - \omega$ mixing) and two-pion exchange. The separate contributions to CSB from these two processes is under debate [Coo79, Coo96], but the overall effect on the $nn$ and $pp$ scattering length difference is in the order of $\Delta a = \mid a_{nn}^N \mid - \mid a_{pp}^N \mid \sim 1$ fm, where $a_{nn}^N$ is the experimental $a_{nn}$ with an electromagnetic correction of $-0.2$ fm [Coo96]. Given that $a_{pp}^N = -17.3 \pm 0.4$ fm [Mil90] and our extracted $a_{nn}^N = -19.0 \pm 0.6$ fm, we obtain $\Delta a_{CSB}^{exp} = 1.6 \pm 1.0$ fm, in agreement with the meson-exchange CSB prediction.

The sign and magnitude of our $\Delta a_{CSB}^{exp}$ are also consistent with the $A = 3$ mirror nuclei binding-energy difference ($\Delta E = E(^3H) - E(^3He)$) calculations by Wu *et al.*, where the total calculated CSB contribution to the $\Delta E$ was $78 \pm 8$ keV [Wu90]. This suggests that the strength of the $nn$ interaction is greater than that of the $pp$ interaction, in agreement

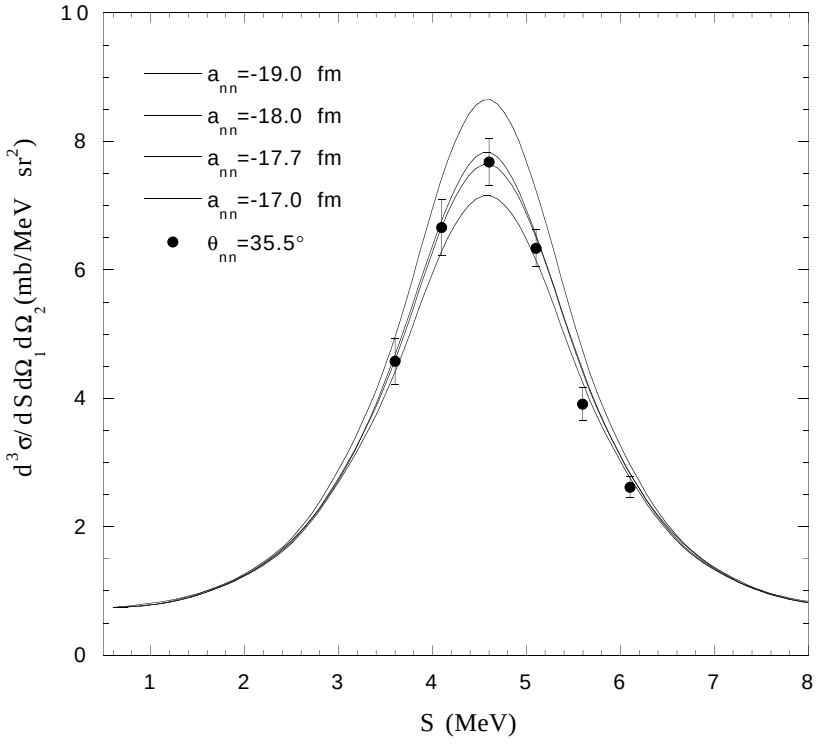


Figure 7.3: Cross section for $\theta_{nn} = 35.5°$. The cross-section datum at $S = 3.1$ MeV was excluded because of difficulties in establishing a reliable estimate of the cross-talk background.

with our results.

The difference between our extracted $a_{nn}$ and that of the average of the two $\pi^-$d capture experiments mentioned in Section 1.0.3 ($-18.6\pm0.3$ fm [Mil90]) is well within the uncertainties of both $a_{nn}$ values ($-0.1\pm0.7$ fm). Our result agrees with the average $\pi^-$d $a_{nn}$ determination, and departs drastically from the world-average $a_{nn} = -16.7\pm0.5$ [Mil90] for kinematically-complete *nd* breakup experiments, as will be discussed next.

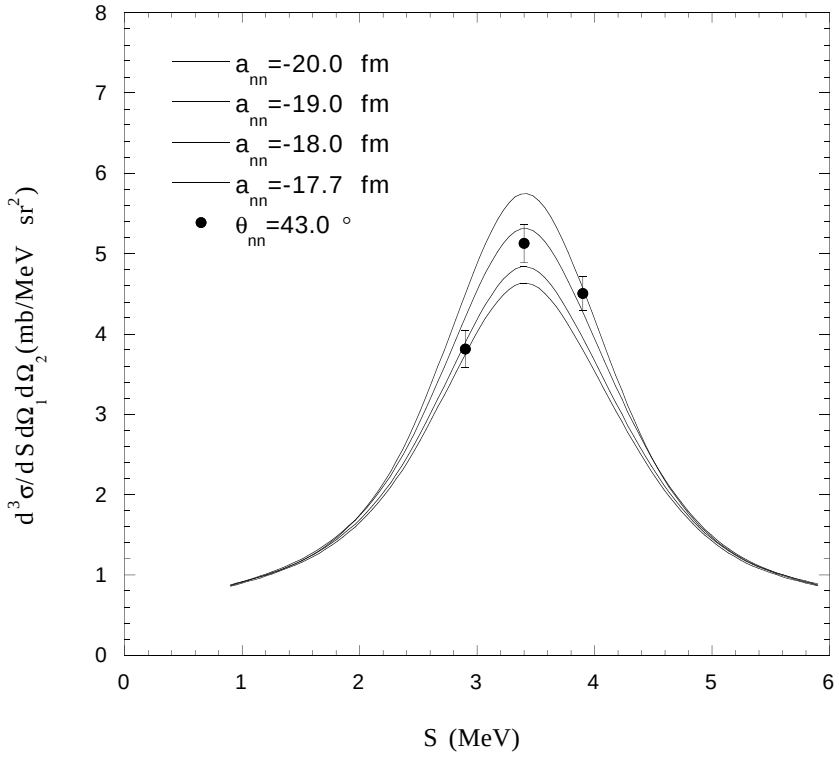


Figure 7.4: Cross section for $\theta_{nn} = 43.0°$.

### 7.2.2 Discrepancies With Erlangen's $a_{nn}$ Results

Before we started our experiment, we tried to obtain detailed information about the previous most accurate *nd* breakup $a_{nn}$ experiments [One78, vW79, Zei70, Zei74]. We hoped that it would be possible to analyze these older data with the rigorous approach used in this thesis. Unfortunately, this turned out to be impossible. Important information about detector bias settings, electronic dead time, scatterer composition, finite geometry, etc., were not available anymore, even from groups which are still involved in few-nucleon physics. One of the most active $a_{nn}$ groups at this time, the group around von Witsch of Bonn University, is about to start a new $a_{nn}$ experiment, in part because they do not

have enough information available to reanalyze their own accurate data obtained in an experiment performed in the late seventies [vW79].

We are convinced that the Erlangen group in their recent $a_{nn}$ experiment either overestimated their cross-talk background subtraction and/or made a mistake in the absolute normalization of their data. Unfortunately, they used the W-matrix method to calculate theoretical *nn* FSI cross sections [Fra88]. They obtained $a_{nn} = -17.0 \pm 1.0$ fm [Geb93]. Would they have used the rigorous calculations applied in the present work to fit their absolute cross-section data, they would have obtained $a_{nn} = -14.30 \pm 0.30$ fm [Glö96], probably triggering a more thorough investigation of possible background and normalization errors in their experiment.

Assuming that the only mistake in Erlangen's data was in the absolute normalization, we made a fit to the shape of their experimental *nn* FSI cross section using the method described in Section 5.6.2. Rigorous point-geometry cross-section calculations were performed for $\theta_{nn} = 25.0^\circ$ for $-15.0 \leq a_{nn} \leq -20.0$ fm in steps of 1.0 fm. No finite-geometry calculations were necessary since the experimental data were given in point-geometry form. Because systematic deviations are apparent for the left wing of the cross-section curve (see Figure 7.5), our shape analysis took into account the cross-section points within the range $4.1 \leq S \leq 8.1$ MeV only. From the shape of the experimental cross section we obtained $a_{nn}^{shape} = -17.9 \pm 0.5$ fm, which is in agreement with our average $a_{nn}$. This result suggests that the main problem of Erlangen's data was an improper normalization.

### 7.2.3 Absence of a Strong Three-Body Force

It has been proposed that the $a_{nn}$ discrepancy between $\pi^-$d and kinematically-complete *nd* breakup experiments could be due to a three-body force present in the exit channel of the latter reaction [Wit96]. In the case of our experiment, the signature of a three-body force would have been a clear and systematic dependence of $a_{nn}$ on the production angle $\theta_{nn}$ and a significant difference between our determined $a_{nn}$ and that of the $\pi^-$d

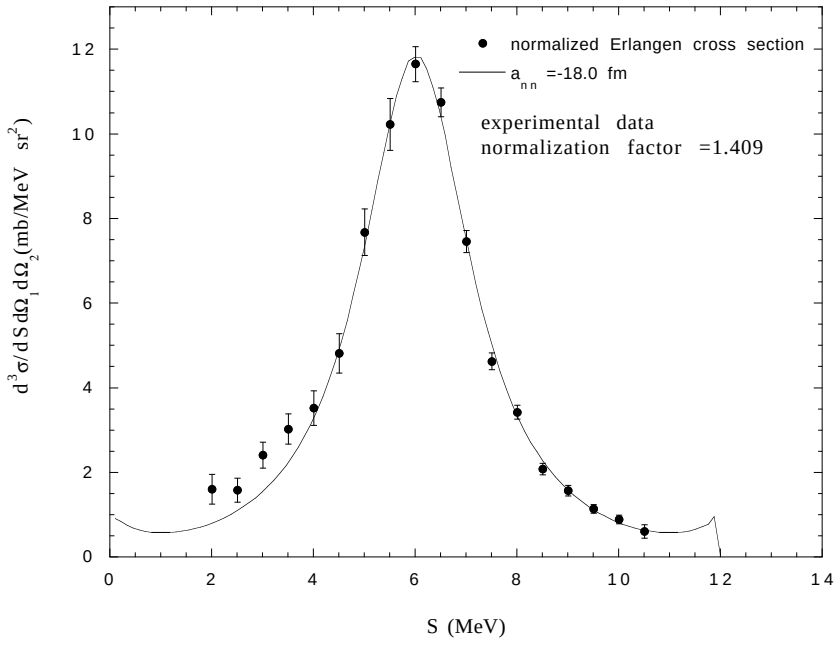


Figure 7.5: Cross-section comparison for $\theta_{nn} = 25.0^{\circ}$ between Erlangen's data normalized by 1.409 and rigorously-calculated $nn$ FSI cross sections for $a_{nn} = -18.0$ fm.

experiments. We neither observe a strong production-angle dependence for $a_{nn}$ (e.g., as expected from the Tucson-Melbourne three-body force using a cutoff parameter $\Lambda = 5.8 m_{\pi}$ (TM 3NF) [Wit96]) nor is our average value for $a_{nn}$ in disagreement with the $\pi^{-}$d results. Therefore, within our experimental uncertainties we do not see a 3NF effect. The meson-exchange effective model for the NN interaction accounts for the measured $nd$ breakup cross sections for the $nn$ FSI configurations. Hence, the effects from the suppression of quark/gluon degrees of freedom and relativistic effects on the $nd$ breakup cross section are negligible within the accuracy of the $a_{nn}$ value extracted from this experiment.

# Appendix A

# $nd$ breakup Cross-Section Tables

| | experimental cross sections ($\frac{mb}{sr^2 MeV}$) | | calculated finite-geometry cross sections ($\frac{mb}{sr^2 MeV}$) as a function of $a_{nn}$ (fm) | | | | |
|---|---|---|---|---|---|---|---|
| S (MeV) | $\frac{d^3\sigma(S)}{d\Omega_1 d\Omega_2 dS}$ | stat. error | $-17.0$ | $-17.7$ | $-18.0$ | $-19.0$ | $-20.0$ |
| nnfsr1 configuration ($\theta_{nn} = 43.0°$) | | | | | | | |
| 2.9 | 3.81 | 0.24 | 3.58 | 3.75 | 3.89 | 4.21 | 4.50 |
| 3.4 | 5.13 | 0.25 | 4.38 | 4.64 | 4.84 | 5.32 | 5.75 |
| 3.9 | 4.51 | 0.22 | 3.63 | 3.80 | 3.95 | 4.27 | 4.57 |
| nnfsr2 configuration ($\theta_{nn} = 35.5°$) | | | | | | | |
| 3.1 | 2.04 | 0.20 | 2.94 | 3.01 | 2.99 | 3.17 | 3.19 |
| 3.6 | 4.58 | 0.36 | 4.41 | 4.59 | 4.67 | 4.95 | 5.20 |
| 4.1 | 6.66 | 0.44 | 6.30 | 6.67 | 6.77 | 7.43 | 7.93 |
| 4.6 | 7.68 | 0.36 | 7.15 | 7.64 | 7.83 | 8.65 | 9.36 |
| 5.1 | 6.34 | 0.29 | 6.16 | 6.52 | 6.55 | 7.25 | 7.63 |
| 5.6 | 3.91 | 0.26 | 4.23 | 4.40 | 4.43 | 4.73 | 4.89 |
| 6.1 | 2.62 | 0.17 | 2.77 | 2.83 | 2.83 | 2.97 | 3.01 |
| nnfsr3 configuration ($\theta_{nn} = 28.0°$) | | | | | | | |
| 3.6 | 2.53 | 0.18 | 2.85 | 2.93 | 2.92 | 3.00 | 3.00 |
| 4.1 | 4.42 | 0.27 | 4.12 | 4.28 | 4.28 | 4.45 | 4.60 |
| 4.6 | 6.50 | 0.35 | 6.06 | 6.38 | 6.37 | 6.80 | 7.18 |
| 5.1 | 9.33 | 0.47 | 8.20 | 8.76 | 9.02 | 9.64 | 10.50 |
| 5.6 | 10.96 | 0.39 | 9.56 | 10.30 | 10.47 | 11.49 | 12.51 |
| 6.1 | 9.67 | 0.33 | 8.46 | 9.06 | 9.22 | 9.98 | 10.90 |
| 6.6 | 6.55 | 0.25 | 6.44 | 6.79 | 6.88 | 7.29 | 7.57 |
| 7.1 | 4.66 | 0.22 | 4.38 | 4.55 | 4.67 | 4.74 | 4.87 |
| 7.6 | 3.06 | 0.15 | 2.93 | 3.01 | 3.07 | 3.08 | 3.17 |
| nnfsr4 configuration ($\theta_{nn} = 20.5°$) | | | | | | | |
| 4.5 | 4.15 | 0.21 | 4.04 | 4.30 | 4.25 | 4.30 | 4.44 |
| 5.0 | 6.33 | 0.31 | 5.75 | 6.33 | 6.29 | 6.40 | 6.70 |
| 5.5 | 9.64 | 0.44 | 8.31 | 9.07 | 9.07 | 9.59 | 10.21 |
| 6.0 | 13.40 | 0.48 | 11.25 | 12.14 | 12.23 | 13.26 | 14.41 |
| 6.5 | 15.77 | 0.40 | 12.66 | 13.80 | 13.95 | 15.27 | 16.80 |
| 7.0 | 13.19 | 0.34 | 11.37 | 12.29 | 12.38 | 13.70 | 14.95 |
| 7.5 | 10.25 | 0.32 | 8.85 | 9.49 | 9.50 | 10.08 | 10.78 |
| 8.0 | 6.40 | 0.26 | 6.42 | 6.57 | 6.54 | 6.78 | 7.09 |
| 8.5 | 4.67 | 0.19 | 4.34 | 4.57 | 4.53 | 4.53 | 4.69 |

Table A.1: Experimental and Monte-Carlo calculated *nd* breakup cross sections.

# Appendix B

# Kinematic Plots

The following plots show the dependence of the S-curve on the neutron energies $E_1$ and $E_2$ for various $nn$ FSI production angles $\theta_{nn}$ (projectile neutron energy $E_0 = 13.0$ MeV). For all configurations the proton energy $E_3$ changes slowly as a function of $E_1$ and $E_2$. For larger $\theta_{nn}$ the proton leaves with a greater fraction of the total energy available, leading to a rapidly-contracting S-curve.

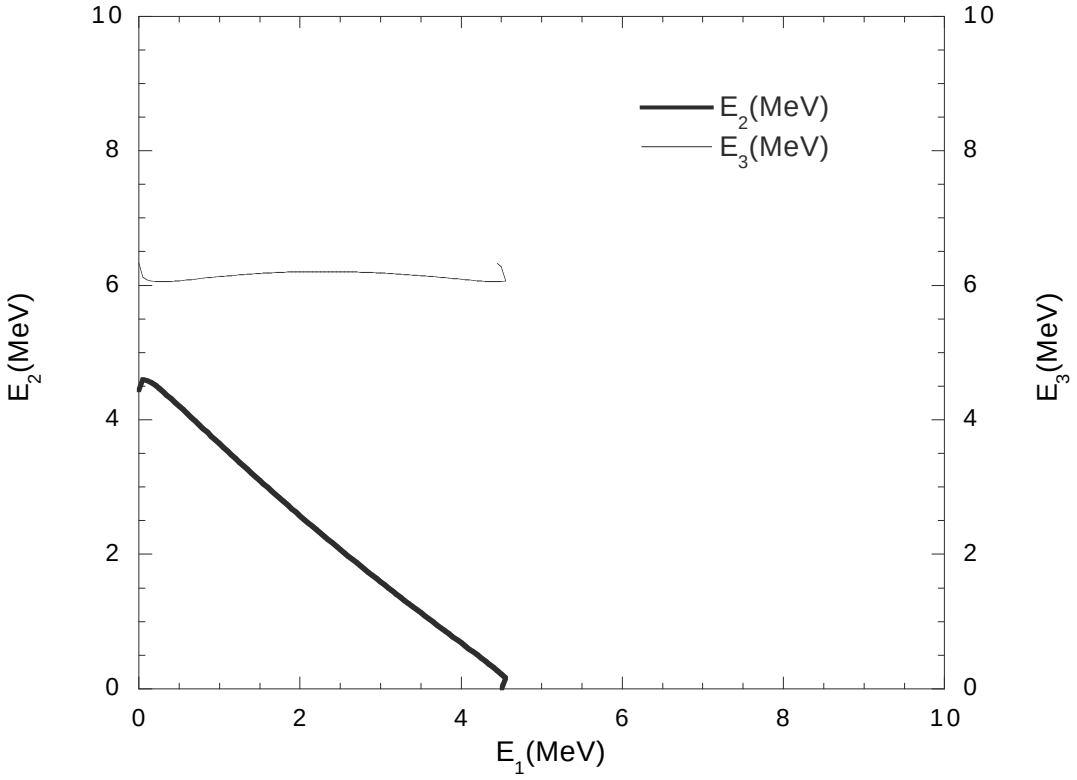


Figure B.1: Kinematic curves for $E_2$ and $E_3$ as a function of $E_1$ ($\theta_{nn} = 43.0^{\circ}$).

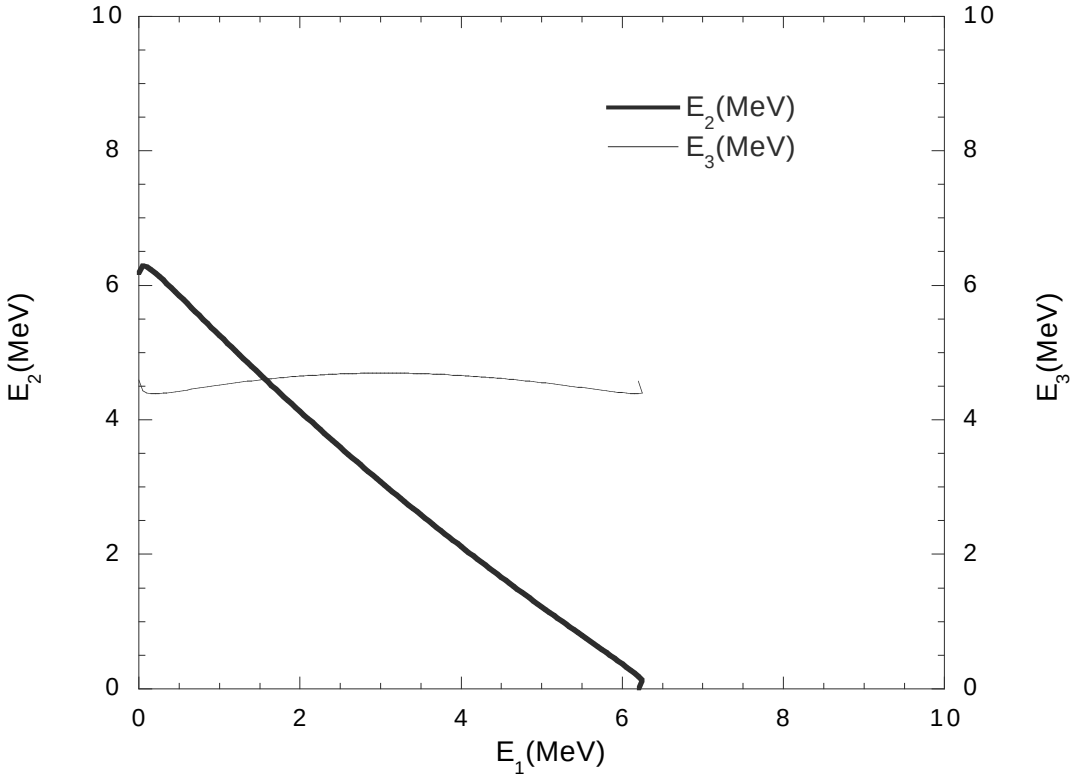


Figure B.2: Kinematic curves for $E_2$ and $E_3$ as a function of $E_1$ ($\theta_{nn} = 35.5^\circ$).

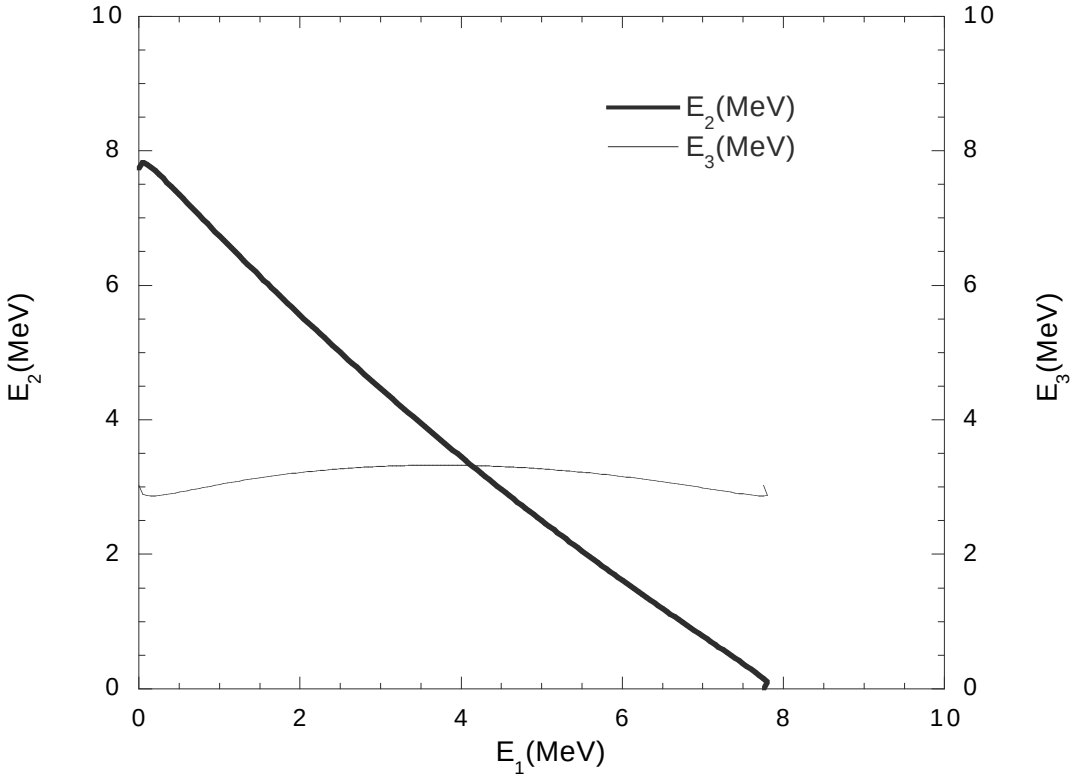


Figure B.3: Kinematic curves for $E_2$ and $E_3$ as a function of $E_1$ ($\theta_{nn} = 28.0^{\circ}$).

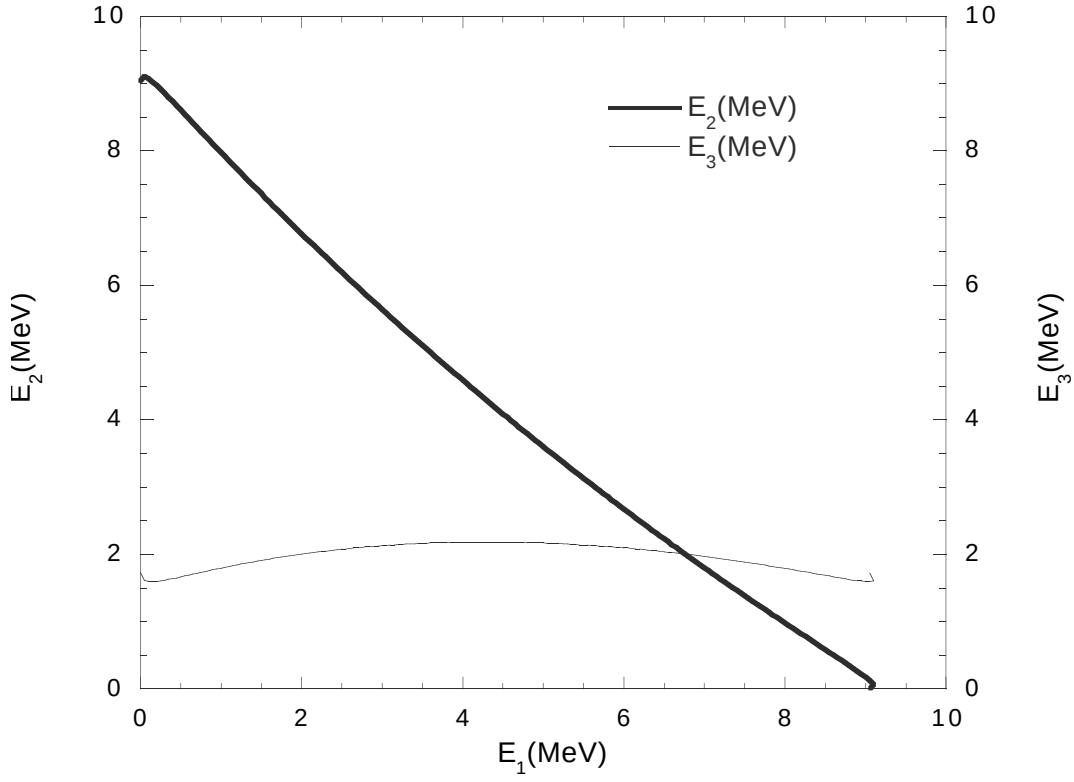


Figure B.4: Kinematic curves for $E_2$ and $E_3$ as a function of $E_1$ ($\theta_{nn} = 20.5^\circ$).

# Bibliography


[Aar65] R. Aaron, R.D. Amado, and Y. Y. Yam. *Calculations of Neutron-Deuteron Scattering.* Physical Review, **140**(1965) B1291.

[Bev69] P. R. Bevington. *Data Reduction and Error Analysis for the Physical Sciences.* McGraw-Hill, 1969.

[Bre80] H. J. Brede. *The Braunschweig Accelerator Facilty for Fast Neutron Research, I. Building Design and Accelerators.* Nuclear Instruments and Methods in Physics Research, **A169**(1980).

[Coo79] S. A. Coon, M. D. Scadron, P. C. McNamee, B.R. Barrett, D. W. E. Blatt, and B. H. J. McKellar. *The Two-Pion-Exchange Three-Nucleon Potential and Nuclear Matter.* Nuclear Physics, **A317**(1979) 242–278.

[Coo96] S. A. Coon and J. A. Niskanen. *Two-Pion Exchange Contributions to Nuclear Charge Asymmetry.* Physical Review C, **53**(1996) 1154–1160.

[Cub89] J. Cub, E. Finckh, K. Gebhardt, K. Geissdörfer, H. Klein, R. Lin, and J. Strate. *The Neutron Detection Efficiency of NE213 Detectors measured by Means of a $^{252}$Cf source.* Nuclear Instruments and Methods in Physics Research, **A274**(1989) 217–221.

[Die78] G. Dietze. *SPEKT - A Dialog Program for Multichannel Spectra Analysis.* Technical Report PTB-ND-13, Physikalisch-Technische Bundesanstalt, Bundesallee 100, W-3300 Braunschweig, 1978.

[Die82a] G. Dietze and H. Klein. *Gamma-Calibration of NE213 scintillator counters.* Nuclear Instruments and Methods in Physics Research, **A194**(1982).

[Die82b] G. Dietze and H. Klein. *NRESP4 and NEFF4 Monte Carlo Codes for the Calculation of Neutron Response Functions and Detection Efficiencies for NE 213 Scintillation Detectors.* Technical Report PTB-ND-22, Physikalisch-Technische Bundesanstalt, Bundesallee 100, W-3300 Braunschweig, 1982.

[Dro78] M. Drosg. *Unified Absolute Differential Cross Sections for Neutron Production by the Hydrogen Isotopes for Charge-Particle Energies Between 6 and 17 MeV.* Nuclear Science and Engineering, **67**(1978) 190–220.

[Fad61] L.D. Faddeev. *Scattering Theory for a Three-Particle System.* Journal of Experimental and Theoretical Physics (U.S.S.R.), **12**(1961) 1014–1019.

[Fin87] E. Finckh, K. Geissdörfer, R. Lin, S. Schindler, and J. Strate. *Method for Data Analysis of Three Particle Experiments by Monte Carlo Simulation.* Nuclear Instruments and Methods in Physics Research, **A262**(1987) 441–443.

[Fra88] T. N. Frank, H. Haberzettl, W. Kerwath Th. Januschke, and W. Sandhas. *Neutron-deuteron breakup calculations with W-matrix representation of the two-body input.* Physical Review C, **38**(1988) 1112–1117.

[Fri95] J. L. Friar, G. L. Payne, W. Glöckle, D. Hüber, and H. Witała. *Benchmark solutions for n-d breakup amplitudes.* Physical Review C, **51**(1995) 2356–2359.

[Gab84] B. Gabioud, J.-C. Adler, C. Joseph, J.-F. Loude, N. Morel, A. Perrenoud, J.-P. Perroud, M. T. Tran, E. Winkelmann, W. Dahme, H. Panke, D. Renker, G. Strassner, P. Truöl, and G.F. de Téramond. *nn SCATTERING PARAMETERS $a_{nn}$ and $r_{nn}$ FROM THE PHOTON SPECTRUM OF THE REACTION $\pi^- d \rightarrow \gamma nn$.* Nuclear Physics, **A420**(1984) 496–524.

[Geb93] K. Gebhardt, W. Jäger, C. Jeitner, M Vitz, E. Finckh, T.N Frank, Th. Januschke, W. Sandhas, and H. Haberzettl. *Experimental and theoretical investigation of the $^2H(n, nnp)$ reaction and of the neutron-neutron scattering length.* Nuclear Physics A, **A561**(1993) 232–250.

[Glö96] W. Glöckle, H. Witała, D. Hüber, and J. Golack. *The Three-Nucleon Continuum: Achievements, Challenges and Applications.* Physics Reports, **274**(1996) 107–286.

[Gus82] P. P. Guss. *Elastic and Inelastic Scattering Cross Sections and Analyzing Powers for $^{58}Ni$, $^{60}Ni$, $^{116}Sn$ and $^{120}Sn$.* Ph.D. thesis, Duke University, 1982.

[Hei32] W. Heisenberg. Z. Phys., **77**(1932) 1.

[Hon86] G. M. Honoré. *Neutron Scattering Cross Section and Analyzing Power Measurements for $^{40}Ca$ and $^{89}Y$ and Comprehensive Optical Model Analyses.* Ph.D. thesis, Duke University, 1986.

[How84] C. R. Howell. *Neutron Scattering from $^{28}Si$ and $^{32}S$: Cross Sections and Analyzing Powers from 8 to 40 MeV.* Ph.D. thesis, Duke University, 1984.

[Hüb93] D. Hüber, H. Witała, and W. Glöckle. *Momentum-Space Calculations for Three-Nucleon Scattering Including a Three-Nucleon Force.* Few-Body Systems, **14**(1993) 171–190.

[Kle] H. Klein, private communication.

[Leo94] W.R. Leo. *Techniques for Nuclear and Particle Physics Experiments.* Springer-Verlag, 1994.

[Lov64] C. Lovelace. In R.G. Moorehouse, editor, *Lectures of the 1963 Edinburgh Summer School*, 1964.

[Mac87] R. Machleidt, K. Holinde, and Ch. Elster. *The Bonn Meson-Exchange Model for the Nucleon-Nucleon Interaction.* Physics Reports, **149**(1987) 1–89.

[Mil90] G.A. Miller, B.M.K. Nefkens, and I. Šlaus. *Charge Symmetry, Quarks and Mesons.* Physics Reports, **194**(1990) 1–116.

[One78] Y. Onel, R. C. Brown, J. A. Edington, N. M. Stewart, and I. M. Blair. *Further Study of the reaction* $^2$*H(n,p2n) near 120 MeV.* Nuclear Physics, **A304**(1978) 51.

[Ped86] R. S. Pedroni. *Cross Sections and Analyzing Powers in the 8 to 17 MeV Range for Neutron Scattering from* $^{54,56}$*Fe,* $^{58,60}$*Ni,* $^{93}$*Nb, and* $^{120}$*Sn.* Ph.D. thesis, Duke University, 1986.

[Pre36] R. D. Present. Physical Review, **50**(1936) 635.

[Sch87] O. Schori, B. Gabioud, C. Joseph, J.-P. Perroud, D. Rüegger, M. T. Tran, P. Truöl, E. Winkelmann, and W. Dahme. *Measurement of the Neutron-Neutron Scattering Length* $a_{nn}$ *with the Reaction* $\pi^- d \rightarrow nn\gamma$ *in Complete Kinematics.* Physical Review C, **35**(1987) 2252–2257.

[Set95] H. R. Setze. *Differential Cross Section for the Neutron-Induced Deuteron Breakup Reaction at* $E_n = 13.0$ *MeV.* Ph.D. thesis, Duke University, 1995.

[Šla89] I. Šlaus, Y. Akaishi, and H. Tanaka. *Neutron-Neutron Effective Range Parameters.* Physics Reports, **173**(1989) 259–300.

[Tak51] M. Taketani, S. Nakamura, and M. Sasaki. *On the Method of the Theory of Nuclear Forces.* Progress of Theoretical Physics, **VI**(1951).

[Tér89] G.F. de Téramond. *Charge Symmetry of the Nuclear Interaction and the N-N Scattering Parameters.* In *Proc. Workshop on Spin and Symmetries*, volume TRI-89-5, pages 235–244, 1989.

[Tic92] M. Tichy, H. Klein, and J. Pulpan. *Calibration of an NE-213 Scintillator.* Technical Report PTB-7.2-92-1, Physikalisch-Technische Bundesanstalt, Bundesallee 100, W-3300 Braunschweig, 1992.

[Tor86] W. Tornow, W. Arnold, J. Herdtweck, and G. Mertens. *Measurement of the Response of the Deuterated Scintillators NE 232 and NE 230 to Protons and Deuterons.* Nuclear Instruments and Methods in Physics Research, **A244**(1986).

[Tor93a] W. Tornow, R. T. Braun, and H. Witała. *Determinations of the Neutron-Neutron Scattering Length from Incomplete Neutron-Deuteron Breakup Data Revisited.* Physics Letters B, **318**(1993) 281–286.

[Tor93b] W. Tornow, H. Witała, and D.E. González Trotter. *Watson-Migdal Model Versus Rigorous Three-Nucleon: A Comparison of Neutron-Neutron Final-State-Interaction Cross Sections for $^2H(n,nn)p$.* In *Triangle Universities Nuclear Laboratory Progress Report*, volume XXXII, pages 41–44, 1993.

[Tor94] W. Tornow, H. Witała, D. Hüber, W. Glöckle, and D.E. González Trotter. *Extracting the Neutron-Neutron Scattering Length from Kinematically Complete n-d Breakup Experiments: Sensitivity to NN Potential Models.* In *Triangle Universities Nuclear Laboratory Progress Report*, volume XXXIII, pages 43–46, 1994.

[Tor96] W. Tornow, H. Witała, and R. T. Braun. *Determinations of the Neutron-Neutron Scattering Length from Kinematically Incomplete Neutron-Deuteron Breakup Data Revisited.* Few-Body Systems, **21**(1996) 97–130.

[Tuv36] M. A. Tuve, N. P. Heydenburg, and L. R. Hafstad. *Magnetic Moments of Neutron Resonances in Rare-Earth Nuclei.* Physical Review, **50**(1936) 806.

[vW79] W. von Witsch, B. Gómez Moreno, W. Rosenstock, and K. Ettling. *Determination of the n-n Scattering Length from the $^2H(n,np)n$ Reaction at Bombarding Energies Between Energies Between 17 MeV and 27 MeV.* Nuclear Physics, **A329**(1979) 141–156.

[Wit] H. Witała, private communication.

[Wit88] H. Witała, W. Glöckle, and Th. Cornelius. *Nucleon-induced deuteron breakup: Analysis of 14.1 MeV data by rigorous Faddeev calculations with meson-exchange NN interactions.* Physical Review C, **39**(1988) 384.

[Wit89] H. Witała, W. Glöckle, and Th. Cornelius. *Rigorous Faddeev Calculations for Elastic Neutron-Deuteron Scattering Around 8 MeV c.m. Energy.* Nuclear Physics, **A491**(1989) 157.

[Wit96] H. Witała, D. Hüber, W. Glöckle, W. Tornow, and D. E. González Trotter. *Extraction of the Neutron-Neutron Scattering Length $a_{nn}$ from Kinematically Complete Neutron-Deuteron Breakup Experiments.* Few Body Physics, **20**(1996) 81–92.

[Wu90] Y. Wu, S. Ishikawa, and T. Sasakawa. *Nuclear Charge Asymmetry and Charge Dependence in the $^3H - ^3He$ Binding-Energy Difference.* Physical Review Letters, **64**(1990) 1875–1878.

[Zei70] B. Zeitnitz, R. Maschuw, and P. Suhr. *Determination of the Neutron-Neutron Scattering Length from a Kinematically Complete Experiment on the Reaction $^2H(n,2n)H$.* Nuclear Physics, **A149**(1970) 13–28.

[Zei74] B. Zeitnitz, R. Maschuw, P. Suhr, W. Ebenhöh, J. Bruinsma, and J. H. Stuivenberg. *Neutron-Neutron Effective Range Parameters From Kinematically Complete Experiments on the Reaction $^2H(n,2n)^1H$.* Nuclear Physics, **A231**(1974) 13–28.

# Biography

Dinko E. González Trotter

## Personal

Born in Santiago de Chile, June 4, 1967

## Education

B.S. Physics, Southwestern University, Georgetown, Texas, 1990

A.M. Physics, Duke University, Durham, North Carolina, 1992

## Academic Positions

Teaching Assistant, Duke University, 1990–1992

Research Assistant, Duke University, 1992–1997

## Memberships

American Physical Society

Alpha Chi

## Publications


H. R. Setze, C. R. Howell, W. Tornow, R. T. Braun, W. Glöckle, A. H. Hussein, J. L. Lambert, G. Mertens, C. D. Roper, F. Salinas, I. Šlaus, D. E. González Trotter, B. Vlahović, R. L. Walter, H. Witała. *Verification of the space-star anomaly in nd breakup.* Physics Letters B, **388** 5 (1996).

H. R. Setze, C. R. Howell, R. T. Braun, D. E. González Trotter, A. H. Hussein, C. D. Roper, F. Salinas, I. Šlaus, W. Tornow, B. Vlahović, R. L. Walter, G. Mertens, J. M. Lambert, H. Witała. *Cross-Section Measurements of the Space-Star Configuration in n-d Breakup at 13.0 MeV.* In F. Gross, editor, $14^{th}$ *International IUPAP Conference on Few Body Problems in Physics.* 1994.

R. T. Braun, W. Tornow, D. E. González Trotter, C. R. Howell, C. D. Roper, F. Salinas, H. R. Setze, R. L. Walter. *Neutron-Proton Analyzing Power at 12 MeV and charged $\pi NN$ Coupling Constant.* In F. Gross, editor, $14^{th}$ *International IUPAP Conference on Few Body Problems in Physics.* 1994.

C. R. Howell, W. Tornow, H. R. Setze, R. T. Braun, D. E. González Trotter, C. D. Roper, R. S. Pedroni, S. M. Grimes, C. E. Brient, N. Al-Niemi, F. C. Goeckner. *Resolution of Discrepancy Between Backward Angle Cross-Section Data for Neutron-Deuteron Elastic Scattering*, Few-Body Systems **16**, 127-142, 1994.

H. Witała, D. Hüber, W. Glöckle, W. Tornow, and D. E. González Trotter. *Extraction of the Neutron-neutron Scattering Length $a_{nn}$ from Kinematically Complete Neutron-Deuteron Breakup Experiments.*, Few-Body Systems **20**, 81-92, 1996.

C. R. Howell, H. R. Setze, R. T. Braun, D. E. González Trotter, A. H. Hussein, C. D. Roper, F. Salinas, I. Šlaus, W. Tornow, B. Vlahović, R. L. Walter, G. Mertens, J. M. Lambert, H. Witała. *Probing the three-nucleon force using nucleon-deuteron breakup reactions.* NIM B **99**, 316-319, 1995.

W. Tornow, C. R. Howell, R. T. Braun, Q. Chen, D. E. González Trotter, C. D. Roper, F. Salinas, H. R. Setze, R. L. Walter, H. Witała. *Selected Topics of the Few-Nucleon Research Program at TUNL.* Few-Body Systems Suppl. **8**, 161-165, 1995.